

**DOCTORAL THESIS**

# Properties of $\text{CuSbSe}_2$ and $\text{Sb}_2\text{Se}_3$ Absorber Materials for Solar Cell Applications

Aleksei Penežko

TALLINN UNIVERSITY OF TECHNOLOGY  
DOCTORAL THESIS  
74/2022

**Properties of  $\text{CuSbSe}_2$  and  $\text{Sb}_2\text{Se}_3$   
Absorber Materials for Solar Cell  
Applications**

ALEKSEI PENEŽKO



TALLINN UNIVERSITY OF TECHNOLOGY

School of Engineering

Department of Materials and Environmental Technology

This dissertation was accepted for the defence of the degree 17/11/2022

**Supervisor:**

Prof. Maarja Grossberg-Kuusk  
School of Engineering  
Tallinn University of Technology  
Tallinn, Estonia

**Co-supervisor:**

Dr. Marit Kauk-Kuusik  
School of Engineering  
Tallinn University of Technology  
Tallinn, Estonia

**Opponents:**

Associate Professor, Dr. Vambola Kisand  
Faculty of Science and Technology  
Institute of Physics  
University of Tartu  
Tartu, Estonia

Senior Researcher, Dr. Rokas Kondrotas  
Department of Characterization of Material Structure  
Centre for Physical Science and Technology  
Vilnius, Lithuania

**Defence of the thesis:** 20/12/2022, Tallinn

**Declaration:**

Hereby I declare that this doctoral thesis, my original investigation and achievement, submitted for the doctoral degree at Tallinn University of Technology has not been submitted for doctoral or equivalent academic degree.

Aleksei Penežko

-----  
signature



European Union  
European Regional  
Development Fund



Investing  
in your future

Copyright: Aleksei Penežko, 2022

ISSN 2585-6898 (publication)

ISBN 978-9949-83-939-1 (publication)

ISSN 2585-6901 (PDF)

ISBN 978-9949-83-940-7 (PDF)

Printed by Koopia Niini & Rauam

TALLINNA TEHNIKAÜLIKOOL  
DOKTORITÖÖ  
74/2022

**Päikeseplatari absorbermaterjalide  
CuSbSe<sub>2</sub> ja Sb<sub>2</sub>Se<sub>3</sub> omaduste  
uurimine**

ALEKSEI PENEŽKO





# Contents

Contents.....	5
List of publications .....	7
Author’s contribution to the publications .....	8
Introduction .....	9
Abbreviations, terms and symbols.....	11
1 Literature review.....	12
1.1 Fundamentals of photovoltaics.....	12
1.1.1 Emerging materials for thin film PV.....	12
1.2 Binary and ternary Sb- chalcogenides as absorber materials .....	13
1.2.1 CuSbSe <sub>2</sub> .....	13
1.2.1.1 Phase diagram of CuSbSe <sub>2</sub> .....	13
1.2.1.2 Structural properties of CuSbSe <sub>2</sub> .....	14
1.2.1.3 Optical and electrical properties of CuSbSe <sub>2</sub> .....	15
1.2.1.4 Defects in CuSbSe <sub>2</sub> .....	16
1.2.1.5 CuSbSe <sub>2</sub> preparation methods and application in solar cells .....	17
1.2.2 Sb <sub>2</sub> Se <sub>3</sub> .....	19
1.2.2.1 Phase diagram and structural properties of Sb <sub>2</sub> Se <sub>3</sub> .....	19
1.2.2.2 Optical and electrical properties of Sb <sub>2</sub> Se <sub>3</sub> .....	20
1.2.2.3 Defects in Sb <sub>2</sub> Se <sub>3</sub> .....	21
1.2.2.4 Solar cells based on Sb <sub>2</sub> Se <sub>3</sub> .....	22
1.3 Post-treatment of CuSbSe <sub>2</sub> and Sb <sub>2</sub> Se <sub>3</sub> .....	23
1.4 Photoluminescence spectroscopy.....	24
1.4.1 Band-to-band photoluminescence .....	25
1.4.2 Excitonic transitions .....	25
1.4.3 Free-to-bound PL (FB) .....	25
1.4.4 PL from donor-acceptor pair (DAP) recombination.....	26
1.5 Summary of the literature review and aim of the thesis .....	26
2 Experimental details.....	28
2.1 Preparation of CuSbSe <sub>2</sub> .....	28
2.2 Preparation of Sb <sub>2</sub> Se <sub>3</sub> .....	28
2.3 Preparation of CuSbSe <sub>2</sub> thin films and solar cells.....	28
2.3.1 Preparation of the substrates.....	28
2.3.2 Preparation and deposition of CuSbSe <sub>2</sub> thin films by magnetron sputtering ..	29
2.3.3 Post-annealing – selenization.....	30
2.3.4 Buffer layer and window layer deposition .....	30
2.4 Characterization methods.....	31
3 Results and discussion.....	32
3.1 Structural and elemental composition of CuSbSe <sub>2</sub> polycrystalline samples .....	32

3.1.1 EDX, XRD and Raman analyzes of polycrystalline CuSbSe <sub>2</sub> .....	32
3.1.2 Photoluminescence studies of polycrystalline CuSbSe <sub>2</sub> .....	34
3.2 Analysis of Sb <sub>2</sub> Se <sub>3</sub> polycrystals .....	36
3.2.1 XRD and Raman studies of Sb <sub>2</sub> Se <sub>3</sub> polycrystals .....	36
3.2.2 Photoreflectance study of Sb <sub>2</sub> Se <sub>3</sub> polycrystals .....	37
3.2.3 Photoluminescence study of Sb <sub>2</sub> Se <sub>3</sub> polycrystals .....	37
3.3 Structural properties of as-deposited CuSbSe <sub>2</sub> thin films .....	41
3.3.1 SEM, EDX and Raman analyzes of CuSbSe <sub>2</sub> thin films .....	41
3.3.2 Properties of selenized CuSbSe <sub>2</sub> thin films .....	42
Conclusions .....	46
References .....	48
Acknowledgements .....	57
Abstract .....	58
Lühikokkuvõte .....	61
Appendix .....	63
Curriculum vitae .....	86
Elulookirjeldus .....	88

## List of publications

The list of author's publications, on the basis of which the thesis has been prepared:

- I **A. Penezko**, M. Kauk-Kuusik, O. Volobujeva, R. Traksmaa, and M. Grossberg, Observation of photoluminescence edge emission in CuSbSe<sub>2</sub> absorber material for photovoltaic applications, *Appl. Phys. Lett.* 115, 092101, 2019. <https://doi.org/10.1063/1.5114893>
- II M. Grossberg, O. Volobujeva, **A. Penezko**, R. Kaupmees, T. Raadik, J. Krustok, Origin of photoluminescence from antimony selenide, *Journal of Alloys and Compounds*, Volume 817, 152716, 2020. <https://doi.org/10.1016/j.jallcom.2019.152716>
- III **A. Penezko**, M. Kauk-Kuusik, O. Volobujeva, M. Grossberg, Properties of Cu-Sb-Se thin films deposited by magnetron co-sputtering for solar cell applications, *Thin Solid Films* 740, 139004, 2021. <https://doi.org/10.1016/j.tsf.2021.139004>

The copies of the papers are included in Appendix.



## **Author's contribution to the publications**

Contribution to the papers in this thesis are:

- I Major part of experimental work, including the synthesis and post-growth thermal treatments of polycrystalline  $\text{CuSbSe}_2$ ; characterization of the materials by Raman spectroscopy and temperature dependent photoluminescence spectroscopy; analysis of the results and major role in writing.
- II Major part of measurements of  $\text{Sb}_2\text{Se}_3$  polycrystals by Raman spectroscopy and part of the measurements of temperature dependent photoluminescence spectroscopy; part of analysis of the results and minor role in writing.
- III Major part of experimental work, including the deposition of Cu-Sb-Se thin films by magnetron sputtering; post-deposition chemical and heat treatment of thin films; characterization of thin films by Raman spectroscopy; preparation of thin film solar cell structures and characterizing their performance; data analysis and major role in manuscript writing.

## Introduction

Energy consumption is increasing very fast due to the growing world's population, which is projected to reach 8 billion people by the end of 2022. It is extremely urgent to utilize renewable energy instead of burning fossil fuels to alleviate the energy crisis and environmental pollution. According to the International Energy Agency, in 2019, global final electricity consumption reached 22848 TWh [1], from which 63.1% was generated from fossil fuels. Photovoltaic (PV) power generation technology is expected to play an important role in replacing traditional fossil fuels with green and sustainable energy production resources. Furthermore, solar photovoltaic is the fastest growing renewable energy sector. In the first quarter of 2022, the installed PV capacity reached 1 TW [2,3]. In addition to the conventional PV modules, PV can also be integrated with construction elements such as facades, walls, windows, or roof structures to provide innovative clean energy solutions for zero energy buildings. This integrated design is known as building-integrated photovoltaics (BIPV) [4,5].

Silicon solar cells have been the dominant driving force behind photovoltaic technology in recent decades. Crystalline silicon comprises more than 95% of the total revenue of the photovoltaic electricity market. One advantage is the high efficiency – 26.7% for monocrystalline and 24.4% for multicrystalline silicon wafer-based solar cells [6]. One of the drawbacks of crystalline silicon is the indirect nature of its electronic bandgap, which makes it a relatively weak absorber of long-wavelength sunlight. Traditionally, this has been compensated by a relatively thick (100-500  $\mu\text{m}$ ) silicon structure. Although thicker silicon allows more solar radiation to be absorbed, it increases the cost of materials over a large area and makes the structure inflexible [7].

When considering new materials for investigation as absorbers for PV, the main concerns, which need to be addressed are production cost, abundance of the constituent elements, stability and material properties. Among the photovoltaic technologies, thin film technologies have become one of the most cost-competitive due to their low material and production costs [8]. Thus far, commercial thin-film solar cells such as CdTe and Cu(In,Ga)Se<sub>2</sub> (CIGS) cells show a high power conversion efficiency (PCE) of 22.1% [9] and 23.35% [10], respectively. However, tellurium and indium are expensive and limited in reserves, not to mention the toxicity of cadmium. These disadvantages severely hinder the mass-production of PV panels based on materials containing these critical elements. Therefore, to meet the growing demand for sustainable solar electricity production, it is highly required to explore semiconductor thin films consisting of non-toxic elements with rich reserves and suitable photoelectric properties for solar energy conversion. Another aspect to consider in the development of PV devices is their stability when exposed to real operation conditions. For example perovskite solar cells have gain a lot of attention due to their rapid growth in efficiency over a short period of time, but the major obstacle in the way of commercialization is easy degradation of perovskites. Stability concerns can be somewhat reduced by investigating inorganic materials. Recently, a considerable effort has been invested to gain a better and deeper understanding of structural, electrical and optical properties of binary and ternary Sb-based chalcogenide semiconductors aiming at their application in photovoltaics. For example, CuSbSe<sub>2</sub> and Sb<sub>2</sub>Se<sub>3</sub> appear to be promising absorber materials for thin-film solar cells due to their attractive optical and electrical properties, as well as earth-abundant, low-cost and low-toxic constituent elements. However, at the beginning of this doctoral study, very little was known about the defects in these materials, the photoluminescence studies

were missing in the literature. It is well known that defects play a major role in determining the performance of photovoltaics and therefore need careful investigation. The aim of the research of this thesis is to reduce this knowledge gap.

The first aim of this research was to synthesize  $\text{CuSbSe}_2$  polycrystalline materials with homogenous phase composition and to study their defect structure and related recombination mechanisms by photoluminescence spectroscopy. The second aim was to study the defect structure and related recombination mechanisms by photoluminescence spectroscopy in polycrystalline  $\text{Sb}_2\text{Se}_3$ . The third aim was to deposit  $\text{CuSbSe}_2$  thin films by magnetron co-sputtering method and to investigate the effect of the post-annealing conditions on their morphology, structural and compositional properties and to fabricate and characterize  $\text{CuSbSe}_2$  based thin film solar cells.

The novelty of this study relies in the gained information about the electronic defects in  $\text{CuSbSe}_2$  and  $\text{Sb}_2\text{Se}_3$  paving the way towards further improvement of the solar cells based on these materials.

This thesis contains three chapters. The first chapter provides a literature overview of the main properties of  $\text{CuSbSe}_2$  and  $\text{Sb}_2\text{Se}_3$  absorber materials, the preparation methods and achieved photovoltaic performances of devices based on these absorbers. The second chapter describes the applied experimental procedures for the synthesis of  $\text{CuSbSe}_2$  and  $\text{Sb}_2\text{Se}_3$  polycrystals and for the deposition of  $\text{CuSbSe}_2$  thin films. Also, the implemented characterization methods are summarized. The third chapter contains the results and discussion of the experimental work and is based on the three published papers.

This work was supported by institutional research funding IUT19-28 of the Estonian Ministry of Education and Research, by the European Regional Development Fund, Project TK141, by the Estonian Research Council grant PRG1023 and by ASTRA “TUT Institutional Development Programme for 2016-2022” Graduate School of Functional Materials and Technologies (2014-2020.4.01.16-0032). The research was conducted using the NAMUR+ core facility funded by projects “Center of nanomaterials technologies and research” (2014-2020.4.01.16-0123) and TT13.

## Abbreviations, terms and symbols

AS	Admittance spectroscopy
CIGS	$\text{Cu}(\text{In,Ga})(\text{S,Se})_2$
CZTSSe	$\text{Cu}_2\text{ZnSn}(\text{S,Se})_4$
DC	Direct current
DFT	Density functional theory
DLTS	Deep level transient spectroscopy
EDX	Energy dispersive x-ray spectroscopy
$E_g$	Band gap energy
EQE	External quantum efficiency
$FF$	Fill factor
HR-SEM	High-resolution scanning electron microscopy
ITO	Indium tin oxide
$J-V$	Current density–voltage
$J_{sc}$	Short circuit current density
PCE	Power conversion efficiency
PL	Photoluminescence
PV	Photovoltaic
RCSS	Reactive close spaced sublimation
RF	Radio frequency
$R_s$	Series resistance
$R_{SH}$	Shunt resistance
RT	Room temperature
SCCM	Standard cubic centimeter
SEM	Scanning electron microscopy
SLG	Soda–lime glass
TU	Thiourea
$T_s$	Substrate temperature
$V_{OC}$	Open-circuit voltage
$V_{Se}$	Selenium vacancy
$V_{Sb}$	Antimony vacancy
VBM	Valence band maximum
VTD	Vapor transport deposition
XRD	X-ray diffraction
$\theta$	X-ray diffraction incidence angle
$\Phi$	Integral intensity of the PL band
$\sigma(T)$	Temperature dependent electrical conductivity

# 1 Literature review

This chapter provides an overview of the fundamentals of photovoltaics, main properties of CuSbSe<sub>2</sub> and Sb<sub>2</sub>Se<sub>3</sub>, common thin film deposition methods, and the development of solar cells based on these materials. Basics of the photoluminescence spectroscopy as the most relevant characterization technique used in this thesis is also introduced.

## 1.1 Fundamentals of photovoltaics

The direct solar energy conversion into electricity is based on the photoelectric effect of the materials used for the energy harvesting. Semiconductors convert light energy from the sun into electricity between an n-type and a p-type semiconductor at the p-n junction interface, which contains electrons and holes [11].

Typical multilayer structure of a heterojunction solar cell consists of a substrate, back contact, *p*-type absorber layer, *n*-type buffer layer, and transparent front contact. It can be fabricated in a superstrate or a substrate configuration. Absorber materials with a direct band gap in between 1.0 eV and 2.0 eV, and with an absorption coefficient ( $\alpha$ ) of  $10^4$ – $10^5$  cm<sup>-1</sup> in visible light spectral region, are applied [11]. The buffer is generally a wide band gap *n*-type semiconductor between absorber and the transparent conducting oxide layers [12]. Free charge carriers in the contact layer are removed from the solar cell into the electrical circuit. Thus, environmentally friendly electrical energy without unwanted greenhouse gas emissions is received.

### 1.1.1 Emerging materials for thin film PV

Thin-film photovoltaic technologies play a major role in preventing the carbon emission and have the smallest environmental footprint of all photovoltaic solar energy conversion technologies due to their energy and material efficient manufacturing processes.

Currently, the thin film PV market is dominated by the thin film *a*-Si, CdTe and CIGS, even though they face the concern of high toxicity of cadmium and scarcity of indium and tellurium contained in those materials. This has driven the research to concentrate on other absorber materials made from abundant and environmentally benign elements:

- Kesterite, i.e. Cu<sub>2</sub>ZnSn(S, Se)<sub>4</sub> (CZTSSe);
- Sb-containing binary and ternary chalcogenides, i.e. Sb<sub>2</sub>Se<sub>3</sub> and CuSbSe<sub>2</sub>;
- organic and inorganic Perovskite solar cells etc.

Quaternary CZTSSe compounds have gained significant attention and reached solar cell efficiencies around 13% [13]. Currently, the researchers are facing the challenge of high open circuit voltage deficit of kesterite solar cells arising from the combination of a high density of trap defect states, band tailing, low carrier lifetime, and material inhomogeneity.

Perovskites have revolutionized the emerging photovoltaic field achieving record-breaking solar cell efficiencies. Hybrid organic–inorganic halide perovskite solar cells (PSCs) were improved rapidly over the past few years. PSCs now possess an increased output voltage ( $\approx 1.1$  V) and their PCE has increased rapidly from 3.8% in 2009 [14] to over 25.8% in 2021 [15]. At present, the long-term stability of lead halide perovskite cells is a problem. In addition to the stability issues, the usage of toxic lead (Pb) and scaling-up are the main challenges towards bringing perovskite technologies to the market. Despite the tremendous success of perovskite solar cells in recent years, Pb as metal cation seems to be vital for achieving high efficiencies, as all devices with PCE

values above 20% adopt Pb-based halide perovskites as absorber material. Consequently, the associated toxicological hazard in case of unintentional liberation of Pb-containing degradation products into the environment raises serious concerns in view of the large-scale applicability of perovskite solar panels.

Figure 1 shows the evolution of solar cell performance for a variety of thin film photovoltaic materials. CIGSe, CZTSSe and perovskites are showing a steady upward trend, while the efficiency of CuSbSe<sub>2</sub> and Sb<sub>2</sub>Se<sub>3</sub> just started to increase [16].

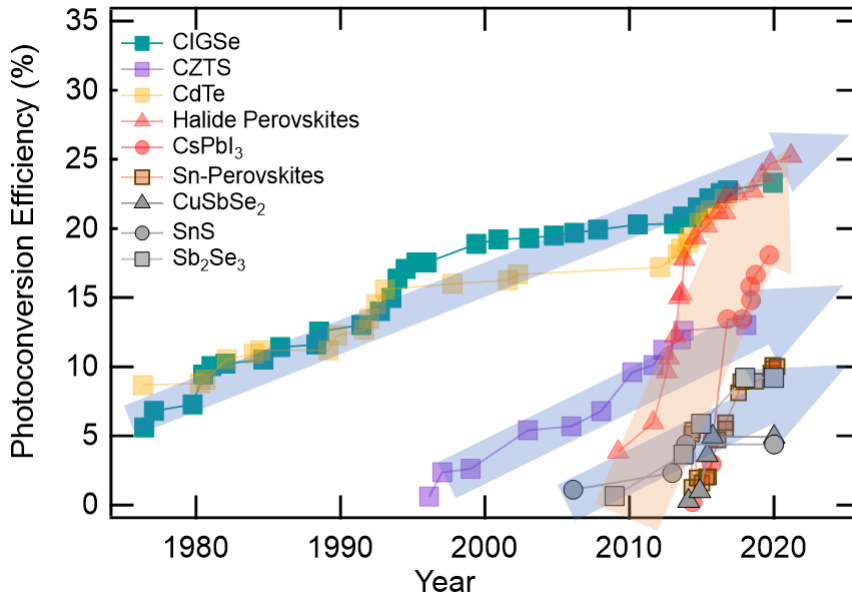


**Figure 1.** Evolution of solar cell performance for a variety of thin film photovoltaic materials. Light arrows are guides to the eye [16].

Among alternative compounds, binary and ternary antimony chalcogenides Sb<sub>2</sub>Se<sub>3</sub> and CuSbSe<sub>2</sub> are *p*-type semiconductors with great potential as absorbers for PV. Being in the focus on this thesis, more detailed overview of the properties of these materials is provided in the next section.

## 1.2 Binary and ternary Sb- chalcogenides as absorber materials

The two absorber materials for photovoltaics investigated in this study are CuSbSe<sub>2</sub> and Sb<sub>2</sub>Se<sub>3</sub>. In the following, an overview of the state of the art in the literature is given, particularly regarding their use as photovoltaic absorber materials.

### 1.2.1 CuSbSe<sub>2</sub>

#### 1.2.1.1 Phase diagram of CuSbSe<sub>2</sub>

Cu–Sb–Se system is complicated because it contains besides CuSbSe<sub>2</sub> phase, at least five binary or ternary phases including Cu<sub>2</sub>Se, CuSe, Sb<sub>2</sub>Se<sub>3</sub>, Cu<sub>3</sub>SbSe<sub>4</sub>, and Cu<sub>3</sub>SbSe<sub>3</sub> that could exist as secondary phases if the samples are non-stoichiometric or prepared with an inappropriate process [17].

The phase diagram of  $\text{Cu}_2\text{Se}$  and  $\text{Sb}_2\text{Se}_3$  system is investigated in several studies [18,19] and is presented in Figures 2A-C.  $\text{CuSbSe}_2$  exists in a very narrow compositional region; it should be close to 1:1:2 stoichiometry to prevent the formation of secondary phases. Cu-Se phases are highly conductive and can cause a shunting effect having therefore detrimental effect on the PV device performance. Another possible secondary phase,  $\text{Sb}_2\text{Se}_3$ , on the other hand has been shown to be an efficient PV absorber [20]. However, as a secondary phase with a different band gap, it will cause unwanted recombination of charge carriers in the  $\text{CuSbSe}_2$  based solar cell device. Due to the narrow single phase material region, the synthesis of phase-pure  $\text{CuSbSe}_2$  by the solid state reaction is rather challenging.

Figure 2B presents the phase diagram of  $\text{Cu}_2\text{Se}-\text{Sb}_2\text{Se}_3$ , which was studied by Glazov *et al.* [21]. More detailed study was performed by Golovei *et al.* [22], where the extension of  $\text{CuSbSe}_2$ -based solid solution as 49.5–50.1 mol%  $\text{Sb}_2\text{Se}_3$  was determined. The maximum melting temperature ( $491 \pm 3$  °C) of  $\text{CuSbSe}_2$  corresponds to the  $\text{Sb}_2\text{Se}_3$  content 49.6 mol% (Figure 2C). The melting temperature of the stoichiometric  $\text{CuSbSe}_2$  is  $481 \pm 3$  °C. Temperature values were measured using differential thermal analysis. In the Cu-rich region,  $\text{Cu}_3\text{SbSe}_3$  is formed as an additional phase, and in the Sb-rich region additional phase of  $\text{Sb}_2\text{Se}_3$  is formed.

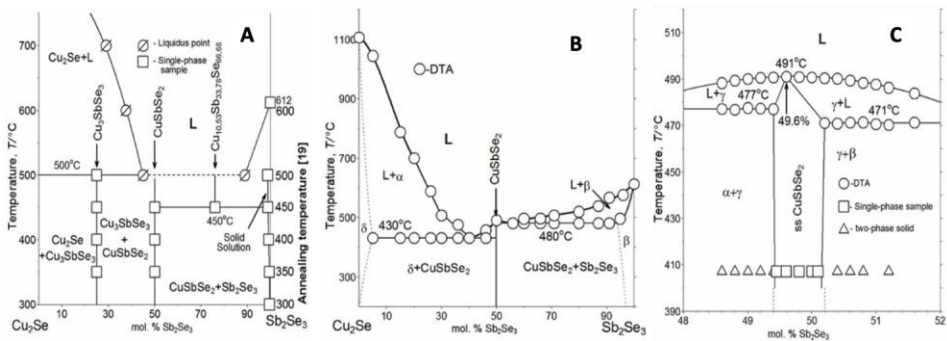


**Figure 2.** Phase diagrams of the  $\text{Cu}_2\text{Se}-\text{Sb}_2\text{Se}_3$  system [18,21,22].

According to Figure 2C, the optimal composition of 49.6 mol%  $\text{Sb}_2\text{Se}_3$  and 50.4 mol%  $\text{Cu}_2\text{Se}$  at 491 °C should be used for the synthesis of  $\text{CuSbSe}_2$ .

### 1.2.1.2 Structural properties of $\text{CuSbSe}_2$

$\text{CuSbSe}_2$  crystallizes in an orthorhombic chalcocite-type layered structure with  $Pnma$  space group [23]. It is composed of double  $\text{CuSbSe}_2$  layers with an interlayer distance of 0.759 nm held together by weak van der Waals forces, as shown in Figure 3. Each layer can be viewed as consisting of  $\text{SbSe}_2$  and  $\text{CuSe}_3$  chains along the  $b$ -axis connected by Sb square pyramids and  $\text{CuSe}_4$  tetrahedral links. These continuous units are interconnected to form layers perpendicular to the  $c$ -axis. Remarkably, analogous to  $\text{Sb}_2\text{Se}_3$  with ribbon-like structure, this layered crystal structure, if oriented along the  $c$ -axis, should provide some chemically inert surfaces (for surfaces enclosed by the  $\text{CuSbSe}_2$  sheet) with few surface states due to the devoid of dangling bonds, thus partly reducing the carrier recombination loss at grain boundaries (GBs) [24].

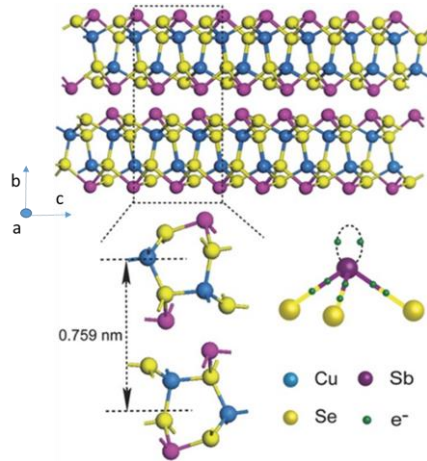


**Figure 3.** Crystal structure of  $\text{CuSbSe}_2$  [24].

As shown in Figure 3, Sb atom is coordinated by three Se atoms with an average Se-Sb-Se bond angle of  $95.24^\circ$ , meaning that only Sb 5p electrons form bonds with Se and Sb 5s electrons are nonbonding to become lone-pair electrons. Thus, the localized unoccupied Sb 5p orbitals in the lower region of conduction band (CB) enable  $\text{CuSbSe}_2$  to have  $(d+p) \rightarrow p$  transition. Due to the high joint density of states (JDOS), the  $(d+p) \rightarrow p$  transition is generally much stronger than the  $(d+p) \rightarrow s$  transition seen in conventional thin film solar cell absorber materials such as CIGS and CZTSSe [24].

The lattice parameters calculated from the experimental diffraction pattern of  $\text{CuSbSe}_2$  were  $a = 6.301 \text{ \AA}$ ,  $b = 3.974 \text{ \AA}$ , and  $c = 14.993 \text{ \AA}$  [24].

During the post-deposition annealing process,  $\text{CuSbSe}_2$  may decompose into  $\text{Cu}_3\text{SbSe}_4$  and  $\text{Sb}_2\text{Se}_3$ .  $\text{Cu}_3\text{SbSe}_4$  crystallizes in a farnatinitite-type structure, where both copper and antimony are coordinated tetrahedrally by selenium. Ordering of the Se tetrahedra results in a tetragonal superstructure of zincblende-type, characterized by a  $c/a$  ratio of 1.993.  $\text{Cu}_3\text{SbSe}_4$  with tetragonal structure has space group  $I\bar{4}2m$  with lattice parameters  $a = 5.6609(8) \text{ \AA}$ ,  $c = 11.280(5) \text{ \AA}$  [25].

### 1.2.1.3 Optical and electrical properties of $\text{CuSbSe}_2$

$\text{CuSbSe}_2$  has suitable properties like  $p$ -type conductivity, indirect and direct band gaps in the range 1.04 - 1.2 eV [24,26–28], high absorption coefficient of  $1.8 \times 10^5 \text{ cm}^{-1}$  [29], and a tunable hole concentration in a range of  $10^{15}$ – $10^{18} \text{ cm}^{-3}$  [30], which favor its application in optoelectronics and photovoltaics. Trivalent Sb ( $\text{Sb}^{3+}$ ) with lone-pair 5s2 electrons is known to be responsible for the large absorption coefficient of  $\text{CuSbSe}_2$  [31]. Recently, Surucu *et al.* have determined the temperature dependence of the band gap energy of  $\text{CuSbSe}_2$ , which was found to follow the Varshni model [32]. Their optical analysis by using the derivative spectroscopy technique showed that  $\text{CuSbSe}_2$  thin film has direct and indirect band gap energies of 1.32 and 1.21 eV, respectively, at 10 K. In addition, a room temperature photoluminescence spectrum of the studied  $\text{CuSbSe}_2$  thin film was detected at 1.30 eV.

For comparison,  $\text{Cu}_3\text{SbSe}_4$  is a  $p$ -type semiconductor with a small direct band gap. Theoretical calculations resulted in a band gap energy of 0.26 eV for  $\text{Cu}_3\text{SbSe}_4$  [33]. Experimentally, the band gap of 0.29 eV was determined by optical absorption edge



measurements for  $\text{Cu}_3\text{SbSe}_4$  [34]. Such a low band gap material is not suitable for PV applications and should also be avoided as a secondary phase in the absorber.

Due to the layered structure, charge transport in  $\text{CuSbSe}_2$  is highly anisotropic as carriers transport within the layer is much easier than between layers. In the latter they are required to hop between  $\text{CuSbSe}_2$  sheets weakly bonded by van der Waals forces. In addition, fewer dangling bonds exist at the grain boundaries enclosed by the  $\text{CuSbSe}_2$  sheets. If a  $\text{CuSbSe}_2$  thin film could be engineered so that the  $\text{CuSbSe}_2$  sheets would be aligned vertically onto the substrate, directional charge transport and relatively benign grain boundaries would be obtained, promoting carrier collection and reducing series resistance of a solar cell. It was also demonstrated by Yang *et al.* [35] that  $\text{CuSbSe}_2$ -based solar cells with preferred [013]- and [112]-orientations show better PV device efficiency. Thus, in-depth understanding, and consequently identifying effective means of phase and orientation control, is vital for the development of efficient  $\text{CuSbSe}_2$  photovoltaics [35].

#### 1.2.1.4 Defects in $\text{CuSbSe}_2$

The electrical and optoelectronic properties of semiconductor materials (such as conductivity and its type) are highly dependent on the chemical composition and defect structure. Various point defects can exist in the  $\text{CuSbSe}_2$  lattice, for example: vacancies ( $V_{\text{Cu}}$ ,  $V_{\text{Sb}}$ ,  $V_{\text{Se}}$ ), atomic substitutions ( $\text{Cu}_{\text{Sb}}$ ,  $\text{Sb}_{\text{Cu}}$ ) and interstitial defects ( $\text{Cu}_i$ ,  $\text{Sb}_i$ ,  $\text{Se}_i$ ). The formation and extent of defects is affected by the energy used to form them, which in turn depends on the crystal growth conditions. For example, it is easier to remove a Cu atom from the lattice and form a Cu vacancy ( $V_{\text{Cu}}$ ) if the growth medium is Cu-poor (Cu partial pressure is low). It is more difficult to form  $V_{\text{Cu}}$  if the growth medium is Cu-rich [24].

Density functional theory (DFT) calculations have been performed in a small number of studies to determine the formation energies and energy levels of potential point defects for different chemical potentials in  $\text{CuSbSe}_2$  [24,36]. According to DFT calculations, the dominating acceptor-type defect in Se-rich  $\text{CuSbSe}_2$  is  $V_{\text{Cu}}$  being also behind the  $p$ -type conductivity of the material. For a Se-poor material, DFT predicts nearly equal formation energies and defect concentrations for  $V_{\text{Cu}}$  acceptor and interstitial copper ( $\text{Cu}_i$ ) donor defects, resulting in strong compensation and intrinsic conductivity of the material [24]. Therefore, the Se-poor composition should be avoided if the material is used as the absorber layer in solar cells. According to the theoretical calculations, the  $V_{\text{Cu}}$  acceptor has a shallow energy level at 0.08 eV above the valence band maximum (VBM) and the  $\text{Cu}_i$  donor has an energy level at 0.15 eV below the conduction band minimum (CBM). From deeper acceptor defects,  $\text{Cu}_{\text{Sb}}$  has the lowest formation energy and has an energy level at 0.29 eV above VBM as predicted by DFT [24]. On the other hand, theoretical calculations by Welch *et al.* [36] also predicted the high probability for the presence of deep selenium vacancies ( $V_{\text{Se}}$ ) with amphoteric character having both donor and acceptor states in the gap, which can trap the photoexcited charge carriers affecting the charge carrier lifetime in the  $\text{CuSbSe}_2$ . Transient terahertz spectroscopy measurements have revealed an electron lifetime of 190 ps in the  $\text{CuSbSe}_2$  [36]. Experimentally, Rampino *et al.* [37] have determined from the temperature dependent electrical conductivity measurements the activation energies of acceptor defects of 0.045 eV and 0.14 eV in stoichiometric and Cu-poor  $\text{CuSbSe}_2$ , respectively. A deep acceptor level with an activation energy of 0.17 eV was detected by Soliman *et al.* [38] also from the temperature dependent electrical conductivity measurements.

Rampino *et al.* [37] have detected the contribution of a deep defect with the activation energy of 270 meV to the total capacitance of the Cu-poor CuSbSe<sub>2</sub> thin film based cells by admittance spectroscopy (AS) measurements. However, there was no photoluminescence (PL) studies of this compound available in the literature at the beginning of this doctoral study and therefore, no information is available about the radiative recombination mechanisms and related defects in CuSbSe<sub>2</sub>.

#### 1.2.1.5 CuSbSe<sub>2</sub> preparation methods and application in solar cells

According to spectroscopic limited maximum efficiency calculations, the theoretical power conversion efficiency of CuSbSe<sub>2</sub> solar cells is 27% [39].

Various methods have been used for the synthesis of CuSbSe<sub>2</sub> crystals including mechanical alloying [40,41], fusion method [42], and solvothermal synthesis [43]. For the synthesis of CuSbSe<sub>2</sub> thin films electrodeposition [26], reactive close-spaced sublimation [44], electron beam evaporation [45], pulsed laser deposition [46] and sputtering techniques have been used [28,36].

**Mechanical alloying** is a solid-state powder processing technique to obtain an alloy from precursor powders by grinding in high-energy ball mill. Both, elemental or binary precursors can be used. Zhang *et al.* [40] synthesized CuSbSe<sub>2</sub> polycrystalline compound from elemental powders of Cu, Sb and Se by mechanical alloying. The phase evolution during the mechanical alloying process was studied by XRD and it was concluded that the formation of the ternary chalcostibite compound CuSbSe<sub>2</sub> starts with the reaction between Cu and Se leading to the formation of binary compounds (CuSe and Cu<sub>2</sub>Se). With increasing the milling time, the refined Sb powders were gradually involved in the reaction with Cu and Se to form the ternary chalcostibite compound Cu<sub>3</sub>SbSe<sub>4</sub> and ultimately CuSbSe<sub>2</sub> after a complete consumption of the Sb component. Tiwari *et al.* [41] used mechanical alloying from elemental precursors to prepare source material for thin film deposition by e-beam evaporation. As-deposited thin films were vacuum annealed in the temperature range 350 - 400 °C for 1 hour to obtain stoichiometric (1:1:2) CuSbSe<sub>2</sub> thin films.

**Reactive close-spaced sublimation (RCSS)** is a quite new technique, which is based on traditional close-spaced sublimation (CSS) method. Wang *et al.* [44] used pre-sputtered Cu layer as a substrate and Sb<sub>2</sub>Se<sub>3</sub> powder was evaporated using the traditional CSS method. In RCSS method, the evaporated Sb<sub>2</sub>Se<sub>3</sub> decomposed partially and released Se, which reacted with Cu to form Cu<sub>2</sub>Se. The latter reacted with Sb<sub>2</sub>Se<sub>3</sub> to generate CuSbSe<sub>2</sub>. Using this method, high quality, single-phase CuSbSe<sub>2</sub> films with a doping density of  $\sim 10^{16} \text{ cm}^{-3}$  could be prepared at an optimal substrate temperature of 440–460 °C. An encouraging PCE of 3.04% was obtained for photovoltaic devices with the substrate configuration and structure of ZnO:Al/CuSbSe<sub>2</sub>/CdS/*i*-ZnO/ZnO:Al/Au.

**Electron beam evaporation** is one of the reliable techniques for the growth of thin films of materials with high melting point and it can be useful for multi-component alloys [47]. Goyal *et al.* [45] deposited CuSbSe<sub>2</sub> thin films from pre-synthesized powder using electron beam evaporation. The deposition temperature was varied from 200 400 °C. Optical and electrical analyses showed that the thin film grown at a substrate temperature of 400 °C had strong absorption exceeding  $10^4 \text{ cm}^{-1}$  in the visible spectrum, a band gap  $\sim 1.2 \text{ eV}$ , *p*-type conductivity, and carrier concentration of  $\sim 5.6 \times 10^{15} \text{ cm}^{-3}$ . Solar cell devices were not presented in this study.

**Pulsed laser deposition (PLD)** is one of the most effective methods for the deposition of high quality and adherent material layers with stoichiometric composition [48]. The PLD

process is performed in a high vacuum chamber, where a pulsed laser beam is focused onto the surface of the target material, which vaporizes and forms a plasma plume that expands and condenses onto a substrate surface. In 2021, Goyal *et al.* [49] deposited CuSbSe<sub>2</sub> thin films by PLD at room temperature as well as at 400 °C. As-grown films were post annealed at 400 °C to improve the crystallinity. The results suggested that growth temperature ~400 °C or above is required for the growth of single phase CuSbSe<sub>2</sub> film by suppressing the growth of Sb<sub>2</sub>Se<sub>3</sub> secondary phase. The films had a band gap of ~1.2 eV, p-type conductivity with a carrier concentration value of  $1.2 \times 10^{18} \text{ cm}^{-3}$ , the resistivity and mobility values were around ~5.59 Ω·cm and ~1.10 cm<sup>2</sup> v<sup>-1</sup>s<sup>-1</sup>, respectively. No solar cell device based on CuSbSe<sub>2</sub> thin films by PLD has been published.

**Magnetron sputtering** is one of the physical vapor deposition (PVD) high-rate vacuum coating techniques used to deposit metals, alloys, and compounds to form thin films with thicknesses of nanometers. The sputtering process begins in a vacuum chamber, where high energy argon ions from the plasma bombard the target (the cathode), atoms are ejected from a solid target material and condense onto a substrate (the anode), forming the film [50,51]. There are various advantages of magnetron sputtering such as easy sputtering of any metal, alloy, or compound, high deposition rates, excellent uniformity on large-area substrates and high adhesion of films.

Co-sputtering of the binary compounds (Cu<sub>2</sub>Se and Sb<sub>2</sub>Se<sub>3</sub>) used in the present study is a thin film deposition technique, which can provide the control on the stoichiometry of the dense films over a large area with a high uniformity. There have been only few studies on the fabrication and characterization of CuSbSe<sub>2</sub> thin films using the co-sputtering method [17,28,36] and one study, where first Sb<sub>2</sub>Se<sub>3</sub> was deposited by PLD followed by Cu deposition by magnetron sputtering onto the prepared Sb<sub>2</sub>Se<sub>3</sub> films [52].

Welch *et al.* [28,36] used for CuSbSe<sub>2</sub> absorber synthesis co-sputtering from binary Cu<sub>2</sub>Se and Sb<sub>2</sub>Se<sub>3</sub> targets. Depositions were performed in a sputtering chamber with  $3 \times 10^{-3}$  Torr of Ar and  $10^{-7}$  Torr base pressure, the substrate temperature was varied between 350-410 °C and cooled/heated in excess Sb<sub>2</sub>Se<sub>3</sub> flux. It was the first time, when the PCE of 3% was reported for a PV device based on stoichiometric CuSbSe<sub>2</sub> thin film deposited by sputtering [28].

In 2017, Welch *et al.* [36] presented CuSbSe<sub>2</sub> devices with PCE of 4.7%. The CuSbSe<sub>2</sub> thin films were deposited by combinatorial co-sputtering from binary Cu<sub>2</sub>Se and Sb<sub>2</sub>Se<sub>3</sub> targets to create gradients in chemical composition across the absorber. It is known that the structural and physical properties of films deposited by sputtering are strongly affected by the growth process parameters such as gas pressure, RF power and substrate temperature. From the sample library obtained with the combinatorial co-sputtering technique, it was found that the “self-regulated” growth process in excess Sb<sub>2</sub>Se<sub>3</sub> vapor at 380 °C allowed to deposit the single phase CuSbSe<sub>2</sub> films with the desired stoichiometric composition.

Kim *et al.* [17] deposited CuSbSe<sub>2</sub> thin films by RF magnetron co-sputtering with CuSe<sub>2</sub> and Sb targets. A series of CuSb<sub>x</sub>Se<sub>2</sub> thin films were prepared with different Sb contents adjusted by sputtering power, followed by rapid thermal annealing. The power for CuSe<sub>2</sub> target was fixed to 40 W and for Sb target from 13 to 21 W. It was found that the formation of phase impurities and changes in the surface morphology were directly affected by the Sb sputtering power, with the formation of volatile components like Sb<sub>2</sub>Se<sub>3</sub>(g) at higher powers. The crystallinity of the CuSbSe<sub>2</sub> thin films was enhanced in the near-stoichiometric system at an Sb sputtering power of 15 W, and when increased over 19 W, a considerable degradation in crystallinity was observed. Resistivity, carrier

mobility, and carrier concentration of the near-stoichiometric CuSbSe<sub>2</sub> thin film were 14.4 Ω·cm, 3.27 cm<sup>2</sup>/V·s, and 1.33 × 10<sup>17</sup> cm<sup>-3</sup>, respectively.

In addition to the above-mentioned methods, CuSbSe<sub>2</sub> thin films as absorbers have been prepared also by other techniques. Xue *et al.* [24] reported CuSbSe<sub>2</sub>-based thin film solar cell with PCE of 1.32%, which was fabricated by a hydrazine solution process. In 2018, Rampino *et al.* [37] reported CuSbSe<sub>2</sub> thin film solar cells with 3.8% power conversion efficiency, where absorber material was grown by the low-temperature pulsed electron deposition (LTPED) technique. LTPED is a high energy growth method, based on the sudden ablation of a polycrystalline target, by which complex materials can be deposited at very low substrate temperature.

Experimental PCE of CuSbSe<sub>2</sub> solar cells is still low due to the presence of secondary phases (Cu<sub>2</sub>Se, Sb<sub>2</sub>Se<sub>3</sub>, Cu<sub>3</sub>SbSe<sub>3</sub>, Cu<sub>3</sub>SbSe<sub>4</sub> etc.), non-optimal interface between the absorber and conventionally used CdS buffer layer, and strong recombination of the charge carriers [35]. It is well known that native defects generate recombination routes for the photogenerated charge carriers. As there is very little experimental information about the defects and recombination mechanisms in CuSbSe<sub>2</sub>, the first part of the thesis is focused on the photoluminescence study of CuSbSe<sub>2</sub> to address this knowledge gap.

## 1.2.2 Sb<sub>2</sub>Se<sub>3</sub>

### 1.2.2.1 Phase diagram and structural properties of Sb<sub>2</sub>Se<sub>3</sub>

Since Sb<sub>2</sub>Se<sub>3</sub> is a binary compound with no other stoichiometries (see Figure 4), phase control in the system is trivial.

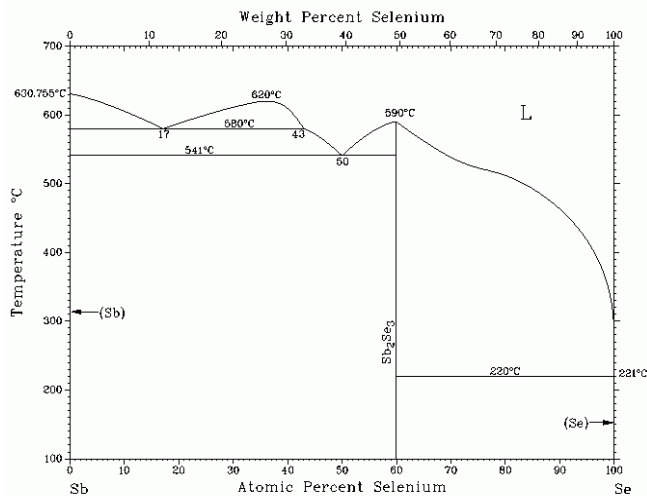


**Figure 4.** The binary phase diagram for Sb and Se [53].

From the structural properties point of view, Sb<sub>2</sub>Se<sub>3</sub> is a one-dimensional line type compound consisting of covalently bonded (Sb<sub>4</sub>Se<sub>6</sub>)<sub>n</sub> ribbons that are stacked together by van der Waals forces and crystallizing in orthorhombic crystal structure with space group *Pbnm* [20]. The Sb<sub>2</sub>Se<sub>3</sub> grains can grow in a columnar manner enabling effective charge carrier transport in one direction, similarly to CuSbSe<sub>2</sub>. Chen *et al.* [54] have shown that carrier collection is significantly improved if the Sb<sub>2</sub>Se<sub>3</sub> grains are preferentially grown along the [001] crystal direction (see Figure 5).

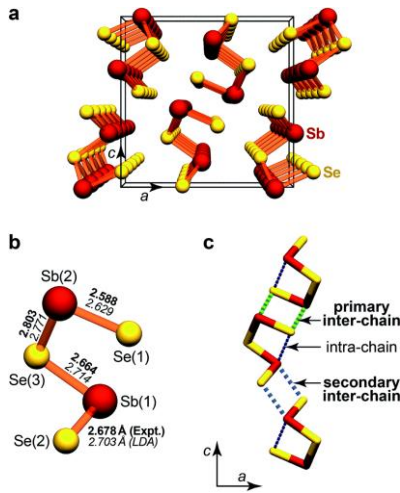


**Figure 5.** Crystal structure of  $Sb_2Se_3$ . a) Perspective view down the short  $b$ -axis, highlighting the “infinite chains” that extend through the crystal, with only the short bonds drawn. (b) Fragment from the above chain, with atomic labelling and Sb–Se distances in Å from experiment (bold) and theory. (c) Structural drawing to emphasise the “weak” contacts along the  $c$ -axis, which connect the strongly bonded 1D chains [55].

### 1.2.2.2 Optical and electrical properties of $Sb_2Se_3$

$Sb_2Se_3$  belongs to  $V_2-VI_3$  ( $V = As, Sb, Bi$ ;  $VI = S, Se, Te$ ) binary materials that have been attracting research interest due to their potential applications in photovoltaics [56].

$Sb_2Se_3$  is a  $p$ -type material with high absorption coefficient ( $>10^5 \text{ cm}^{-1}$  at short wavelength [57]) and nearly optimal band gap energy for solar energy conversion around 1.2 eV at  $T = 300 \text{ K}$  [58]. Both, direct and indirect band gap of  $Sb_2Se_3$  have been detected [20,59]. Chen *et al.* [59] determined indirect band gap  $E_{g \text{ indirect}} = 1.03 \pm 0.01 \text{ eV}$  and direct band gap of  $E_{g \text{ direct}} = 1.17 \pm 0.02 \text{ eV}$  at 300 K from the optical absorption measurements of  $Sb_2Se_3$  thin films. The energetic difference between the indirect and direct band gap of  $Sb_2Se_3$  decreases towards lower temperatures and was found to be only 0.04 eV at  $T = 0 \text{ K}$ . [60] At the same time, even smaller difference of about 0.025 eV at  $T = 0 \text{ K}$  was reported by Birkett *et al.* [58] using temperature-dependent photoreflectance spectroscopy.

Krustok *et al.* [60] have detected the  $A$  and  $B$  biexciton PL emission at 1.302 and 1.322 eV, respectively, at  $T = 3 \text{ K}$ . In addition, they observed  $A$  and  $B$  free exciton emission at 1.311 and 1.333 eV, respectively. The binding energy of  $A$  and  $B$  biexcitons was 9 and 11 meV, respectively, and the binding energy of  $A$  free exciton was 6 meV.

Thin films have been observed to be  $p$ -type [54,56,61] due to  $Se_{Sb}$  defects [62] with doping densities of  $1.49 \times 10^{15} \text{ cm}^{-3}$  being reported for untreated devices [63]. Mobility of the absorber material is an important parameter to be considered when designing and optimizing the device configuration. The hole mobility in a single  $Sb_2Se_3$  grain along  $a$ -,  $b$ - and  $c$ -direction were 1.17, 0.69 and  $2.59 \text{ cm}^2 \text{ V}^{-1} \text{ s}^{-1}$ , respectively. The electron mobility along  $c$ -direction was larger than  $16.9 \text{ cm}^2 \text{ V}^{-1} \text{ s}^{-1}$  [54]. Interestingly, Hobson *et al.* [64] have been able to produce  $n$ -type  $Sb_2Se_3$  thin films and crystals from the source material, which included Cl impurities being the source of  $n$ -type conductivity.

In addition, the conductivity of  $\text{Sb}_2\text{Se}_3$  has been reported to be anisotropic: parallel to the ribbon direction conductivity at room temperature was measured to be  $9 \times 10^{-8} \Omega^{-1}\cdot\text{cm}^{-1}$ , 2.2 times greater than the perpendicular value of  $4 \times 10^{-8} \Omega^{-1}\cdot\text{cm}^{-1}$  [65].

### 1.2.2.3 Defects in $\text{Sb}_2\text{Se}_3$

It is known that defects in the absorber material play a crucial role in determining the solar cell performance. There is only little information available about the defects in  $\text{Sb}_2\text{Se}_3$ . Recently, a comprehensive studies of the first-principles calculations of the defects in  $\text{Sb}_2\text{Se}_3$  was published by Huang *et al.* [66] and by Savory *et al.* [67] stating that due to the low symmetry of the quasi-one-dimensional structure of  $\text{Sb}_2\text{Se}_3$ , a series of donor and acceptor levels are predicted in the band gap of the material, because each point defect located at non-equivalent atomic sites can have very different properties. More specifically, each unit cell is composed of 20 atoms, with 8 Sb and 12 Se, and there are two non-equivalent Sb sites (denoted by Sb(1) and Sb(2)) and three non-equivalent Se sites (denoted by Se(1), Se(2), and Se(3) as can be seen in Figure 5. Several uncommon defects in binary chalcogenide compounds such as the two-anion-replace-one-cation antisite  $2\text{Se}_{\text{Sb}}$  producing a shallow acceptor level or an amphoteric  $\text{Sb}_{\text{Se}}$  defect, which has equal capability of trapping an electron and a hole, are theoretically predicted in  $\text{Sb}_2\text{Se}_3$  [61]. The latter was detected experimentally only recently for the first time by Lian *et al.* [68] in Sb-rich  $\text{Sb}_2\text{Se}_3$ .

The ab initio calculations predict  $V_{\text{Sb}}$  and  $\text{Se}_{\text{Sb}}$  as dominant acceptor defects in Se-rich  $\text{Sb}_2\text{Se}_3$  that is aimed for the PV applications [62,66,69]. Chen *et al.* [54] and Liu *et al.* [62] have experimentally determined an acceptor defect with ionization energy  $E_a = 111$  meV and  $E_a = 107$  meV from the temperature dependent conductivity measurements, respectively. It was assigned to  $\text{Se}_{\text{Sb}}$  defect as it is predicted by theoretical calculations as the defect with the lowest formation energy in  $\text{Sb}_2\text{Se}_3$  with the energy level at about 0.1 eV above the valence band edge  $E_V$  [62,66]. The same defect was detected also in AS measurements with  $E_a = 95$  meV and the density of defects states about  $1 \times 10^{15} \text{cm}^{-3} \text{eV}^{-1}$  [54]. The two deep acceptor defects with energy levels at  $E_V + 0.48$  eV and  $E_V + 0.71$  eV detected in  $\text{Sb}_2\text{Se}_3$  by deep level transient spectroscopy (DLTS) were assigned to  $V_{\text{Sb}}$  and  $\text{Se}_{\text{Sb}}$ , correspondingly [70]. A donor defect at  $E_C - 0.61$  eV detected in the same DLTS study, was assigned to  $\text{Sb}_{\text{Se}}$  donor, which is predicted as the dominating donor defect in  $\text{Sb}_2\text{Se}_3$  based on the theoretical calculations [66,67].

Tao *et al.* [71] published a temperature dependent AS study on  $\text{Sb}_2\text{Se}_3$  solar cells with an efficiency of over 7% and detected the presence of three deep defect levels at 363 meV, 398 meV, and 435 meV, however, no assignment of the defects is provided to the reader. Recently, Krautmann *et al.* [72] has determined a deep defect level at  $E_V + 0.39$  eV from the temperature dependent AS on  $\text{Sb}_2\text{Se}_3$  thin film solar cells without proposing a specific defect. Interestingly, it was also found in [70] that in different samples, the defect densities of  $\text{Se}_{\text{Sb}}$  and  $\text{Sb}_{\text{Se}}$  are always very similar suggesting that they might form  $[\text{Se}_{\text{Sb}} + \text{Sb}_{\text{Se}}]$  defect complexes as is also predicted in the recent study by Huang *et al.* [66]. An overview of the experimentally determined intrinsic defects in  $\text{Sb}_2\text{Se}_3$  are summarized in Table 1.

**Table 1:** Experimentally determined energy levels of intrinsic defects in  $Sb_2Se_3$ .

Energy level (meV)	Proposed defect	Method	Reference
$E_V +111$	$Se_{Sb}$	$\sigma (T)^*$	[54]
$E_V +95$	$Se_{Sb}$	AS	[54]
$E_V +480$	$V_{Sb}$	DLTS	[70]
$E_V +710$	$Se_{Sb}$	DLTS	[70]
$E_C -610$	$Sb_{Se}$	DLTS	[70]
$E_V +286$	-	AS	[73]
$E_V +188$	-	AS	[73]
$E_V +60$	$Se_{Sb}$	$\sigma (T)$	[74]
$E_C -378$	-	DLTS	[75]
$E_C -460$	-	DLTS	[75]
$E_C -690$	-	DLTS	[75]
$E_V +390$	-	AS	[72]

\* Temperature dependent electrical conductivity

#### 1.2.2.4 Solar cells based on $Sb_2Se_3$

The use of  $Sb_2Se_3$  as an absorber material in photovoltaics was investigated by Nair *et al.* in the 2000s, achieving a rather low power conversion efficiency of 0.66% [76]. Since then, a remarkable efficiency improvement up to 3.2% was achieved by Choi *et al.* in 2014 [77]. In the latter study,  $Sb_2Se_3$  was deposited on mesoporous  $TiO_2$  (mp- $TiO_2$ ) by a spin coating method using a single-source precursor and thermal decomposition, followed by an annealing at 300 °C in argon atmosphere. The potential of the  $Sb_2Se_3$  electrodeposited thin films in  $TiO_2/Sb_2Se_3/CuSCN$  planar heterojunction solar cells with PCE 2.2% was presented by Ngo *et al.* [78].

The first thermally evaporated  $Sb_2Se_3$  based solar cell with PCE of 2.1% was presented by Liu *et al.* [79]. During thermal evaporation,  $Sb_2Se_3$  slightly decomposed leading to the formation of Se deficient  $Sb_2Se_{3-x}$  due to the large vapor pressure of Se. Thus, selenium vacancies ( $V_{Se}$ ) were formed, which are predicted to act as deep recombination centers in  $Sb_2Se_3$  films [66]. Thus, an additional selenization step was introduced to the thermal evaporation process in the study by Leng *et al.* [80] resulting in PCE of 3.7%.

Orientalional control of the  $Sb_2Se_3$  film is predicted to be crucial to realize an efficient carrier transport and benign GBs [81,82]. Therefore, the possibility of a correlation between  $Sb_2Se_3$  film orientation and photovoltaic device performance was studied by Zhou *et al.* [81]. By changing the substrate temperature, the preferred [211] orientation of the  $Sb_2Se_3$  active layers was obtained, which improved the transport properties and lowered recombination losses and resulted in lower series resistance ( $R_s$ ), improved fill factor ( $FF$ ) and short circuit current density ( $J_{sc}$ ) of the PV devices. Finally, the oriented crystal growth perpendicular to the substrate showed a certified device efficiency of 5.6% with superstrate configuration SLG/ITO/CdS/ $Sb_2Se_3$ /Au. Krautmann *et al.* [72] were recently able to increase the presence of crystal planes in the [001] direction in the  $Sb_2Se_3$  thin film fabricated by the CSS method by implementing a seed layer. In 2017, Wang *et al.* [83] presented 6%-efficient  $Sb_2Se_3$  solar cell with ZnO buffer layer.

Chen and co-workers succeeded to increase the efficiency up to 6.5% with using PbS colloidal quantum dot film as a hole transport layer (HTL) in superstrate SLG/ITO/CdS/Sb<sub>2</sub>Se<sub>3</sub>/HTL/Au solar cell. Consequently, an improvement was observed in all solar cell parameters [84].

In 2018, Wen *et al.* [70] used a vapor transport deposition (VTD) method to develop Sb<sub>2</sub>Se<sub>3</sub> solar cells. In the VTD process, both the substrate temperature and the distance between source and substrate are adjustable, enabling not only highly oriented Sb<sub>2</sub>Se<sub>3</sub> film, but also enormously improved film crystallinity and reduced bulk and interfacial defects in Sb<sub>2</sub>Se<sub>3</sub> solar cells. By means of this technique, crystallinity of Sb<sub>2</sub>Se<sub>3</sub> films was improved and the efficiency of superstrate ITO/CdS/Sb<sub>2</sub>Se<sub>3</sub>/Au solar cells increased up to 7.6% [70].

Following Wen's work, Li and co-workers [20] constructed [001]-oriented nanorod arrays of Sb<sub>2</sub>Se<sub>3</sub> on Mo-coated glass substrates by using the CSS method. A *p-n* junction between Sb<sub>2</sub>Se<sub>3</sub> nanorods and CdS was formed and investigated. They showed that the element Sb drifts through the entire CdS buffer layer if no definite protection was used. Subsequently, they inserted a very thin TiO<sub>2</sub> layer by atomic layer deposition (ALD) method at the CdS/Sb<sub>2</sub>Se<sub>3</sub> heterojunction interface. This interface engineering with TiO<sub>2</sub> enabled to obtain verified record conversion efficiency of 9.2% for the Sb<sub>2</sub>Se<sub>3</sub> solar cells (ZnO:Al/ZnO/CdS/TiO<sub>2</sub>/Sb<sub>2</sub>Se<sub>3</sub> nanorod arrays/MoSe<sub>2</sub>/Mo) with an absorber thickness over 1 μm while maintaining a high *FF* of 70.3% [20].

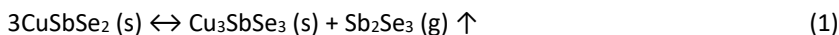
The current efficiency record of 10.12% was obtained by using an injection vapor deposition technology [85], but it is still lower than the theoretical predictions (> 30%, according to Shockley-Queisser limit) [56]. The authors have brought out the suppressed carrier recombination and excellent carrier transport in the record device. To conclude, the efficiency of Sb<sub>2</sub>Se<sub>3</sub> solar cells is still far from the theoretical value.

### 1.3 Post-treatment of CuSbSe<sub>2</sub> and Sb<sub>2</sub>Se<sub>3</sub>

Typically, post-deposition annealing improves the absorber quality by increasing the crystallinity, tuning the crystal orientation, reducing the bulk trap density, and decreasing nonradiative recombination losses. The general approach for improving the crystallinity, optical and electrical properties of polycrystalline thin films of semiconductor compounds is post-deposition annealing involving the introduction of additional volatile elements such as the chalcogen [86]. Selenization process is used to compensate the Se vacancy [79].

Some related studies have been done on the CuSbSe<sub>2</sub> and Sb<sub>2</sub>Se<sub>3</sub> absorber layers. Tang *et al.* [87] investigated the effect of rapid thermal annealing (RTA) at 300 °C in Ar atmosphere on the CuSbSe<sub>2</sub> thin films prepared by one-step electrodeposition. After rapid thermal processing, polycrystalline CuSbSe<sub>2</sub> thin film with improved morphology was obtained.

Abouabassi *et al.* [88] studied annealing of electrodeposited films at 250–500 °C for 15 minutes under nitrogen flow. The annealing process changes the samples morphology depending on the temperature. In the range 250–350 °C, the pure CuSbSe<sub>2</sub> phase was obtained. At 400 °C, the sample became porous with an even distribution of cavities, which was attributed to the evaporation of Sb<sub>2</sub>Se<sub>3</sub> phase, resulting from the decomposition of CuSbSe<sub>2</sub> as follows (1):





From 400 to 500 °C, CuSbSe<sub>2</sub> undergoes a preferential phase orientation change, as well as the increasing formation of Cu-rich phases such as Cu<sub>3</sub>SbSe<sub>3</sub> and Cu<sub>3</sub>SbSe<sub>4</sub> due to the partial decomposition of CuSbSe<sub>2</sub> and due to the Sb losses.

Guo *et al.* [46] studied the annealing effect on the CuSbSe<sub>2</sub> films deposited by PLD. The annealing temperature was varied from 300–450 °C. Structural changes were characterized by XRD, which showed the most intense and sharp peaks for the CuSbSe<sub>2</sub> films annealed at 350 °C for 15 minutes, indicating that this condition is most suitable for the growth of CuSbSe<sub>2</sub> thin films in terms of crystalline quality.

Kim *et al.* [17] studied the effect of rapid thermal annealing at 350 °C for 30 minutes under a N<sub>2</sub> gas atmosphere on the CuSbSe<sub>2</sub> thin films prepared by co-sputtering process. The carrier concentration in the order of 10<sup>17</sup> cm<sup>-3</sup> and resistivity in the range 10<sup>0</sup>–10<sup>1</sup> Ω·cm, were determined for the annealed thin films. The annealed CuSbSe<sub>2</sub> thin films showed resistivity, carrier mobility, and carrier concentration 14.4 Ω·cm, 3.27 cm<sup>2</sup>/V·s, and 1.33 × 10<sup>17</sup> cm<sup>-3</sup>, respectively.

A selenization process at different annealing temperatures was also applied to improve the Sb<sub>2</sub>Se<sub>3</sub> thin film quality since Sb<sub>2</sub>Se<sub>3</sub> partially decomposes during the evaporation and the decomposition product Se has higher vapor pressure than Sb resulting in the formation of a Se deficient Sb<sub>2</sub>Se<sub>3</sub> film. A selenization treatment at 200 °C for the thermal evaporated Sb<sub>2</sub>Se<sub>3</sub> thin films has demonstrated a solar cell device efficiency improvement from 2.6% to 3.7% [80]. In another study, the selenization treatment of co-evaporated Sb<sub>2</sub>Se<sub>3</sub> films was found to improve conversion efficiency from 3.07% to 4.25%. [89] Similarly, sputtered Sb<sub>2</sub>Se<sub>3</sub> based solar cells with an efficiency of 6.06% have been achieved by tuning the post-selenization parameters [90]. An open-circuit voltage (*V*<sub>oc</sub>) exceeding 500 mV has been achieved with thin-film solar cells based on the sputtered and selenized Sb<sub>2</sub>Se<sub>3</sub> [91]. The selenization of Sb<sub>2</sub>Se<sub>3</sub> films improves the film quality and device performance in two ways: (1) compensating the Se loss during the deposition, which helps to reduce the *V*<sub>se</sub> related recombination; (2) forming a thin MoSe<sub>2</sub> layer at the Sb<sub>2</sub>Se<sub>3</sub>/Mo interface, eliminating the Schottky barrier and reducing the recombination at the back interface [92]. Rijal *et al.* [92] systematically investigated the impact of post-deposition annealing temperature on the structural and morphological properties of Sb<sub>2</sub>Se<sub>3</sub> thin films deposited on Mo-coated glass substrates by CSS technique. It was found that the selenization temperature of 425 °C was beneficial to increase the grain size, crystallinity and orientation of the Sb<sub>2</sub>Se<sub>3</sub> films. In addition, the Se loss during the CSS deposition was found to be compensated by the selenization process leading to a significant device performance improvement up to 6.43% [92].

## 1.4 Photoluminescence spectroscopy

Photoluminescence spectroscopy is one of the most sensitive methods for studying defects and photoexcited carrier recombination mechanisms in semiconductors. Knowing the defects in a semiconductor material, it is possible to modify the technology of the material production to change its electrical and optical properties according to our needs. Consequently, we have used this technique in this work for studying the defects and related recombination mechanisms in Sb<sub>2</sub>Se<sub>3</sub> and CuSbSe<sub>2</sub>.

Photoluminescence is the optical radiation emitted by a physical system resulting from excitation to a non-equilibrium state by irradiation with light [93]. As schematically shown in Figure 6, an electron-hole pair is generated as a result of absorption of light with an energy exceeding the bandgap energy of the material. Depending on the energy

of the excitation, in the case of an excess energy, the absorption is followed by thermalization of carriers to the band edges giving the released energy to the crystal lattice. Upon returning to equilibrium state, electron and hole will recombine, which results in the emission of a photon. Depending on the defects, which are present in the studied material, different radiative transitions can be observed, see Figure 6. PL emission arising from different recombination channels results in different behavior with varying temperature and laser power. Hereby we shortly introduce the characteristic features of most common radiative recombination mechanisms, including band-to-band, donor-to-band and band-to-acceptor (also known as free-to-bound), and donor-acceptor pair recombination.

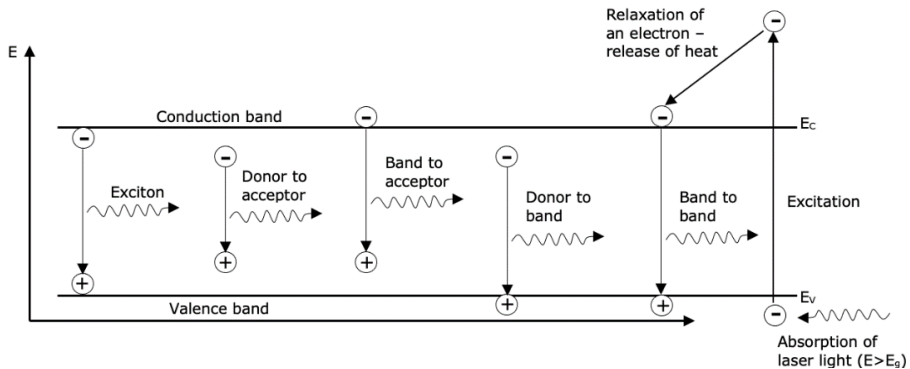


**Figure 6.** Most common radiative transitions observable with photoluminescence spectroscopy.

#### 1.4.1 Band-to-band photoluminescence

Band-to-band (BB) recombination takes place between the free electrons and holes in the conduction and valence band, respectively [94]. The corresponding PL band position, which is at about the bandgap energy of the semiconductor, follows the temperature dependence of the bandgap energy. The integrated intensity of the PL band  $\Phi$  originating from the BB recombination follows the  $\Phi \sim P^m$  ( $P$  is laser power) relation with  $m \sim 1$ .

#### 1.4.2 Excitonic transitions

Excitons are usually formed at low temperatures, where Coulomb attraction between electrons and holes is relevant. The annihilation of such bound electron-hole pair results in PL emission with an energy close to the bandgap energy of the material, the difference from the band gap being equal to the binding energy of the exciton. Also, the exciton band position follows the temperature dependence of the bandgap energy. The intensity of an excitonic emission will decrease fast when the thermal energy overcomes the exciton binding energy, being therefore thermally activated process. The energetic position of an exciton emission band is not affected by the excitation intensity. The integrated intensity of the PL band  $\Phi$  originating from the excitonic transitions follows the  $\Phi \sim P^m$  relation with  $m > 1$ .

#### 1.4.3 Free-to-bound PL (FB)

Band-to-band recombination usually dominates at high temperatures, where all the shallow impurities are ionized. At low temperatures, where the thermal energy of carriers is smaller than the ionization energy of the defects and carriers are frozen on

impurities [94], a free-to-bound recombination can occur. FB recombination involves a free carrier (electron or hole) and a charge (electron or hole) bound to a defect.

The emitted photon energy,  $E_{max}$  resulting from a free-to-bound recombination involving an acceptor defect is described as (2):

$$E_{max} = E_g - E_A, \quad (2)$$

where  $E_g$  is the band gap energy and  $E_A$  is the ionization energy of an acceptor, which can be determined from the thermally activated quenching process of the FB emission. With increasing excitation power, FB PL band peak position does not change. The integrated intensity of the PL band  $\Phi$  originating from the FB recombination follows the  $\Phi \sim P^m$  relation with  $m < 1$ .

#### 1.4.4 PL from donor-acceptor pair (DAP) recombination

When there are both, donor and acceptor defects in the semiconductor, donor-acceptor transitions can occur. Under illumination, electrons and holes can be trapped forming neutral donors ( $D^0$ ) and neutral acceptors ( $A^0$ ) at the sites of ionized donors ( $D^+$ ) and ionized acceptors ( $A^-$ ). In returning to equilibrium state some of the electrons on the neutral donors will recombine radiatively with holes on the neutral acceptors and can be represented by the reaction (3) [94]:



There is an attractive Coulomb potential between the charged donor and acceptor, this additional energy is also transferred to the emitted photon. The donor-acceptor pair (DAP) emission band position can be calculated by the following equation (4) [94,95]:

$$E_{max} = E_g - E_A - E_D + e^2 / (4\pi\epsilon_0\epsilon R) \quad (4)$$

where  $E_g$  is the band gap energy,  $E_A$  and  $E_D$  are the acceptor and donor ionization energies, respectively,  $e$  is the electron charge,  $\epsilon$  is the static dielectric constant,  $\epsilon_0$  is the permittivity of vacuum, and  $R$  is the distance between the donor and the acceptor.

As excitation power density increases, the recombination involving more distant DAPs saturates and mainly closer pairs having stronger Coulomb-interaction energy dominate the recombination, resulting in the characteristic blue-shift of the DAP band with increasing laser power. The blue-shift is usually in the order of 5-10 meV.

In the case of the DAP emissions, once the shallower defect forming the pair is ionized, the FB transition will start to dominate.

### 1.5 Summary of the literature review and aim of the thesis

Based on the literature, a considerable effort has been invested to gain a better and deeper understanding of structural, electrical and optical properties of binary and ternary Sb-based chalcogenide semiconductors aiming at their possible applications in photovoltaics. CuSbSe<sub>2</sub> and Sb<sub>2</sub>Se<sub>3</sub> appear to be a promising absorber materials for thin-film solar cells due to their attractive optical and electrical properties, as well as earth-abundant, low-cost and low-toxic constituent elements. CuSbSe<sub>2</sub>-based solar cell has reached to 4.7% and Sb<sub>2</sub>Se<sub>3</sub>-based solar cell has established a very rapid growth reaching 10.12% in short time, these are still much lower than the theoretically expected value

which is higher than 30%. One of the limiting factors for achieving higher efficiency of the devices is high recombination losses. As defects play a crucial role in determining the solar cell device performance, this thesis is dedicated to the studies of defects and recombination mechanisms in  $\text{CuSbSe}_2$  and  $\text{Sb}_2\text{Se}_3$  absorber materials by photoluminescence spectroscopy. At the beginning of this doctoral study, there were no photoluminescence studies of  $\text{CuSbSe}_2$  and  $\text{Sb}_2\text{Se}_3$  absorber materials available in the literature. Therefore, the objectives of this thesis are the following:

1. to prepare  $\text{CuSbSe}_2$  and  $\text{Sb}_2\text{Se}_3$  polycrystalline materials with homogeneous elemental and phase composition and to study their defect structure and related recombination mechanisms by photoluminescence spectroscopy.
2. to optimize the magnetron co-sputtering conditions and annealing parameters of the  $\text{CuSbSe}_2$  thin films and to investigate the changes in the morphology, structural properties and elemental and phase composition of the films depending on the annealing conditions.
3. to fabricate  $\text{CuSbSe}_2$  based thin film solar cells and characterize the photovoltaic properties of these devices.

## 2 Experimental details

This chapter describes the preparation methods applied for the synthesis of CuSbSe<sub>2</sub> and Sb<sub>2</sub>Se<sub>3</sub> polycrystalline samples (papers I, II), as well as the magnetron sputtering method used to deposit CuSbSe<sub>2</sub> thin films (paper III) and the characterization methods used to analyse the obtained materials and devices.

### 2.1 Preparation of CuSbSe<sub>2</sub>

CuSbSe<sub>2</sub> polycrystalline material was synthesized by the molten phase reaction method (Paper I). To obtain a single-phase polycrystalline material, 11 samples with different chemical compositions and 3 different synthesis routes in the temperature region 450–900 °C was investigated. Also different precursor materials including binaries Cu<sub>2</sub>Se and Sb<sub>2</sub>Se<sub>3</sub>, or elementary Cu, Sb, and Se were experimented. The most homogeneous material was synthesised from high purity precursor materials Cu, Sb<sub>2</sub>Se<sub>3</sub>, and Se (purchased from Alfa Aesar). The precursor materials were weighted in appropriate ratios (Cu:Sb:Se is 1:1:2) to produce 0.5 g of CuSbSe<sub>2</sub> and ground in an agate mortar, and the mixture was loaded into a quartz ampoule and degassed. According to the literature, the melting temperature of the stoichiometric CuSbSe<sub>2</sub> is 481 ± 3 °C [96]. The synthesis was performed above the melting point of the material. The stoichiometric mixture of precursors was heated up in a furnace from room temperature (RT) to 900 °C for 3 hours and maintained at this temperature for 1 hour. High temperature is used to increase the rate of reaction in liquid phase. After that, the ampoule was taken out from the furnace and quenched into cold water. The resulting polycrystalline ingot had a diameter of about 6 mm and a length of ~10 mm. For analysis, the ingot was broken into pieces.

### 2.2 Preparation of Sb<sub>2</sub>Se<sub>3</sub>

Sb<sub>2</sub>Se<sub>3</sub> polycrystals were prepared by isothermal annealing the commercial high purity (99.999%) Sb<sub>2</sub>Se<sub>3</sub> powder (purchased from Alfa Aesar) in sealed quartz ampoules at T = 350 °C in Ar atmosphere (100 Torr) in the presence of additional Se source for 30 minutes (Paper II). Post-treatment in Se vapor was performed because the commercial Sb<sub>2</sub>Se<sub>3</sub> failed to provide any PL signal. The post-treatment conditions were found to be the optimal for Sb<sub>2</sub>Se<sub>3</sub> thin films studied in parallel [80,92] to obtain photoconductive Sb<sub>2</sub>Se<sub>3</sub> with uniform stoichiometric composition.

### 2.3 Preparation of CuSbSe<sub>2</sub> thin films and solar cells

This section describes the pre-treatment process of the soda-lime glass substrates, deposition parameters of magnetron sputtering for CuSbSe<sub>2</sub> thin films, the post-annealing conditions, buffer layer deposition by chemical bath deposition and window layer deposition by RF sputtering and the fabrication of solar cells (Paper III).

#### 2.3.1 Preparation of the substrates

Soda-lime glass (SLG) substrates were cleaned in sulfuric acid in ultrasonic cleaner at 50 °C for 10 minutes, washed by deionized water, then dried by air flow and kept under ultraviolet lamp for 10 minutes.

### 2.3.2 Preparation and deposition of $\text{CuSbSe}_2$ thin films by magnetron sputtering

In this study, to deposit molybdenum (Mo) as back contact and  $\text{CuSbSe}_2$  thin films as absorber layers was used magnetron sputtering system by Angstrom Engineering Evovac 030 with three sputtering sources with glow discharge (Figure 7).

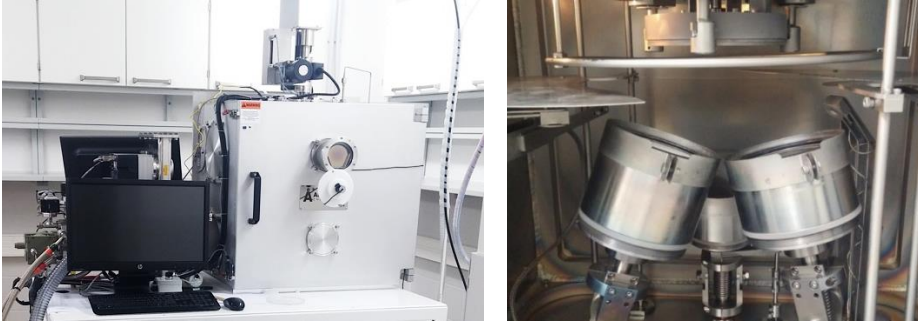


**Figure 7.** Photograph of Angstrom Engineering Evovac 030 with three sputtering sources with glow discharge and the substrate holder and 3 target holders.

The magnetron sputtering system contains the deposition chamber (schematic image is presented in Figure 8), cooling system, low vacuum pump, high vacuum cryopump, the substrate holder and 3 target holders. The substrate is at the top of the chamber and the targets are at the bottom of the chamber.

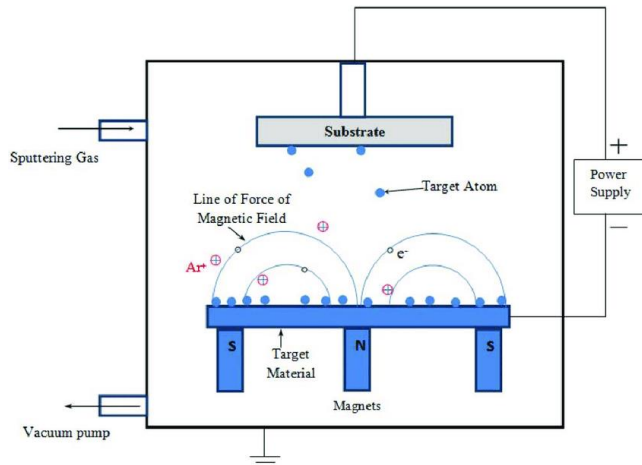


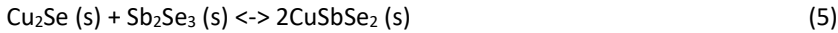
**Figure 8.** Schematic image of magnetron sputtering chamber [50].

After cleaning the SLG substrates, Mo layer as back contact was deposited by DC magnetron sputtering at substrate temperature of  $400\text{ }^\circ\text{C}$  under Ar pressure of  $0.67\text{ Pa}$  for 50 minutes.

$\text{CuSbSe}_2$  thin films were deposited by co-sputtering method from binary targets of  $\text{Cu}_2\text{Se}$  (DC) and  $\text{Sb}_2\text{Se}_3$  (RF). In order to obtain  $\text{CuSbSe}_2$  thin films with good adhesion, crystallinity and homogenous composition, 19 test series were experimented by varying the substrate temperature - RT,  $300\text{ }^\circ\text{C}$ ,  $350\text{ }^\circ\text{C}$ ,  $380\text{ }^\circ\text{C}$ ,  $400\text{ }^\circ\text{C}$ . The purity of both targets

was 99.99% (Testbourne Ltd). The rotational speed for glass substrate was 2 rpm. The distance between the substrate (10 cm × 10 cm size) and the targets was set as 12 cm. The background pressure of the vacuum chamber was  $9.3 \times 10^{-5}$  Pa and the process pressure was 0.53 Pa. The applied DC power for Cu<sub>2</sub>Se was varied between 18 to 27 W and RF power for Sb<sub>2</sub>Se<sub>3</sub> was varied between 58 to 88 W.

Cu<sub>2</sub>Se reacts with Sb<sub>2</sub>Se<sub>3</sub> phase to form CuSbSe<sub>2</sub> as expressed in Equation (5):



Based on the above experiments, the CuSbSe<sub>2</sub> thin films that were deposited for 50 min at a substrate temperature of 350 °C with a sputtering power of 27 W for Cu<sub>2</sub>Se and 88 W for Sb<sub>2</sub>Se<sub>3</sub> were selected for subsequent selenization experiments.

### 2.3.3 Post-annealing – selenization

The as-deposited CuSbSe<sub>2</sub> films were post-annealed in selenium vapor in a dual zone heating tube furnace (Figure 9). Selenization was done in the degassed and sealed quartz ampoules. The sample was placed at one end of the ampoule and the Se granule at the other end. Temperatures of both zones were controlled separately.

Temperature of the sample side was varied from 380 to 420 °C, the annealing time was varied from 10 to 60 minutes and the vapor pressure of selenium was kept constant at 133.32 Pa (360 °C). After selenization, all samples were cooled down naturally to room temperature.

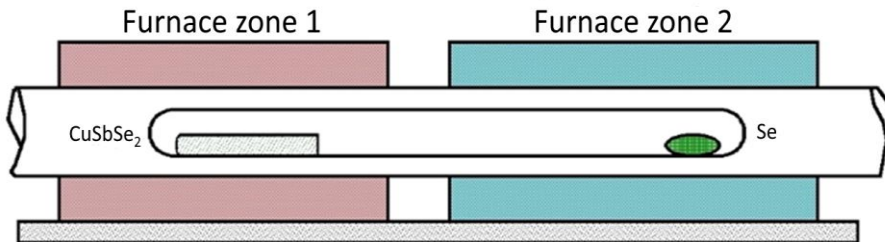


**Figure 9.** Schematic illustration of selenization in a dual zone heating tube furnace.

### 2.3.4 Buffer layer and window layer deposition

The potential of selenized thin films as a solar cell absorber was evaluated by fabricating the devices with the structure of SLG/Mo/absorber/CdS/*i*-ZnO/ZnO:Al. The CdS buffer layer was deposited by chemical bath deposition method and ZnO window layer by RF sputtering. ZnO consists of 2 layers: thin layer (40-50 nm) of intrinsic zinc oxide (*i*-ZnO) and thicker layer of ZnO:Al (300-500 nm) - doped with 2% of aluminum to improve conductivity. Base pressure in the chamber was  $2-6 \times 10^{-6}$  Torr, working pressure was  $3-4 \times 10^{-2}$  Torr. Power for RF sputtering was 100 W. For deposition of *i*-ZnO layer, the flow rate of oxygen was 7.5 SCCM (cm<sup>3</sup>/min) and the flow rate of argon was 22.5 SCCM for 5 minutes. For ZnO:Al layer deposition, the argon flow with rate 30 SCCM for 45 minutes were used without oxygen. Oxygen is required for stable stoichiometric composition of *i*-ZnO and to increase shunt resistance.

CdS was deposited from an aqueous solutions containing 0.02 M cadmium acetate dihydrate (Cd(CH<sub>3</sub>COO)<sub>2</sub>•2H<sub>2</sub>O) as source of Cd, 0.35 M thiourea (SC(NH<sub>2</sub>)<sub>2</sub>) as source of S, 2 M ammonium hydroxide (NH<sub>4</sub>OH) as a buffer solution for keeping the pH at 11.6.

The deposition time was 10 minutes and temperature was 60 °C. The buffer layer deposition recipe has been previously developed in PV lab. Prior to CdS deposition, the selenized films were etched with 10 wt. % KCN alkaline solution for 60 seconds to remove undesired Cu-Se phases.

## 2.4 Characterization methods

The synthesized materials were investigated using Raman scattering, X-ray diffraction (XRD), Energy Dispersive X-ray Spectroscopy (EDX), photoreflectance and temperature as well as laser power dependent photoluminescence spectroscopy (PL) to determine the crystallographic properties, phase composition, band gap energy and defects dominating in the radiative recombination processes, respectively.

Room-temperature micro-Raman spectra were recorded by using a Horiba's LabRam HR800 spectrometer with a spectral resolution better than  $1\text{ cm}^{-1}$ . A YAG: Nd laser with a wavelength of 532 nm was used for excitation and the signal was detected with a cooled multichannel CCD detection system. The laser spot size on the sample is around  $10\text{ }\mu\text{m}$  in diameter.

For the temperature dependent PL measurements, a closed-cycle helium cryostat (Janis CCS-150) was employed, enabling the measurements in the temperature range from 10 K to 300 K. 442 nm line of a He-Cd laser was used for the PL excitation. The laser power incident on the material was varied by using neutral density filters. The laser spot size for these measurements was  $\sim 200\text{ }\mu\text{m}$  in diameter. A 0.64 m focal length and 600 lines/mm grating monochromator was used for resolving the spectra. For PL signal detection a Hamamatsu InGaAs photomultiplier tube was used.

The crystal structure of the studied samples was determined by XRD by using a Rigaku Ultima IV diffractometer with monochromatic Cu K $\alpha$ 1 radiation ( $\lambda = 1.5406\text{ \AA}$ ) at 40 kV and 40 mA operating with the silicon strip detector D/teX Ultra. The lattice constants were determined using the Rietveld refinement procedure by Rigaku PDXL version 1.4.0.3 software.

The evolution of the surface morphology and the thickness of films was performed with high-resolution scanning electron microscope (HR-SEM Zeiss Merlin). An operating voltage of 3 kV was used for imaging. The chemical composition was determined using an energy dispersive x-ray analysis (EDS) system (Bruker EDX-XFlash6/30 detector). For EDS analysis an operating voltage 10 kV (and 20 kV for mapping) was used and the concentrations of elements were calculated by using PB-ZAF standardless mode.

The photoreflectance (PR) measurements were made with a traditional setup [97], where the 0.64 m focal length grating monochromator together with a 250 W halogen bulb as a primary beam and a 45 mW He-Cd laser line (441 nm) as a secondary beam, were used. The reflectance signal at 85 Hz was detected using a Si detector with a lock-in amplifier in the spectral range from 1.1 to 1.3 eV.

Photovoltaic properties of devices based on CuSbSe<sub>2</sub> films were analyzed by current-voltage characteristics (*I*-*V*) and external quantum efficiency (EQE) measurements. *I*-*V* characteristics were measured under the  $100\text{ mW/cm}^2$  illumination using a Keithley 2400 Source Meter. EQE measurements were done using a computer-controlled SPM-2 monochromator and a 100 W halogen-tungsten light source.



### 3 Results and discussion

In this paragraph, the first two sections (3.1 and 3.2) present the results of structural, compositional and optical properties of synthesized polycrystalline  $\text{CuSbSe}_2$  and  $\text{Sb}_2\text{Se}_3$  materials. The third section (3.3) is dedicated to the results of structural and compositional properties of co-sputtered and post-annealed  $\text{CuSbSe}_2$  films, as well as the optoelectronic properties of the solar cell devices based on these thin films.

#### 3.1 Structural and elemental composition of $\text{CuSbSe}_2$ polycrystalline samples

##### 3.1.1 EDX, XRD and Raman analyzes of polycrystalline $\text{CuSbSe}_2$

According to the EDX analysis, the bulk composition of synthesized  $\text{CuSbSe}_2$  polycrystalline material was Sb-rich with elemental composition: Cu 24.0 at.%, Sb 26.0 at.%, and Se 50.0 at.%, which corresponds to the chemical formula  $\text{Cu}_{0.96}\text{Sb}_{1.04}\text{Se}_2$ . The uniformity of polycrystalline sample was analyzed by EDX mapping, which shows distribution of elements in material. An example of the EDX mapping of a  $\text{CuSbSe}_2$  polycrystalline material is presented in Figure 10. (paper I). The black and white image shows SEM image of cross-section of polycrystalline  $\text{CuSbSe}_2$  sample, colored images show distribution of individual elements – copper (blue), antimony (red) and selenium (green) and the middle image of EDX mapping shows uniform distribution of all elements. A minor contribution of  $\text{Sb}_2\text{Se}_3$  was also detected by EDX in the studied samples.

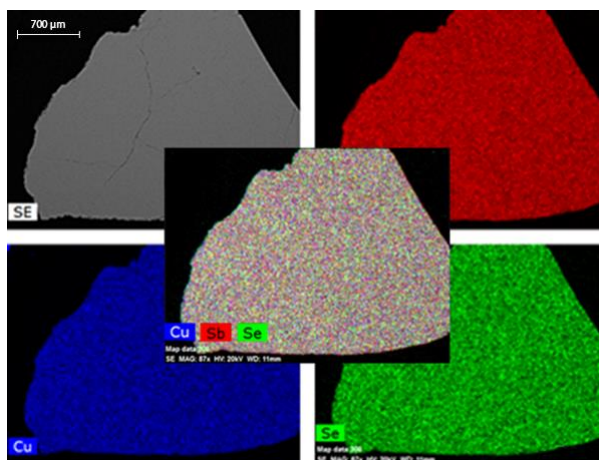


**Figure 10.** Elemental mapping of a synthesized  $\text{CuSbSe}_2$  polycrystalline material by EDX.

The phase and crystal structure was analyzed by XRD and Raman spectroscopy. Figure 11 presents the XRD pattern of the studied material mainly consisting of the characteristic peaks of  $\text{CuSbSe}_2$  with orthorhombic structure  $Pnma$ . The determined lattice parameters  $a = 6.308 \text{ \AA}$ ,  $b = 3.985 \text{ \AA}$ , and  $c = 15.014 \text{ \AA}$  are in good agreement with the experimental data in the literature [98,99]. XRD analysis also revealed the minor contribution of elemental selenium (Se-b JDPDF 01-073-2121).

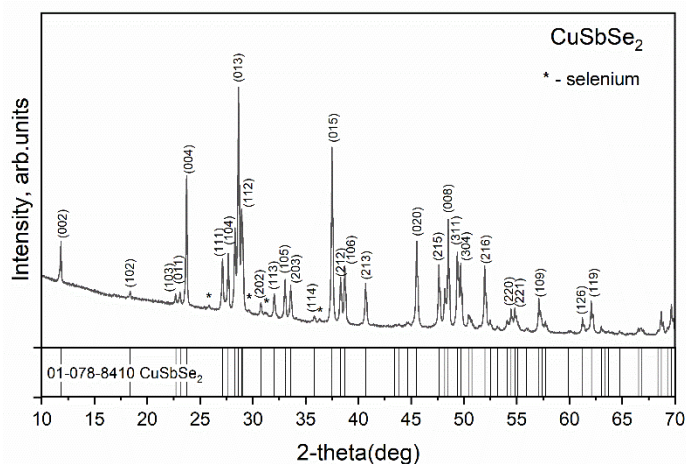


**Figure 11.** XRD pattern of the studied  $\text{CuSbSe}_2$  polycrystalline material.

Due to the superposition between the peaks in the XRD pattern of the  $\text{CuSbSe}_2$  and some of the secondary phases, micro-Raman spectroscopy was used as a comparative method for the phase analysis of the synthesized compounds. The Raman spectrum of the  $\text{CuSbSe}_2$  polycrystalline material is presented in Figure 12 showing the characteristic peaks of  $\text{CuSbSe}_2$  at  $103$ ,  $139$ , and  $214 \text{ cm}^{-1}$ . In addition, minor contribution of  $\text{Sb}_2\text{Se}_3$  (the shoulder peak at  $189 \text{ cm}^{-1}$  [100]) to the Raman spectrum was detected. The Raman peaks at  $103$ ,  $139$ , and  $214 \text{ cm}^{-1}$  are in correspondence with the data presented in [41] and were assigned to the  $A_g$ ,  $B_{2g}$ , and  $A_g$  vibrational modes of  $\text{CuSbSe}_2$ , respectively [24].

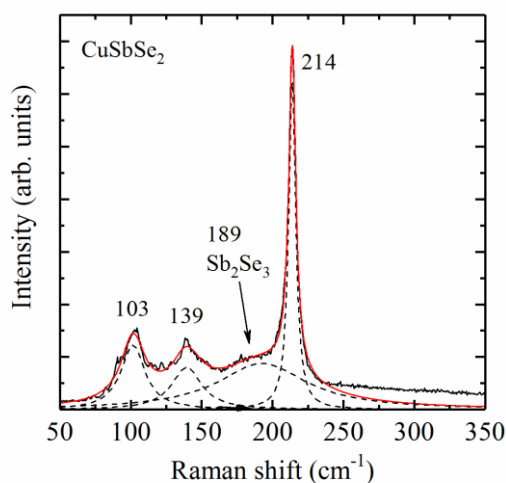


**Figure 12.** Raman spectrum of the studied  $\text{CuSbSe}_2$  polycrystalline material showing characteristic peaks of  $\text{CuSbSe}_2$  at  $103$ ,  $139$ , and  $214 \text{ cm}^{-1}$ . The dashed lines represent the fitting of the spectrum with Lorentz peaks.

### 3.1.2 Photoluminescence studies of polycrystalline CuSbSe<sub>2</sub>

A detailed photoluminescence analysis of the synthesized CuSbSe<sub>2</sub> polycrystalline material using various temperatures and laser excitation powers was performed. The temperature and laser power dependencies of the PL spectrum of CuSbSe<sub>2</sub> are shown in Figures 13(a) and 13(b), respectively. The PL spectrum of CuSbSe<sub>2</sub> at  $T = 10$  K consists of three asymmetric PL bands at 1.28 eV, 1.17 eV, and 0.90 eV, named PL1, PL2, and PL3, respectively.

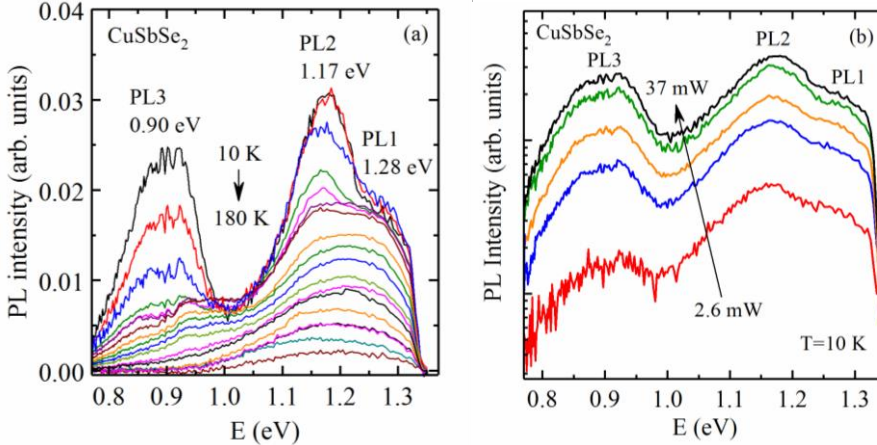


**Figure 13.** (a) Temperature and (b) laser power dependencies ( $T = 10$  K) of the PL spectrum of CuSbSe<sub>2</sub>. Three PL bands at 1.28 eV (PL1), 1.17 eV (PL2), and 0.90 eV (PL3) at  $T = 10$  K were detected.

The detected PL bands have a slightly asymmetrical shape with an exponential slope on the low-energy side and were therefore fitted with an empirical asymmetric double sigmoidal function [101] for the detailed analysis of the PL bands.

In general, the asymmetric shape of the PL bands is common to compensated multinary semiconductors with a high concentration of native defects that induce spatial potential fluctuations to the material [102–104].

The potential fluctuations will lead to a local perturbation of the band structure, also broadening the defect level distribution and forming band tails enabling additional recombination paths for the light-generated charge carriers. From the laser power dependence of the low-temperature PL spectrum of CuSbSe<sub>2</sub> (Figure 13b), a blueshift of the PL1 and PL2 bands with increasing excitation power was detected with the magnitudes of 8 meV/decade and 12 meV/decade, respectively. The peak position of the PL3 band did not vary with the laser power. A large blueshift observed for the PL1 and PL2 bands is typical for the recombination in a material including spatial potential fluctuations and/or bandgap fluctuations and band tails [101,102]. The dependence of the integrated intensity  $\Phi(P)$  of PL bands on the excitation laser power  $P$  is following the sublinear dependence  $\Phi \sim P^m$  as can be seen in Figure 14. Unfortunately, the PL bands labelling was not correct in the paper I. The power coefficient  $m$  can be found as the gradient of the  $\Phi(P)$  plot on a log-log scale as shown in Figure 14(a) giving values  $m = 1.06$ ,  $m = 0.72$ , and  $m = 0.63$  for the studied PL bands PL3, PL2, and PL1, respectively. The detected  $m$  values for PL2 and PL1 bands that are smaller than unity indicate the radiative recombination of charge carriers localized at defects within the bandgap [105].

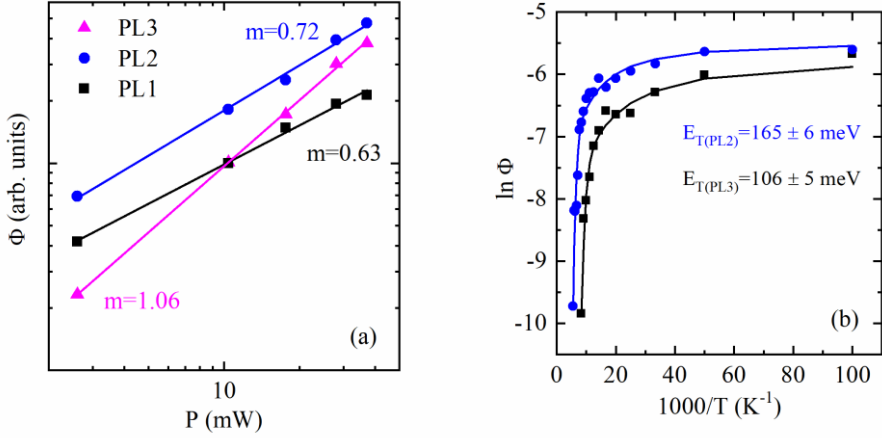


**Figure 14.** (a) Integrated PL intensity  $\Phi$  of different PL bands as a function of the laser power  $P$ . The lines are least squares fit to the data. (b) Temperature dependencies of the integrated intensities of the PL bands; solid lines present the fitting results with Eq. (6).

Figure 14(b) presents the temperature dependencies of the integrated intensities of the PL bands  $\Phi$  from which the thermal activation energies were determined. The linear dependence of  $\ln \Phi(T)$  vs  $1000/T$  at high temperatures was fitted by using the theoretical expression (6) for discrete energy levels [106],

$$\Phi(T) = \frac{\Phi_0}{1 + \alpha_1 T^{3/2} + \alpha_2 T^{3/2} \exp(-E_T/kT)} \quad (6)$$

where  $\alpha_1$  and  $\alpha_2$  are the process rate parameters and  $E_T$  is the thermal activation energy.

Thermal activation energies  $165 \pm 6$  meV and  $106 \pm 5$  meV were obtained for the PL2 and PL3 bands in CuSbSe<sub>2</sub>, indicating the involvement of rather deep defects in the radiative recombination processes. There was no linear dependence of  $\ln \Phi(T)$  vs  $1000/T$  at high temperatures found for the PL1 band. The temperature dependencies of the peak positions of all three PL bands follow the temperature dependence of the bandgap energy as presented in [24]. The peak position close to the bandgap of CuSbSe<sub>2</sub> around 1.3 eV at  $T = 10$  K (considering that the bandgap at  $T = 300$  K is 1.2 eV as found in [27]) and the behavior of the PL1 band with temperature allow us to propose that this emission results from the band-to-band recombination that is usually an indication of good optoelectronic quality of the material. It was observed in the laser power dependence of the PL1 band that  $m = 0.63$ , which indicates to the defect related recombination. As a result, the origin of PL1 band remains open and needs further studies.

The integrated intensity and the peak position of the PL2 band show the dependence on temperature and laser power typical for the band-to-acceptor transition involving holes localized in the acceptor level and electrons in the conduction band. The obtained thermal activation energy obtained from the quenching of the PL2 band  $165 \pm 6$  meV resembles the position of the deep acceptor level from VBM. Rampino *et al.* [37] and Soliman *et al.* [38] also found deep acceptor defects with similar activation energy from the temperature dependent electrical conductivity measurements. Based on the DFT calculations [24], [36] the dominating acceptor defects with the lowest formation energy in Cu-poor CuSbSe<sub>2</sub> are  $V_{Cu}$  and  $Cu_{Sb}$ . As the ionisation energy of  $V_{Cu}$  is predicted to be

0.08 eV, which is much lower than the defect ionisation energy obtained from the PL measurements in this study, we attribute the detected deep acceptor to  $\text{Cu}_{\text{Sb}}$  antisite defect.

A thermal activation energy of PL3 band is  $106 \pm 5$  meV, which is rather small considering the bandgap of the  $\text{CuSbSe}_2$  at  $T = 10$  K. Such deep PL bands with low activation energy and no shift with laser power are often found to result from the deep donor—deep acceptor recombination in multinary chalcogenide semiconductors [107,108]. We cannot exclude that this PL3 band could also be related to the  $\text{Sb}_2\text{Se}_3$  secondary phase that was detected in the studied samples. Similar deep PL bands showing very small thermal activation energies (on the order of few tenths of meV only) were detected in closely related  $\text{CuSbS}_2$  [109] and attributed to free-to-bound recombination that, however, would require additional explanation of the large discrepancy between the bandgap and PL band position. Hence, such deep PL bands as is PL3 in this study should be investigated further.

## 3.2 Analysis of $\text{Sb}_2\text{Se}_3$ polycrystals

### 3.2.1 XRD and Raman studies of $\text{Sb}_2\text{Se}_3$ polycrystals

The XRD pattern and the Raman spectrum of the studied  $\text{Sb}_2\text{Se}_3$  polycrystals are presented in Figure 15(a) and Figure 15(b), respectively. According to the XRD analysis, the material crystallizes in orthorhombic structure of  $\text{Sb}_2\text{Se}_3$  with space group  $Pnma$  62 (ICDD: 01-083-7430). All detected XRD peaks belong to  $\text{Sb}_2\text{Se}_3$ , only main diffraction peaks are labelled for the clarity of the figure. The following lattice parameters were determined:  $a = 1.17833(10)$  nm,  $b = 0.39776(6)$  nm and  $c = 1.1634(2)$  nm being in correspondence with the data reported by other research groups [110].

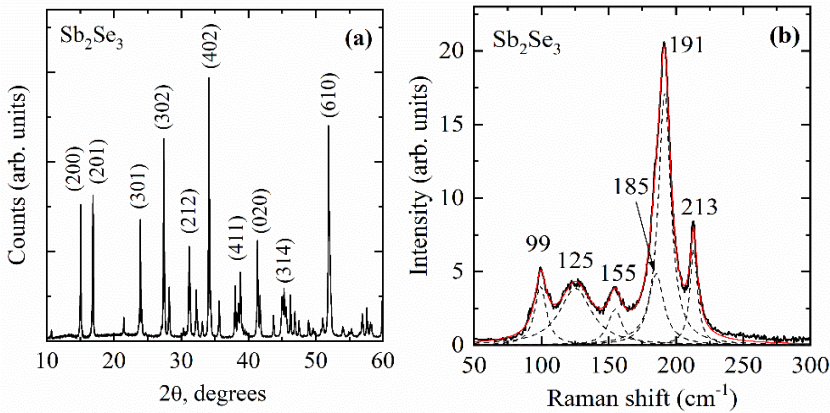


**Figure 15.** The XRD pattern (a) and the Raman spectrum (b) of the studied  $\text{Sb}_2\text{Se}_3$  polycrystals indicating to the single phase material.

The characteristic Raman spectrum of the studied  $\text{Sb}_2\text{Se}_3$  consisted of 6 Raman peaks at 99, 125, 155, 185, 191 and 213  $\text{cm}^{-1}$ , the Raman peak at 191  $\text{cm}^{-1}$  being the dominant one. The obtained Raman spectrum is in good correlation with the published data by Shongalova *et al.* [111] showing that the often found Raman mode around 250  $\text{cm}^{-1}$  that is absent in our samples is corresponding to  $\text{Sb}_2\text{O}_3$  instead of  $\text{Sb}_2\text{Se}_3$ . No contribution from the secondary phases to the XRD pattern and to the Raman spectrum of the studied material could be detected.

### 3.2.2 Photoreflectance study of Sb<sub>2</sub>Se<sub>3</sub> polycrystals

For determining the band gap of the studied Sb<sub>2</sub>Se<sub>3</sub> polycrystals, photoreflectance spectroscopy in the temperature range from 120 K to 300 K was used. The PR spectrum of Sb<sub>2</sub>Se<sub>3</sub> at  $T = 300$  K is presented in Figure 16. The measured PR spectra were analyzed by the low-field line-shape function with a third derivative functional form, developed by Aspnes [112]:

$$\frac{\Delta R}{R} = \text{Re}[Ae^{i\phi}(E - E_g + i\Gamma)^{-n}], \quad (7)$$

where  $E$  is the photon energy and  $A$ ,  $\phi$ ,  $E_g$ , and  $\Gamma$  are the amplitude, phase, optical transition energy, and broadening parameter of the spectrum, respectively. The exponent  $n$  in Eq. (7) depends on the type of the critical point, and determining its proper value is of particular importance in analyzing PR spectra.  $n = 2.5$ , corresponding to a three-dimensional critical point, was used for the fitting of all PR spectra. The band gap  $E_g = 1.182 \pm 0.010$  eV and the broadening parameter  $\Gamma = 74 \pm 12$  meV were found for Sb<sub>2</sub>Se<sub>3</sub> at  $T = 300$  K. The temperature dependence of the bandgap energy of Sb<sub>2</sub>Se<sub>3</sub> presented in the inset graph of Figure 16 is in very good agreement with the data presented in [58], however, they found slightly larger broadening parameter  $\Gamma = 82$  meV at  $T = 300$  K.

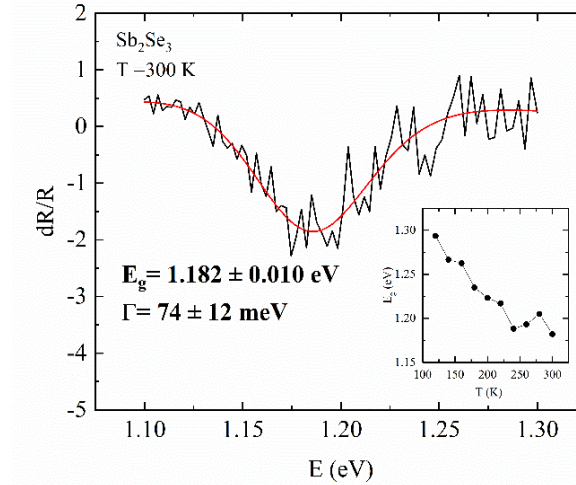


**Figure 16.** PR spectrum of the studied Sb<sub>2</sub>Se<sub>3</sub> crystals at  $T = 300$  K. The red solid line presents the fitting of the experimental data with Eq. (7). The inset graph presents the temperature dependence of the bandgap energy of the material determined from the PR spectra in the temperature region from 120 K to 300 K.

### 3.2.3 Photoluminescence study of Sb<sub>2</sub>Se<sub>3</sub> polycrystals

There was no detailed PL study of Sb<sub>2</sub>Se<sub>3</sub> available at the beginning of this doctoral study, so this is the first one.

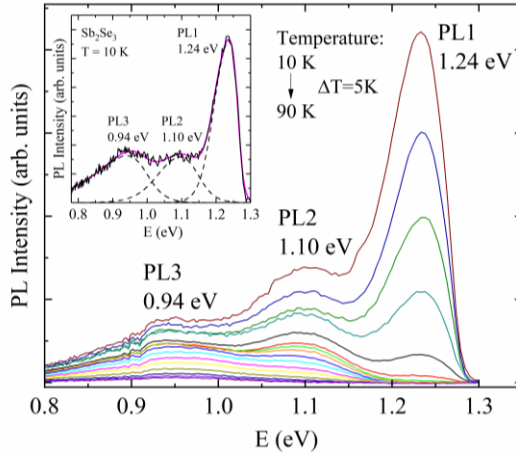


**Figure 17.** The temperature dependence of the PL spectrum of the studied  $Sb_2Se_3$  polycrystals. The inset figure presents an example of the fitting of the spectra.

The temperature dependence of the PL spectrum of the studied  $Sb_2Se_3$  polycrystals in the temperature region from  $T = 10$  K to  $T = 90$  K is presented in Figure 17. The inset graph presents the fitting of the spectrum at  $T = 10$  K with an empirical asymmetric double sigmoid function [101] resulting in three PL bands positioned at 1.24 eV (labelled PL1), at 1.1 eV (labelled PL2) and at 0.94 eV (labelled PL3). To determine the type of recombination, the temperature and laser power dependencies of the PL emission were measured. The PL bands had slightly asymmetric shape with a steeper decline at high-energy side and nearly temperature independent incline at the low energy side that is common in semiconductors with band tails [102]. The average depth of the band edge fluctuations determined from the low energy side of the PL1 band at  $T = 10$  K according to [102] is  $\gamma = 17$  meV, which is smaller than the Urbach energy 38 meV at  $T = 300$  K found by Chen *et al.* in [54] indicating to the good quality of our studied polycrystals. The temperature dependence of the PL bands positions (Figure 18(a)) revealed a slight shift towards higher energies in the case of the PL1 and PL3 bands. PL2 band peak position shows a red-shift larger than the temperature dependence of the band gap [58].

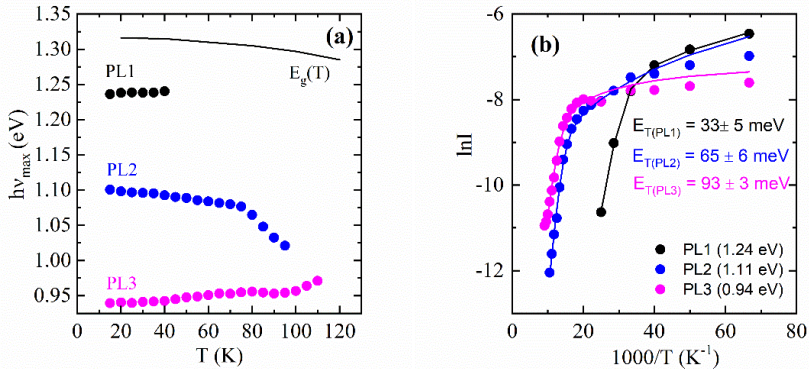


**Figure 18.** The temperature dependence of the PL band peak positions together with the band gap energy  $E_g$  from Ref. [54] presented as solid line (a), and the Arrhenius plot (b) showing the thermal activation energies for the studied three PL bands in  $Sb_2Se_3$  obtained from the fitting of the curves with Eq. (6).

The thermal activation energies for the bands obtained from the Arrhenius plot (Figure 18b) where the dependence of  $\ln(I/T)$  versus  $1000/T$  at high temperatures was fitted by using theoretical expression (6) for discrete energy levels [106].

As predicted by the fast quenching of the PL spectra with temperature (see Figure 18) small thermal activation energies  $E_T(\text{PL1}) = 33 \pm 5$  meV,  $E_T(\text{PL2}) = 65 \pm 6$  meV and  $E_T(\text{PL3}) = 93 \pm 3$  meV were obtained.

Considering the low temperature band gap of  $\text{Sb}_2\text{Se}_3$   $E_g = 1.32$  eV [58,59], the positions of the detected PL bands at  $T = 10$  K being quite distant from the band gap, and the obtained small thermal activation energies, one can propose that the PL1 and PL3 bands most probably arise from the donor-acceptor pair (DAP) recombination. The presence of high concentration of donor-acceptor pairs is also predicted by the theoretical calculations [66].

To analyze the recombination mechanisms behind the PL bands, also the laser power dependence of the PL spectra was measured at  $T = 10$  K, see Figure 19. The inset graphs present the laser power dependencies of the PL bands positions and intensities. The dependence of the integrated intensity  $\Phi(P)$  of PL bands on the excitation laser power  $P$  is following the dependence  $\Phi \sim P^m$  as can be seen from the inset graph in Figure 19. The power coefficient  $m$  can be found as the gradient of the  $\Phi(P)$  plot on a log-log scale as shown in upper inset graph in Figure 19 giving  $m \sim 0.6$  for all three PL bands. The detected  $m$  value which is smaller than unity indicates to the radiative recombination of charge carriers localized at defects within the band gap for all three PL bands [105].

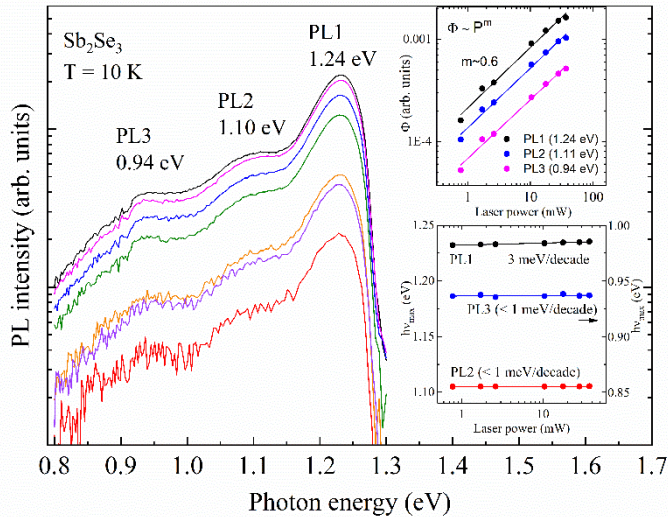


**Figure 19.** The laser power dependence of the PL bands of  $\text{Sb}_2\text{Se}_3$  at  $T=10$  K. The inset graphs present the laser power dependencies of the PL bands peak positions (bottom graph) and intensities (upper graph).

The peak position of the PL2 and PL3 bands varied only slightly (less than 1 meV/decade) with the laser power. A blueshift of the PL1 band with increasing excitation power was detected with the magnitude of 3 meV/decade, which is characteristic to donor-acceptor pair recombination as well as to a semiconductor involving band tails [102]. The emission energy from a donor-acceptor pair separated by a distance  $R$  can be calculated by the equation (4) [95]. The relatively small shift of the PL3 band with laser



power and rather “deep” peak position indicate to the DAP recombination via very close donor-acceptor pairs, while the PL1 band involves DAP with larger distance between donor and acceptor defects.

Due to a low symmetry of  $\text{Sb}_2\text{Se}_3$  crystal lattice, 2 different lattice sites for Sb and 3 different sites for Se exist (see Figure 5) [55]. The closest distance  $R = 0.2588$  nm is between Se(1) and Sb(2) sites corresponding to the Coulomb energy of 232 meV ( $\epsilon = 24$  [54]). Considering the peak position of the PL3 band, the thermal activation energy, and the bandgap energy of  $\text{Sb}_2\text{Se}_3$ , similar value for the Coulomb energy for the PL3 band is expected. Accordingly, our results show that we have a donor-acceptor pair, where the donor and acceptor defects occupy closest Se and Sb sites in the lattice.

These so-called deep donor-deep acceptor pairs (DD-DA) were discovered previously in CdTe [113], in chalcopyrites [114], and in kesterites [107]. It is known that the electron (hole) wave function in the deep donor (acceptor) level must be highly localized. Therefore, for more distant pairs, there is practically no overlapping of carriers’ wave functions and, consequently, no observable recombination emission. According to [66] all single defects in  $\text{Sb}_2\text{Se}_3$  are quite deep and therefore they indeed can form DD-DA pairs. When paired, single acceptor and donor defect levels are pushed towards band edges and the thermal activation energy of these complexes will become quite small. While the PL1 band of more distant pairs shows a certain blueshift with increased excitation intensity, the PL3 band corresponding to DD-DA pairs practically does not shift.

Moreover, DA pairs having somewhat larger separation and thus smaller Coulomb energy can cause the observed slightly asymmetric shape of the PL bands in addition to the broadening caused by the band tails. For example, Sb(1)-Se(3) sites are separated by the distance  $R = 0.2664$  nm and the corresponding Coulomb energy is only about 7 meV smaller than for the closest distance.

The shallowest single acceptor defect in slightly Se-rich  $\text{Sb}_2\text{Se}_3$  is  $\text{Se}_{\text{Sb}(1)}$  defect having a depth of about 100 meV [54,66]. We can assume, that this defect is a component of DA pair responsible for the PL1 band. The corresponding donor defect is not clear and requires further studies.

We can see that PL1 quenches very fast with temperature showing small thermal activation energy of 33 meV. As this PL band shifts slightly towards higher energies with increasing temperature, it is proposed to originate from donor-acceptor pair recombination. The same applies for PL3.

The PL2 band behaves differently from the PL1 and PL3 bands referring to a different type of recombination. According to Figure 18 (a), the PL2 band peak position shows a red-shift comparable or even slightly larger than the temperature dependence of the band gap energy and it is independent of the magnitude of the laser power. However, considering the PL2 band peak position, the low-temperature band gap of  $\text{Sb}_2\text{Se}_3$   $E_g = 1.32$  eV [58,59] and the thermal activation energy for this PL band, it cannot be attributed to a simple band-to-acceptor recombination. Moreover, the observed peak position shift with temperature is an indication of the involvement of the band states in the recombination process for the PL2 band. Therefore, the most probable origin of the PL2 band was proposed to be related to grain boundaries. There are different models about PL in the vicinity of grain boundaries, they all are based on band bending and thus on local reduction of bandgap energy or the depth of defect levels. In this case, the recombination can occur through tunnelling processes near grain boundaries, where a significant band bending is present. Similar model was proposed also for Z-bands in CdTe [115]. In the studied polycrystalline samples the concentration of grain boundaries is

quite high and therefore the intensity of the PL2 band is also relatively high. Of course, further studies must be performed to clarify this recombination related to grain boundaries.

### 3.3 Structural properties of as-deposited CuSbSe<sub>2</sub> thin films

This part is containing the results of the co-sputtered CuSbSe<sub>2</sub> thin films (Paper III).

#### 3.3.1 SEM, EDX and Raman analyzes of CuSbSe<sub>2</sub> thin films

Morphology of as-deposited CuSbSe<sub>2</sub> thin films were characterised by SEM. Figure 20a shows SEM images of the cross-section and Figure 20b the surface of as-deposited CuSbSe<sub>2</sub> thin film co-sputtered at 350 °C for 1 hour. Cross-sectional image of CuSbSe<sub>2</sub> absorber shows that a compact film with thickness around 1.4 μm was obtained. Top-view of the film shows that the surface of as-deposited film is heterogeneous. According to the EDX analysis, the as-deposited CuSbSe<sub>2</sub> polycrystalline thin films had Cu-poor composition with elemental concentrations: Cu 22.4 at%, Sb 27.3 at% and Se 50.3 at%. EDX elemental mapping analysis showed that the CuSbSe<sub>2</sub> thin films contain Sb- and Se-rich regions - Cu 15.3 at%, Sb 32.7 at%, Se 52.0 at% (yellow and pink coloured areas in the inset map in Figure 20b), which could correspond to Sb<sub>2</sub>Se<sub>3</sub> phase.

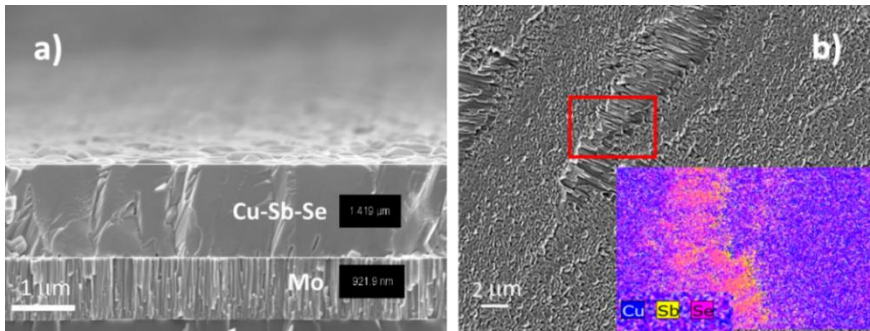


**Figure 20.** SEM images of a) cross-section and b) surface of as-deposited Cu-Sb-Se thin film sputtered at 350 °C. Enlarged view shows EDX elemental mapping of the surface regions of Sb<sub>2</sub>Se<sub>3</sub>.

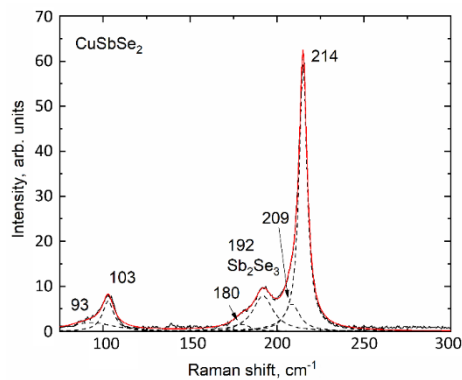


**Figure 21.** Raman spectrum of as-deposited CuSbSe<sub>2</sub> thin film together with the fitting using Lorentzian peaks.

Phase composition of the as-deposited film was determined by Raman analysis. Figure 21 shows Raman spectrum of as-deposited  $\text{CuSbSe}_2$  thin film with peaks at 93, 103, 180, 209, and 214  $\text{cm}^{-1}$ , which are attributed to  $\text{CuSbSe}_2$  phase [41]. Additionally, Raman peak at 192  $\text{cm}^{-1}$  was detected, which is assigned to  $\text{Sb}_2\text{Se}_3$  secondary phase [100].

According to XRD pattern presented in Figure 22a, as-deposited  $\text{CuSbSe}_2$  thin film consists of  $\text{CuSbSe}_2$  phase (PDF 01–083–9473), which crystallize in orthorhombic structure with space group  $Pnma$ . The determined lattice parameters for  $\text{CuSbSe}_2$   $a = 6.294 \text{ \AA}$ ,  $b = 4.015 \text{ \AA}$  and  $c = 14.905 \text{ \AA}$  are in good agreement with the literature data [98]. Additionally,  $\text{Sb}_2\text{Se}_3$  phase (PDF 03–065–2433) was detected, which crystallizes also in orthorhombic structure.

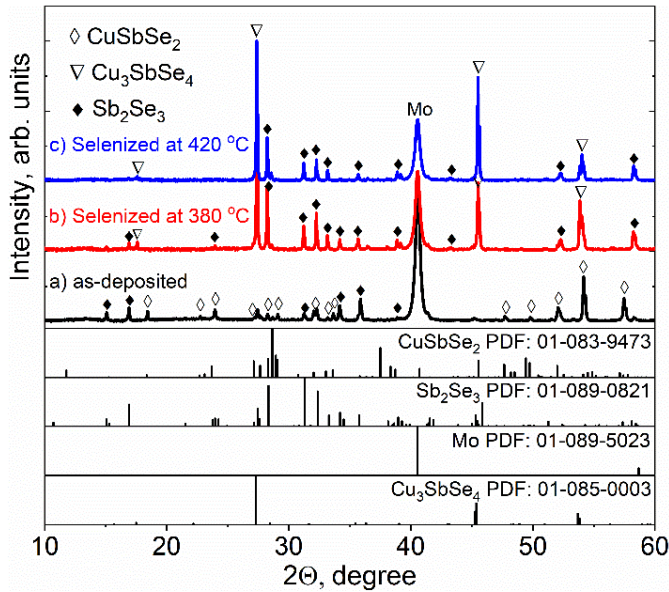


**Figure 22.** XRD patterns of a) as-deposited  $\text{CuSbSe}_2$  thin film, b) selenized at 380 °C and c) selenized at 420 °C.

### 3.3.2 Properties of selenized $\text{CuSbSe}_2$ thin films

In this part, post-deposition annealing was done in a dual zone heating tube furnace. As-deposited  $\text{CuSbSe}_2$  films were selenized at temperatures 380- 420 °C for 10 to 60 minutes under selenium vapor pressure of 133.32 Pa.

In Figure 22b and 22c are presented XRD patterns of the  $\text{CuSbSe}_2$  thin films after selenization at 380 °C and 420 °C, respectively. The strongest diffraction peaks can be perfectly indexed to a tetragonal structure  $\text{Cu}_3\text{SbSe}_4$  (PDF 01 85–0003; space group  $I-42m$ ) with lattice constants  $a = 5.645 \text{ \AA}$  and  $c = 11.237 \text{ \AA}$ , which are in good agreement with the experimental data in the literature [110]. In addition to  $\text{Cu}_3\text{SbSe}_4$ , the binary antimony selenide phase with the orthorhombic structure (ICDD # 01–089–0821, space group  $Pbnm$ ) with the unit cell parameters  $a = 11.617 \text{ \AA}$ ,  $b = 11.750 \text{ \AA}$ ,  $c = 3.972 \text{ \AA}$  was detected. Results suggest that selenization at selected temperatures leads to decomposition of  $\text{CuSbSe}_2$  to  $\text{Cu}_3\text{SbSe}_4$  and  $\text{Sb}_2\text{Se}_3$  [36].

Figure 23a and Figure 23b show SEM images of cross-section and surface of the films selenized at 380 °C for 10 and 60 minutes. Cross-sectional SEM images show that the selenization process results in the formation of a double layer structure of the films.

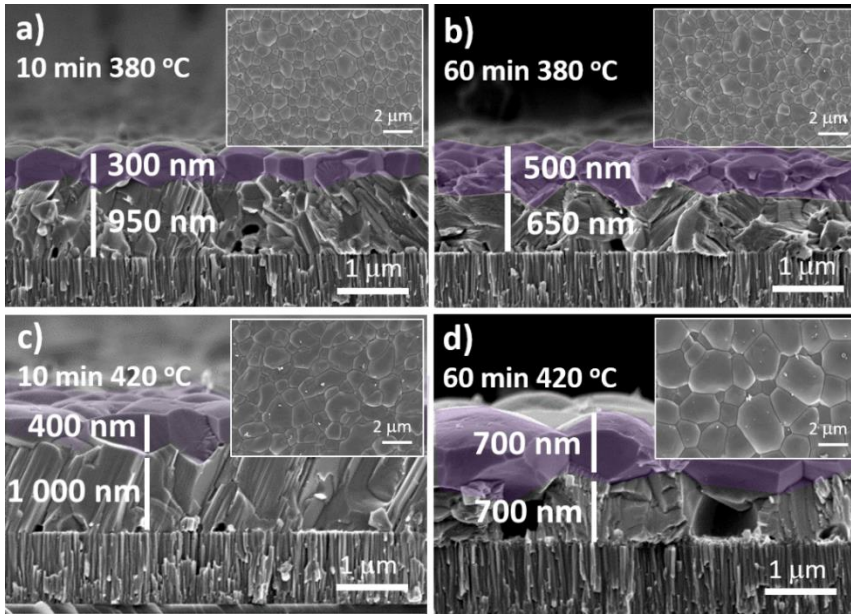
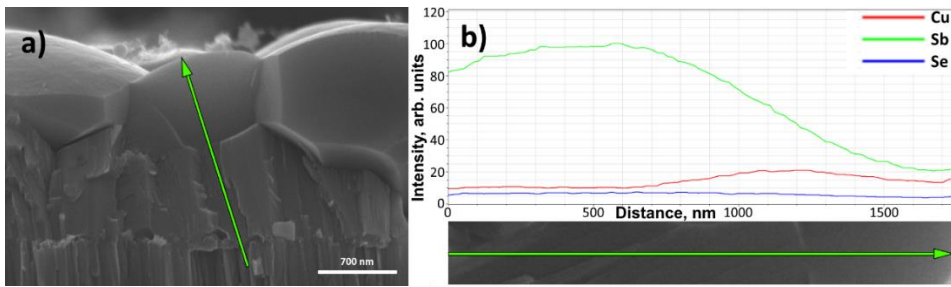


**Figure 23.** SEM images of cross-section and surface of thin films selenized at 380 °C a) for 10 min and b) 60 min, at 420 °C c) for 10 min and d) 60 min showing the formed double-layered structure of the selenized films.

The thickness of the top layer increases from ~300 nm to ~500 nm by increasing the annealing time from 10 to 60 minutes.

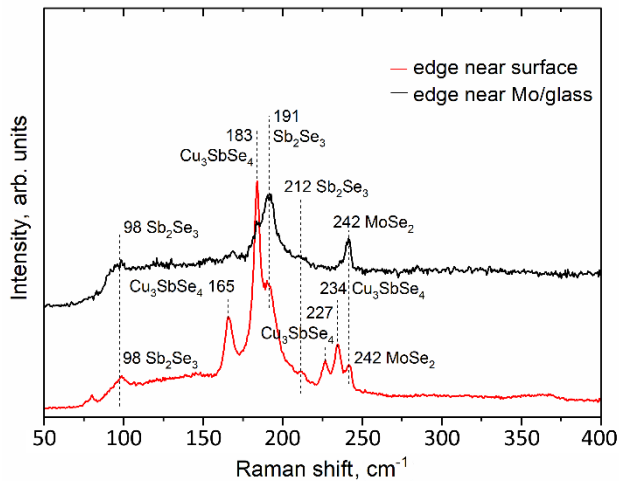
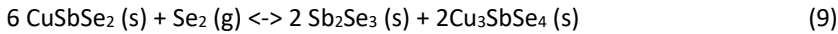
Figure 23c and Figure 23d show the SEM images of cross-section and surface of the films selenized at 420 °C for 10 and 60 minutes, respectively. The crystals in the top layer of the film are growing much larger with increasing the annealing temperature and time. Furthermore, top-view SEM images (inset images in Figure 23d) show the formation of large, sintered crystals after annealing at higher temperatures (420 °C). The thickness of top layer after selenization at 420 °C for 60 minutes is approximately 700 nm. The estimated thickness of the bottom layer is ~700 nm. Unfortunately, the formed thin film also contains pinholes between large crystals exposing the Mo back contact.

After the selenization at 420 °C for 60 minutes, the double-layered films were analyzed by EDX elemental depth profiles across the cross-section of the film as shown in Figure 24. According to the EDX profile, Cu concentration increased from the bottom layer to top layer (marked with a red line in Figure 24(b) and the concentration of Sb decreased in the same direction (marked with a green line in Figure 24(b)). The content of Se was homogeneously distributed over the cross-section of film (marked with a blue line in Figure 24(b)). EDX analysis showed that the surface layer contains Cu 33.8 at% and Sb 12.1 at% ([Cu]/[Sb] ratio is ~2.8) and near the Mo back-contact, the Cu content was 9.7 at% and Sb content was 33.3 at% ([Cu]/[Sb]~0.3). To determine the phase composition of double-layered Cu-Sb-Se films, Raman analysis was performed on the cross-section of samples.



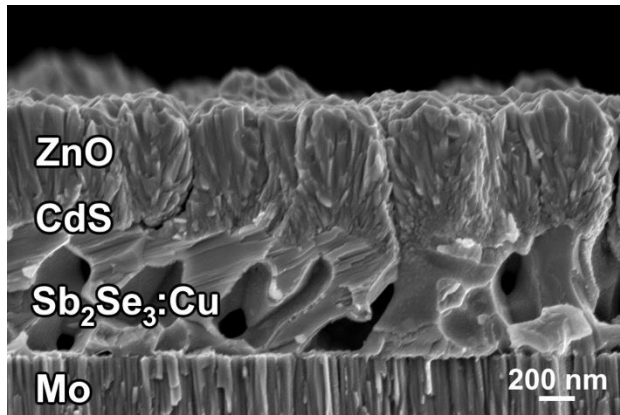
**Figure 24.** a) SEM images of cross-section of selenized  $\text{CuSbSe}_2$  thin film at  $420\text{ }^\circ\text{C}$  for 60 min and b) corresponding EDX profile.

Figure 25 shows the Raman spectra measured from the cross-section of  $\text{CuSbSe}_2$  film selenized at  $420\text{ }^\circ\text{C}$ . Based on the relative intensities of the Raman peaks, it shows that on the back contact side (edge near Mo/SLG) is mainly  $\text{Sb}_2\text{Se}_3$  phase with characteristic Raman peaks at  $98, 191$  and  $212\text{ cm}^{-1}$  [111]. On the front side (near the surface) is mainly  $\text{Cu}_3\text{SbSe}_4$  phase with characteristic Raman peaks at  $165, 183, 227$  and  $234\text{ cm}^{-1}$ , which are in correspondence with the data presented in [116]. Raman peak at  $242\text{ cm}^{-1}$  belongs to  $\text{MoSe}_2$  [117]. XRD analysis confirmed that  $\text{CuSbSe}_2$  films decomposed after selenization at  $380\text{ }^\circ\text{C}$  and  $420\text{ }^\circ\text{C}$ , the new phases appeared according to the formula (9):



**Figure 25.** Raman spectra of  $\text{CuSbSe}_2$  thin film selenized at  $420\text{ }^\circ\text{C}$  for 60 min.

As  $\text{Cu}_3\text{SbSe}_4$  compound detected as the top layer of the selenized films has very small bandgap  $0.29\text{ eV}$  [34], KCN chemical etching was applied before using the selenized thin films as absorber layers in solar cells. KCN etching is typically used to remove Cu-chalcogenide phases [118]. After the etching process, the remaining porous thin film contained mainly  $\text{Sb}_2\text{Se}_3$  phase (Sb 39.6 at%, Se 57.5 at% by EDX) with small amount of Cu (2.9 at% by EDX).



**Figure 26.** SEM image of the cross-section of solar cell with the structure: SLG/Mo/Sb<sub>2</sub>Se<sub>3</sub>:Cu/CdS/i-ZnO/ZnO:Al.

Figure 26 shows the SEM image of cross-section of the prepared solar cell structure glass/Mo/Sb<sub>2</sub>Se<sub>3</sub>:Cu/CdS/i-ZnO/ZnO:Al. Current-voltage characteristic of the device is shown in the Figure 27a. The highest PCE of 3.2% was achieved with the following parameters: the open circuit voltage ( $V_{oc}$ ) of the cell was 373 mV,  $FF = 52.1\%$  and short circuit current density ( $J_{sc}$ ) 16.5 mA/cm<sup>2</sup>. The working area was 3.9 mm<sup>2</sup>.

Figure 27b shows the EQE spectra of the solar cell structure glass/Mo/Sb<sub>2</sub>Se<sub>3</sub>:Cu/CdS/i-ZnO/ZnO:Al. EQE was used to determine the band gap ( $E_g$ ) value of absorber material. The EQE spectra was measured as a function of the incident light wavelength at room temperature in the wavelength range from 350 to 1200 nm. From the linear segment of the low-energy side of the construction  $(EQE)^2$  vs.  $E$  curves, the effective bandgap energy ( $E_g^*$ ) was evaluated. Estimated band gap value was 1.25 eV, which is in good correlation with reported bandgap values for Sb<sub>2</sub>Se<sub>3</sub> [119].

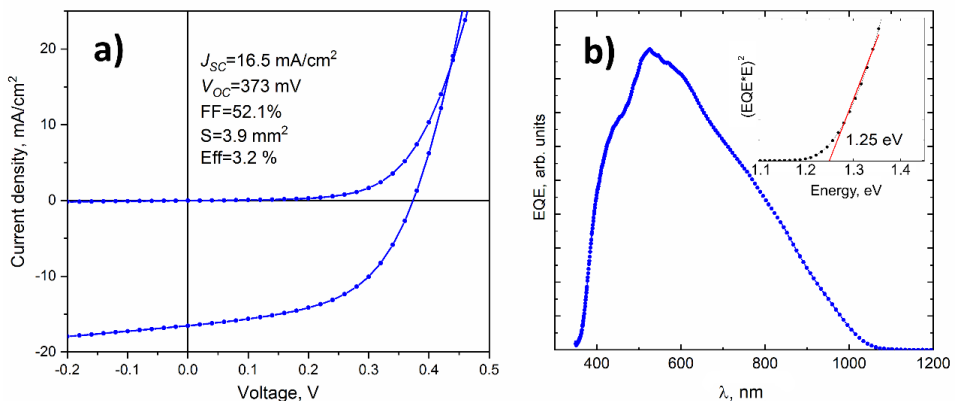


**Figure 27.** a) J-V characteristic and b) EQE of solar cell with the structure: SLG/Mo/Sb<sub>2</sub>Se<sub>3</sub>:Cu/CdS/i-ZnO/ZnO:Al.

## Conclusions

In this thesis, two polycrystalline materials - CuSbSe<sub>2</sub> and Sb<sub>2</sub>Se<sub>3</sub> were successfully prepared. At first, a structural and compositional analysis was performed, followed by a detailed photoluminescence (PL) study. There was no PL studies of these compounds available in the literature at the beginning of this doctoral study and therefore, no information was available about the radiative recombination mechanisms and related defects in CuSbSe<sub>2</sub> and Sb<sub>2</sub>Se<sub>3</sub>.

In addition, CuSbSe<sub>2</sub> thin films were deposited by magnetron co-sputtering method and their morphology, structural properties and elemental and phase composition were investigated. CuSbSe<sub>2</sub> thin films with single phase composition were annealed under selenium atmosphere at different conditions and the changes in the morphology, structural properties and elemental and phase composition of the films depending on the annealing conditions were investigated. Following conclusions can be drawn:

1. According to the compositional analysis by EDX, the bulk composition of synthesized CuSbSe<sub>2</sub> polycrystalline material was Cu-poor and Sb-rich. The uniformity of polycrystalline sample was analyzed by EDX mapping, which confirmed the uniform distribution of all elements. The phase and crystal structure analysis by XRD and Raman spectroscopy confirmed that CuSbSe<sub>2</sub> crystallized in orthorhombic structure.
2. A detailed PL analysis of the synthesized CuSbSe<sub>2</sub> polycrystalline material using various temperatures and laser excitation powers was performed. The results of PL study showed that the low-temperature ( $T = 10$  K) PL spectra of CuSbSe<sub>2</sub> consists of three emission bands: PL1 (1.28 eV), PL2 (1.17 eV), and PL3 (0.90 eV). Based on the peak positions and temperature dependencies of the PL spectra the PL1 band is proposed to result from the band-to-band (BB) recombination and the PL2 band from the band-to acceptor (FB) recombination involving deep acceptor defect with an activation energy of  $165 \pm 6$  meV, which is attributed to Cu<sub>Sb</sub> antisite defect. The latter may act as a strong recombination center in a solar cell limiting the performance of the device. The origin of the PL3 band remains open and is proposed to result either from the deep donor – deep acceptor recombination or result from the Sb<sub>2</sub>Se<sub>3</sub> secondary phase detected in the CuSbSe<sub>2</sub> polycrystalline material.
3. Sb<sub>2</sub>Se<sub>3</sub> polycrystalline sample was prepared by isothermal annealing of the commercial Sb<sub>2</sub>Se<sub>3</sub> powder at 350 °C in Ar atmosphere in the presence of additional Se source. According to the XRD analysis, the material crystallized in orthorhombic structure of Sb<sub>2</sub>Se<sub>3</sub>. According to photoreflectance spectroscopy, the band gap value of the studied Sb<sub>2</sub>Se<sub>3</sub> polycrystals was determined to be  $E_g = 1.182 \pm 0.010$  eV at room temperature.
4. A detailed PL analysis of the prepared Sb<sub>2</sub>Se<sub>3</sub> polycrystalline material using various temperatures and laser excitation powers was performed. The low-temperature PL ( $T = 10$  K) study of Sb<sub>2</sub>Se<sub>3</sub> showed that PL spectra consists of three PL bands: PL1 (1.24 eV), PL2 (1.10 eV), and PL3 (0.94 eV). The temperature dependence of the PL bands positions revealed a slight shift towards higher energies in the case of the PL1 and PL3 bands. PL2 band peak position showed a red-shift larger than the temperature dependence of the band gap. PL1 and PL3 bands were found to originate from the donor-acceptor pair (DAP) recombination. PL1 band is close to the low-temperature band gap of Sb<sub>2</sub>Se<sub>3</sub> 1.32 eV and involves more distant pairs

and shallower defects, while PL3 band involves more close pairs and deeper defects, which again is not favourable for the solar cell performance. The origin of the PL2 band remains open, but is proposed to be related to the recombination at the grain boundaries. To analyze the recombination mechanisms behind the PL bands, also the laser power dependence of the PL spectra was measured at  $T = 10$  K. The power coefficient  $m \sim 0.6$  was found for all three PL bands. The detected  $m$  value, which is smaller than unity, indicates to the radiative recombination of charge carriers localized at defects within the band gap for all three PL bands.

5. Cu-poor  $\text{CuSbSe}_2$  thin films were successfully deposited by magnetron sputtering method at  $350^\circ\text{C}$ . Structural analysis by XRD and Raman spectroscopy revealed that as-deposited films consisted mainly  $\text{CuSbSe}_2$  phase with minor traces of  $\text{Sb}_2\text{Se}_3$ . The influence of post-deposition annealing temperature from  $380$ - $420^\circ\text{C}$  and annealing time from 10 to 60 minutes in selenium atmosphere on the morphology and phase composition of  $\text{CuSbSe}_2$  as absorber layer was studied. Structural analysis by XRD revealed that selenization at selected temperatures led to decomposition of  $\text{CuSbSe}_2$  to  $\text{Cu}_3\text{SbSe}_4$  and  $\text{Sb}_2\text{Se}_3$  phases. Cross-sectional SEM images showed that the selenization process resulted in the formation of a double layer structure of the films. According to the EDX profile and Raman analysis, double-layered Cu-Sb-Se films consisted from mainly  $\text{Sb}_2\text{Se}_3$  phase on the bottom of the layer and  $\text{Cu}_3\text{SbSe}_4$  on top of the layer. As  $\text{Cu}_3\text{SbSe}_4$  compound has very small bandgap  $0.29$  eV, KCN chemical etching was applied before using the selenized thin films as absorber layers in solar cells. Chemical etching with KCN aqueous solution effectively removed  $\text{Cu}_3\text{SbSe}_4$  phase and remained porous  $\text{Sb}_2\text{Se}_3$ :Cu layer was implemented in the device with structure: SLG/Mo/ $\text{Sb}_2\text{Se}_3$ :Cu/CdS/*i*-ZnO/ZnO:Al and the power conversion efficiency of 3.2% was achieved.



## References

- [1] World total Electricity Consumption Data, [Online]. Available: <https://www.iea.org/reports/electricity-information-overview/electricity-consumption>.
- [2] IRENA, [Online]. Available: <https://www.irena.org/>.
- [3] J.F. Weaver, Humans have installed 1 terawatt of solar capacity, generated over 1 petawatt of solar electricity in 2021, *PV Mag.* (2022). Available: <https://pv-magazine-usa.com/2022/03/14/humans-install-1-terawatt-of-solar-capacity-generate-over-1-petawatt-of-solar-electricity-in-2021/>.
- [4] A.-M. Rusen, D. Tokar, Building integrated photovoltaics (BIPV), *Rev. Rom. Ing. Civila/Romanian J. Civ. Eng.* 11 (2020) 423–428. doi:10.37789/rjce.2020.11.4.3.
- [5] J. Kurian, L. Karthi, Building integrated photovoltaics- an overview, *Sustain. Agri, Food Environ. Res.* 10 (2021). doi:10.7770/safer-V10N1-art2495.
- [6] M.A. Green, E.D. Dunlop, J. Hohl-Ebinger, M. Yoshita, N. Kopidakis, K. Bothe, D. Hinken, M. Rauer, X. Hao, Solar cell efficiency tables (Version 60), *Prog. Photovoltaics Res. Appl.* 30 (2022) 687–701. doi:10.1002/pip.3595.
- [7] S. Bhattacharya, S. John, Beyond 30% Conversion Efficiency in Silicon Solar Cells: A Numerical Demonstration, *Sci. Rep.* 9 (2019) 12482. doi:10.1038/s41598-019-48981-w.
- [8] C. Xing, Y. Lei, M. Liu, S. Wu, W. He, Z. Zheng, Environment-friendly Cu-based thin film solar cells: materials, devices and charge carrier dynamics, *Phys. Chem. Chem. Phys.* 23 (2021) 16469–16487. doi:10.1039/D1CP02067F.
- [9] First Solar Achieves Yet Another Cell Conversion Efficiency World Record, Press Release. (2016). Available: <https://investor.firstsolar.com/news/press-release-details/2016/First-Solar-Achieves-Yet-Another-Cell-Conversion-Efficiency-World-Record/default.aspx>.
- [10] M. Nakamura, K. Yamaguchi, Y. Kimoto, Y. Yasaki, T. Kato, H. Sugimoto, Cd-Free Cu(In,Ga)(Se,S)<sub>2</sub> Thin-Film Solar Cell With Record Efficiency of 23.35%, *IEEE J. Photovoltaics.* 9 (2019) 1863–1867. doi:10.1109/JPHOTOV.2019.2937218.
- [11] J.L. Gray, The Physics of the Solar Cell, in: *Handb. Photovolt. Sci. Eng.*, John Wiley & Sons, Ltd, 2010: pp. 82–129. doi:<https://doi.org/10.1002/9780470974704.ch3>.
- [12] L.C. Augustin McEvoy, T. Markvart, *Practical Handbook of Photovoltaics*, Elsevier, 2012. doi:10.1016/C2011-0-05723-X.
- [13] Y. Gong, Q. Zhu, B. Li, S. Wang, B. Duan, L. Lou, C. Xiang, E. Jedlicka, R. Giridharagopal, Y. Zhou, Q. Dai, W. Yan, S. Chen, Q. Meng, H. Xin, Elemental demixing-induced epitaxial kesterite/CdS interface enabling 13%-efficiency kesterite solar cells, *Nat. Energy.* 7 (2022) 966–977. doi:10.1038/s41560-022-01132-4.
- [14] A. Kojima, K. Teshima, Y. Shirai, T. Miyasaka, Organometal Halide Perovskites as Visible-Light Sensitizers for Photovoltaic Cells, *J. Am. Chem. Soc.* 131 (2009) 6050–6051. doi:10.1021/ja809598r.
- [15] H. Min, D.Y. Lee, J. Kim, G. Kim, K.S. Lee, J. Kim, M.J. Paik, Y.K. Kim, K.S. Kim, M.G. Kim, T.J. Shin, S. Il Seok, Perovskite solar cells with atomically coherent interlayers on SnO<sub>2</sub> electrodes, *Nature.* 598 (2021) 444–450. doi:10.1038/s41586-021-03964-8.
- [16] T. Unold, Accelerating research on novel photovoltaic materials, *Faraday Discuss.* (2022). doi:10.1039/D2FD00085G.

- [17] S. Kim, N.-H. Kim, Impurity Phases and Optoelectronic Properties of CuSbSe<sub>2</sub> Thin Films Prepared by Cosputtering Process for Absorber Layer in Solar Cells, Coatings. 10 (2020). doi:10.3390/coatings10121209.
- [18] S. Karup-Møller, The Cu-Sb-Se phase system at temperatures between 350° and 700°C, Neues Jahrb. Für Mineral. - Abhandlungen. 174 (1999) 277–292. doi:10.1127/njma/174/1999/277.
- [19] M. A. Shtykova, M. S. Molokeev, B. A. Zakharov, N. V. Selezneva, A. S. Aleksandrovsky, R. S. Bubnova, D. N. Kamaev, A. A. Gubin, N. N. Habibullayev, A.V. Matigorov, E.V. Boldyreva, O.V. Andreev, Structure and properties of phases in the Cu<sub>2-x</sub>Se-Sb<sub>2</sub>Se<sub>3</sub> system. The Cu<sub>2-x</sub>Se-Sb<sub>2</sub>Se<sub>3</sub> phase diagram, J. Alloys Compd. 906 (2022) 164384. doi:10.1016/j.jallcom.2022.164384.
- [20] Z. Li, X. Liang, G. Li, H. Liu, H. Zhang, J. Guo, J. Chen, K. Shen, X. San, W. Yu, R.E.I. Schropp, Y. Mai, 9.2%-efficient core-shell structured antimony selenide nanorod array solar cells, Nat. Commun. 10 (2019) 125. doi:10.1038/s41467-018-07903-6.
- [21] V. M. Glazov, A. N. Krestovnikov, R. A. Kuliev, Investigation of phase equilibrium and analysis of the nature of intermolecular interaction in systems formed by copper and antimony chalcogenides, Zhurnal Fiz. Khimii Russ. 43 (1969) 3063–3066.
- [22] M.I. Golovei, V.I. Tkachenko, M.Y. Rigan, N.P. Stasyuk, Phase-diagram of the system Cu<sub>2</sub>Se–Sb<sub>2</sub>Se<sub>3</sub> in the region of the existence of the compound CuSbSe<sub>2</sub>, Neorg. Mater. 26 (1990) 786 – 788.
- [23] T. Wada, T. Maeda, Optical properties and electronic structures of CuSbS<sub>2</sub>, CuSbSe<sub>2</sub>, and CuSb(S<sub>1-x</sub>Se<sub>x</sub>)<sub>2</sub> solid solution, Phys. Status Solidi C. 14 (2017) 1600196. doi:https://doi.org/10.1002/pssc.201600196.
- [24] D.-J. Xue, B. Yang, Z.-K. Yuan, G. Wang, X. Liu, Y. Zhou, L. Hu, D. Pan, S. Chen, J. Tang, CuSbSe<sub>2</sub> as a Potential Photovoltaic Absorber Material: Studies from Theory to Experiment, Adv. Energy Mater. 5 (2015) 1501203. doi:https://doi.org/10.1002/aenm.201501203.
- [25] A. Pfitzner, ed., Crystal structure of tricopper tetraselenoantimonate (V), Cu<sub>3</sub>SbSe<sub>4</sub>, Zeitschrift Für Krist. - Cryst. Mater. 209 (1994) 685–685. doi:10.1524/zkri.1994.209.8.685.
- [26] D. Tang, J. Yang, F. Liu, Y. Lai, J. Li, Y. Liu, Growth and characterization of CuSbSe<sub>2</sub> thin films prepared by electrodeposition, Electrochim. Acta. 76 (2012) 480–486. doi:10.1016/j.electacta.2012.05.066.
- [27] D. Colombara, L.M. Peter, K.D. Rogers, J.D. Painter, S. Roncallo, Formation of CuSbS<sub>2</sub> and CuSbSe<sub>2</sub> thin films via chalcogenisation of Sb–Cu metal precursors, Thin Solid Films. 519 (2011) 7438–7443. doi:https://doi.org/10.1016/j.tsf.2011.01.140.
- [28] A.W. Welch, L.L. Baranowski, P. Zawadzki, S. Lany, C.A. Wolden, A. Zakutayev, CuSbSe<sub>2</sub> photovoltaic devices with 3% efficiency, Appl. Phys. Express. 8 (2015) 082301. doi:10.7567/APEX.8.082301.
- [29] M. Kumar, C. Persson, Cu(Sb,Bi)(S,Se)<sub>2</sub> as Indium-free Absorber Material with High Optical Efficiency, Energy Procedia. 44 (2014) 176–183. doi:10.1016/j.egypro.2013.12.025.
- [30] A.W. Welch, P.P. Zawadzki, S. Lany, C.A. Wolden, A. Zakutayev, Self-regulated growth and tunable properties of CuSbS<sub>2</sub> solar absorbers, Sol. Energy Mater. Sol. Cells. 132 (2015) 499–506. doi:https://doi.org/10.1016/j.solmat.2014.09.041.

- [31] E.J. Skoug, D.T. Morelli, Role of Lone-Pair Electrons in Producing Minimum Thermal Conductivity in Nitrogen-Group Chalcogenide Compounds, *Phys. Rev. Lett.* 107 (2011) 235901. doi:10.1103/PhysRevLett.107.235901.
- [32] O. Surucu, M. Isik, M. Terlemezoglu, T. Bektas, N.M. Gasanly, M. Parlak, Temperature effects on optical characteristics of thermally evaporated CuSbSe<sub>2</sub> thin films for solar cell applications, *Opt. Mater.* 133 (2022) 113047. doi:https://doi.org/10.1016/j.optmat.2022.113047.
- [33] D. Do, V. Ozolins, S.D. Mahanti, M.-S. Lee, Y. Zhang, C. Wolverton, Physics of bandgap formation in Cu–Sb–Se based novel thermoelectrics: the role of Sb valency and Cu d levels, *J. Phys. Condens. Matter.* 24 (2012) 415502. doi:10.1088/0953-8984/24/41/415502.
- [34] T.-R. Wei, H. Wang, Z.M. Gibbs, C.-F. Wu, G.J. Snyder, J.-F. Li, Thermoelectric properties of Sn-doped p-type Cu<sub>3</sub>SbSe<sub>4</sub>: a compound with large effective mass and small band gap, *J. Mater. Chem. A.* 2 (2014) 13527–13533. doi:10.1039/C4TA01957A.
- [35] B. Yang, C. Wang, Z. Yuan, S. Chen, Y. He, H. Song, R. Ding, Y. Zhao, J. Tang, Hydrazine solution processed CuSbSe<sub>2</sub>: Temperature dependent phase and crystal orientation evolution, *Sol. Energy Mater. Sol. Cells.* 168 (2017) 112–118. doi:10.1016/j.solmat.2017.04.030.
- [36] A.W. Welch, L.L. Baranowski, H. Peng, H. Hempel, R. Eichberger, T. Unold, S. Lany, C. Wolden, A. Zakutayev, Trade-Offs in Thin Film Solar Cells with Layered Chalcostibite Photovoltaic Absorbers, *Adv. Energy Mater.* 7 (2017) 1601935. doi:https://doi.org/10.1002/aenm.201601935.
- [37] S. Rampino, F. Pattini, M. Bronzoni, M. Mazzer, M. Sidoli, G. Spaggiari, E. Gilioli, CuSbSe<sub>2</sub> thin film solar cells with ~4% conversion efficiency grown by low-temperature pulsed electron deposition, *Sol. Energy Mater. Sol. Cells.* 185 (2018) 86–96. doi:10.1016/j.solmat.2018.05.024.
- [38] L.I. Soliman, A.M. Soad, H. Zayed, S.A. Ghfar, Structural and electrical properties of CuSbTe<sub>2</sub>, CuSbSe<sub>2</sub> and CuSbS<sub>2</sub> chalcogenide thin films, *Fiz. A.* 11 (2002) 139–152.
- [39] L. Yu, R. S. Kokenyesi, D. A. Keszler, A. Zunger, Inverse Design of High Absorption Thin-Film Photovoltaic Materials, *Adv. Energy Mater.* 3 (2013) 43–48. doi:https://doi.org/10.1002/aenm.201200538.
- [40] D. Zhang, J. Yang, Q. Jiang, L. Fu, Y. Xiao, Y. Luo, Z. Zhou, Ternary CuSbSe<sub>2</sub> chalcostibite: facile synthesis, electronic-structure and thermoelectric performance enhancement, *J. Mater. Chem. A.* 4 (2016) 4188–4193. doi:10.1039/C6TA00039H.
- [41] K.J. Tiwari, V. Vinod, A. Subrahmanyam, P. Malar, Growth and characterization of chalcostibite CuSbSe<sub>2</sub> thin films for photovoltaic application, *Appl. Surf. Sci.* 418 (2017) 216–224. doi:10.1016/j.apsusc.2017.01.279.
- [42] D. Li, X. Y. Qin, Thermoelectric properties of CuSbSe<sub>2</sub> and its doped compounds by Ti and Pb at low temperatures from 5 to 310 K, *J. Appl. Phys.* 100 (2006) 023713. doi:10.1063/1.2218592.
- [43] J. Zhou, G.-Q. Bian, Q.-Y. Zhu, Y. Zhang, C.-Y. Li, J. Dai, Solvothermal crystal growth of CuSbQ<sub>2</sub> (Q=S, Se) and the correlation between macroscopic morphology and microscopic structure, *J. Solid State Chem.* 182 (2009) 259–264. doi:10.1016/j.jssc.2008.10.025.

- [44] C. Wang, B. Yang, R. Ding, W. Chen, R. Kondrotas, Y. Zhao, S. Lu, Z. Li, J. Tang, Reactive close-spaced sublimation processed CuSbSe<sub>2</sub> thin films and their photovoltaic application, *APL Mater.* 6 (2018) 084801. doi:10.1063/1.5028415.
- [45] D. Goyal, C.P. Goyal, H. Ikeda, P. Malar, Role of growth temperature in photovoltaic absorber CuSbSe<sub>2</sub> deposition through e-beam evaporation, *Mater. Sci. Semicond. Process.* 108 (2020) 104874. <https://doi.org/10.1016/j.mssp.2019.104874>.
- [46] T. Guo, D. Wang, Y. Yang, X. Xiong, K. Li, G. Zeng, B. Li, M. Ghali, Preparation and characterization of CuSbSe<sub>2</sub> thin films deposited by pulsed laser deposition, *Mater. Sci. Semicond. Process.* 127 (2021) 105716. <https://doi.org/10.1016/j.mssp.2021.105716>.
- [47] C. Metzner, B. Scheffel, Special aspects concerning the electron beam deposition of multi-component alloys, *Surf. Coatings Technol.* 146–147 (2001) 491–497. [https://doi.org/10.1016/S0257-8972\(01\)01460-8](https://doi.org/10.1016/S0257-8972(01)01460-8).
- [48] H.N. Lee, H.M. Christen, M.F. Chisholm, C.M. Rouleau, D.H. Lowndes, Strong polarization enhancement in asymmetric three-component ferroelectric superlattices, *Nature.* 433 (2005) 395–399. doi:10.1038/nature03261.
- [49] D. Goyal, C. P. Goyal, H. Ikeda, C. Gopalakrishnan, P. Malar, Study of CuSbSe<sub>2</sub> thin films grown by pulsed laser deposition from bulk source material, *Mater. Sci. Semicond. Process.* 121 (2021) 105420. doi:<https://doi.org/10.1016/j.mssp.2020.105420>.
- [50] J. L. Shohet, ed., *Encyclopedia of Plasma Technology*, CRC Press, 2016. <https://doi.org/10.1201/9781351204958>.
- [51] J. E. Mahan, *Physical Vapor Deposition of Thin Films*, Wiley-VCH Verlag GmbH & Co. KGaA, 2000.
- [52] H. Yan, R. Xiao, Y. Pei, K. Yang, B. Li, Structural, electrical and optical characteristics of CuSbSe<sub>2</sub> films prepared by pulsed laser deposition and magnetron sputtering processes, *J. Mater. Sci. Mater. Electron.* 31 (2020) 644–651. doi:10.1007/s10854-019-02570-9.
- [53] G. Ghosh, The sb-se (antimony-selenium) system, *J. Phase Equilibria.* 14 (1993) 753–763. doi:10.1007/BF02667889.
- [54] C. Chen, D. C. Bobela, Y. Yang, S. Lu, K. Zeng, C. Ge, B. Yang, L. Gao, Y. Zhao, M. C. Beard, J. Tang, Characterization of basic physical properties of Sb<sub>2</sub>Se<sub>3</sub> and its relevance for photovoltaics, *Front. Optoelectron.* 10 (2017) 18–30. doi:10.1007/s12200-017-0702-z.
- [55] V. L. Deringer, R. P. Stoffel, M. Wuttig, R. Dronskowski, Vibrational properties and bonding nature of Sb<sub>2</sub>Se<sub>3</sub> and their implications for chalcogenide materials, *Chem. Sci.* 6 (2015) 5255–5262. doi:10.1039/C5SC00825E.
- [56] K. Zeng, D.-J. Xue, J. Tang, Antimony selenide thin-film solar cells, *Semicond. Sci. Technol.* 31 (2016) 063001. doi:10.1088/0268-1242/31/6/063001.
- [57] Y. Zhou, M. Leng, Z. Xia, J. Zhong, H. Song, X. Liu, B. Yang, J. Zhang, J. Chen, K. Zhou, J. Han, Y. Cheng, J. Tang, Solution-Processed Antimony Selenide Heterojunction Solar Cells, *Adv. Energy Mater.* 4 (2014) 1301846. doi:<https://doi.org/10.1002/aenm.201301846>.
- [58] M. Birkett, W.M. Linhart, J. Stoner, L. J. Phillips, K. Durose, J. Alaria, J. D. Major, R. Kudrawiec, T. D. Veal, Band gap temperature-dependence of close-space sublimation grown Sb<sub>2</sub>Se<sub>3</sub> by photo-reflectance, *APL Mater.* 6 (2018) 84901. doi:10.1063/1.5027157.

- [59] C. Chen, W. Li, Y. Zhou, C. Chen, M. Luo, X. Liu, K. Zeng, B. Yang, C. Zhang, J. Han, J. Tang, Optical properties of amorphous and polycrystalline  $\text{Sb}_2\text{Se}_3$  thin films prepared by thermal evaporation, *Appl. Phys. Lett.* 107 (2015) 043905. doi:10.1063/1.4927741.
- [60] J. Krustok, R. Kondrotas, R. Nedzinskas, K. Timmo, R. Kaupmees, V. Mikli, M. Grossberg, Identification of Excitons and Biexcitons in  $\text{Sb}_2\text{Se}_3$  under High Photoluminescence Excitation Density, *Adv. Opt. Mater.* 9 (2021) 2100107. doi:https://doi.org/10.1002/adom.202100107.
- [61] S. Siol, P. Schulz, M. Young, K.A. Borup, G. Teeter, A. Zakutayev, Combinatorial In Situ Photoelectron Spectroscopy Investigation of  $\text{Sb}_2\text{Se}_3/\text{ZnS}$  Heterointerfaces, *Adv. Mater. Interfaces.* 3 (2016) 1600755. doi:10.1002/admi.201600755.
- [62] X. Liu, X. Xiao, Y. Yang, D.-J. Xue, D.-B. Li, C. Chen, S. Lu, L. Gao, Y. He, M.C. Beard, G. Wang, S. Chen, J. Tang, Enhanced  $\text{Sb}_2\text{Se}_3$  solar cell performance through theory-guided defect control, *Prog. Photovoltaics Res. Appl.* 25 (2017) 861–870. doi:10.1002/pip.2900.
- [63] Z. Li, H. Zhu, Y. Guo, X. Niu, X. Chen, C. Zhang, W. Zhang, X. Liang, D. Zhou, J. Chen, Y. Mai, Efficiency enhancement of  $\text{Sb}_2\text{Se}_3$  thin-film solar cells by the co-evaporation of Se and  $\text{Sb}_2\text{Se}_3$ , *Appl. Phys. Express.* 9 (2016) 052302. doi:10.7567/APEX.9.052302.
- [64] T. D. C. Hobson, L. J. Phillips, O. S. Hutter, H. Shiel, J. E. N. Swallow, C. N. Savory, P. K. Nayak, S. Mariotti, B. Das, L. Bowen, L. A. H. Jones, T. J. Featherstone, M. J. Smiles, M. A. Farnworth, G. Zoppi, P. K. Thakur, T.-L. Lee, H. J. Snaith, C. Leighton, D. O. Scanlon, V. R. Dhanak, K. Durose, T. D. Veal, J. D. Major, Isotype Heterojunction Solar Cells Using n-Type  $\text{Sb}_2\text{Se}_3$  Thin Films, *Chem. Mater.* 32 (2020) 2621–2630. doi:10.1021/acs.chemmater.0c00223.
- [65] F. Kosek, J. Tulka, L. Štourač, Optical, photoelectric and electric properties of single-crystalline  $\text{Sb}_2\text{Se}_3$ , *Czechoslov. J. Phys.* 28 (1978) 325–330. doi:10.1007/BF01597220.
- [66] M. Huang, P. Xu, D. Han, J. Tang, S. Chen, Complicated and Unconventional Defect Properties of the Quasi-One-Dimensional Photovoltaic Semiconductor  $\text{Sb}_2\text{Se}_3$ , *ACS Appl. Mater. Interfaces.* 11 (2019) 15564–15572. doi:10.1021/acsami.9b01220.
- [67] C. N. Savory, D. O. Scanlon, The complex defect chemistry of antimony selenide, *J. Mater. Chem. A.* 7 (2019) 10739–10744. doi:10.1039/C9TA02022E.
- [68] W. Lian, R. Cao, G. Li, H. Cai, Z. Cai, R. Tang, C. Zhu, S. Yang, T. Chen, Distinctive Deep-Level Defects in Non-Stoichiometric  $\text{Sb}_2\text{Se}_3$  Photovoltaic Materials, *Adv. Sci.* 9 (2022) 2105268. doi:10.1002/advs.202105268.
- [69] H. Guo, Z. Chen, X. Wang, Q. Cang, X. Jia, C. Ma, N. Yuan, J. Ding, Enhancement in the Efficiency of  $\text{Sb}_2\text{Se}_3$  Thin-Film Solar Cells by Increasing Carrier Concentration and Inducing Columnar Growth of the Grains, *Sol. RRL.* 3 (2019) 1800224. doi:10.1002/solr.201800224.
- [70] X. Wen, C. Chen, S. Lu, K. Li, R. Kondrotas, Y. Zhao, W. Chen, L. Gao, C. Wang, J. Zhang, G. Niu, J. Tang, Vapor transport deposition of antimony selenide thin film solar cells with 7.6% efficiency, *Nat. Commun.* 9 (2018) 2179. doi:10.1038/s41467-018-04634-6.
- [71] J. Tao, X. Hu, J. Xue, Y. Wang, G. Weng, S. Chen, Z. Zhu, J. Chu, Investigation of electronic transport mechanisms in  $\text{Sb}_2\text{Se}_3$  thin-film solar cells, *Sol. Energy Mater. Sol. Cells.* 197 (2019) 1–6. doi:10.1016/j.solmat.2019.04.003.

- [72] R. Krautmann, N. Spalatu, R. Gunder, D. Abou-Ras, T. Unold, S. Schorr, M. Krunk, I. Oja Acik, Analysis of grain orientation and defects in  $\text{Sb}_2\text{Se}_3$  solar cells fabricated by close-spaced sublimation, *Sol. Energy*. 225 (2021) 494–500. doi:10.1016/j.solener.2021.07.022.
- [73] X. Hu, J. Tao, G. Weng, J. Jiang, S. Chen, Z. Zhu, J. Chu, Investigation of electrically-active defects in  $\text{Sb}_2\text{Se}_3$  thin-film solar cells with up to 5.91% efficiency via admittance spectroscopy, *Sol. Energy Mater. Sol. Cells*. 186 (2018) 324–329. doi:10.1016/j.solmat.2018.07.004.
- [74] H. Deng, S. Yuan, X. Yang, J. Zhang, J. Khan, Y. Zhao, M. Ishaq, W. Ye, Y.-B. Cheng, H. Song, J. Tang, High-throughput method to deposit continuous composition spread  $\text{Sb}_2(\text{Se}_x\text{S}_{1-x})_3$  thin film for photovoltaic application, *Prog. Photovoltaics Res. Appl.* 26 (2018) 281–290. doi:10.1002/pip.2980.
- [75] T.D.C. Hobson, L.J. Phillips, O.S. Hutter, K. Durose, J.D. Major, Defect properties of  $\text{Sb}_2\text{Se}_3$  thin film solar cells and bulk crystals, *Appl. Phys. Lett.* 116 (2020) 261101. doi:10.1063/5.0012697.
- [76] S. Messina, M.T.S. Nair, P.K. Nair, Antimony Selenide Absorber Thin Films in All-Chemically Deposited Solar Cells, *J. Electrochem. Soc.* 156 (2009) H327. doi:10.1149/1.3089358.
- [77] Y.C. Choi, T.N. Mandal, W.S. Yang, Y.H. Lee, S.H. Im, J.H. Noh, S. Il Seok,  $\text{Sb}_2\text{Se}_3$ -Sensitized Inorganic–Organic Heterojunction Solar Cells Fabricated Using a Single-Source Precursor, *Angew. Chemie Int. Ed.* 53 (2014) 1329–1333. doi:10.1002/anie.201308331.
- [78] T. T. Ngo, S. Chavhan, I. Kosta, O. Miguel, H. J. Grande, R. Tena-Zaera, Electrodeposition of antimony selenide thin films and application in semiconductor sensitized solar cells, *ACS Appl. Mater. Interfaces*. 6 (2014) 2836–2841. doi:10.1021/am405416a.
- [79] X. Liu, J. Chen, M. Luo, M. Leng, Z. Xia, Y. Zhou, S. Qin, D.-J. Xue, L. Lv, H. Huang, D. Niu, J. Tang, Thermal Evaporation and Characterization of  $\text{Sb}_2\text{Se}_3$  Thin Film for Substrate  $\text{Sb}_2\text{Se}_3/\text{CdS}$  Solar Cells, *ACS Appl. Mater. Interfaces*. 6 (2014) 10687–10695. doi:10.1021/am502427s.
- [80] M. Leng, M. Luo, C. Chen, S. Qin, J. Chen, J. Zhong, J. Tang, Selenization of  $\text{Sb}_2\text{Se}_3$  absorber layer: An efficient step to improve device performance of  $\text{CdS}/\text{Sb}_2\text{Se}_3$  solar cells, *Appl. Phys. Lett.* 105 (2014) 083905. doi:10.1063/1.4894170.
- [81] Y. Zhou, L. Wang, S. Chen, S. Qin, X. Liu, J. Chen, D.-J. Xue, M. Luo, Y. Cao, Y. Cheng, E.H. Sargent, J. Tang, Thin-film  $\text{Sb}_2\text{Se}_3$  photovoltaics with oriented one-dimensional ribbons and benign grain boundaries, *Nat. Photonics*. 9 (2015) 409–415. doi:10.1038/nphoton.2015.78.
- [82] R. Kondrotas, J. Zhang, C. Wang, J. Tang, Growth mechanism of  $\text{Sb}_2\text{Se}_3$  thin films for photovoltaic application by vapor transport deposition, *Sol. Energy Mater. Sol. Cells*. 199 (2019) 16–23. doi:10.1016/j.solmat.2019.04.024.
- [83] L. Wang, D.-B. Li, K. Li, C. Chen, H.-X. Deng, L. Gao, Y. Zhao, F. Jiang, L. Li, F. Huang, Y. He, H. Song, G. Niu, J. Tang, Stable 6%-efficient  $\text{Sb}_2\text{Se}_3$  solar cells with a ZnO buffer layer, *Nat. Energy*. 2 (2017) 17046. doi:10.1038/nenergy.2017.46.
- [84] C. Chen, L. Wang, L. Gao, D. Nam, D. Li, K. Li, Y. Zhao, C. Ge, H. Cheong, H. Liu, H. Song, J. Tang, 6.5% Certified Efficiency  $\text{Sb}_2\text{Se}_3$  Solar Cells Using PbS Colloidal Quantum Dot Film as Hole-Transporting Layer, *ACS Energy Lett.* 2 (2017) 2125–2132. doi:10.1021/acsenerylett.7b00648.

- [85] Z. Duan, X. Liang, Y. Feng, H. Ma, B. Liang, Y. Wang, S. Luo, S. Wang, R. E. I. Schropp, Y. Mai, Z. Li, Sb<sub>2</sub>Se<sub>3</sub> Thin-Film Solar Cells Exceeding 10% Power Conversion Efficiency Enabled by Injection Vapor Deposition Technology, *Adv. Mater.* 34 (2022) 2202969. doi:10.1002/adma.202202969.
- [86] O. K. Simya, B. G. Priyadarshini, K. Balachander, A. M. Ashok, Formation of a phase pure kesterite {CZTSe} thin films using multisource hybrid physical vapour deposition, *Mater. Res. Express.* 7 (2020) 16419. doi:10.1088/2053-1591/ab64ee.
- [87] D. Tang, J. Yang, F. Liu, Y. Lai, M. Jia, J. Li, Y. Liu, One-Step Electrodeposition and Annealing of CuSbSe<sub>2</sub> Thin Films, *Electrochem. Solid-State Lett.* 15 (2011) D11–D13. doi:10.1149/2.007202esl.
- [88] K. Abouabassi, L. Atourki, A. Sala, M. Ouafi, L. Boulkaddat, A. Ait Hssi, N. Labchir, K. Bouabid, A. Almaggoussi, E. Gilioli, A. Ihlal, Annealing Effect on One Step Electrodeposited CuSbSe<sub>2</sub> Thin Films, *Coatings* 12 (2022) 75. doi:10.3390/coatings12010075.
- [89] Z. Li, X. Chen, H. Zhu, J. Chen, Y. Guo, C. Zhang, W. Zhang, X. Niu, Y. Mai, Sb<sub>2</sub>Se<sub>3</sub> thin film solar cells in substrate configuration and the back contact selenization, *Sol. Energy Mater. Sol. Cells.* 161 (2017) 190–196. doi:10.1016/j.solmat.2016.11.033.
- [90] R. Tang, Z.-H. Zheng, Z.-H. Su, X.-J. Li, Y.-D. Wei, X.-H. Zhang, Y.-Q. Fu, J.-T. Luo, P. Fan, G.-X. Liang, Highly efficient and stable planar heterojunction solar cell based on sputtered and post-selenized Sb<sub>2</sub>Se<sub>3</sub> thin film, *Nano Energy.* 64 (2019) 103929. doi:https://doi.org/10.1016/j.nanoen.2019.103929.
- [91] G.-X. Liang, Y.-D. Luo, S. Chen, R. Tang, Z.-H. Zheng, X.-J. Li, X.-S. Liu, Y.-K. Liu, Y.-F. Li, X.-Y. Chen, Z.-H. Su, X.-H. Zhang, H.-L. Ma, P. Fan, Sputtered and selenized Sb<sub>2</sub>Se<sub>3</sub> thin-film solar cells with open-circuit voltage exceeding 500 mV, *Nano Energy.* 73 (2020) 104806. doi:10.1016/j.nanoen.2020.104806.
- [92] S. Rijal, Z. Song, D.-B. Li, S. S. Bista, Y. Yan, Optimizing the Selenization of Sb<sub>2</sub>Se<sub>3</sub> Absorbers to Improve the Film Quality and Solar Cell Performances, in: *2021 IEEE 48th Photovolt. Spec. Conf., IEEE, 2021: pp. 1148–1151.* doi:10.1109/PVSC43889.2021.9518895.
- [93] H. B. Bebb, E. W. Williams, Chapter 4 Photoluminescence I: Theory, in: *R. K. Willardson, A. C. Beer (Eds.), Elsevier, 1972: pp. 181–320.* doi:10.1016/S0080-8784(08)62345-5.
- [94] P. Y. Yu, M. Cardona, *Fundamentals of Semiconductors*, Springer Berlin Heidelberg, Berlin, Heidelberg, 2010. doi:10.1007/978-3-642-00710-1.
- [95] F. Williams, Donor—acceptor pairs in semiconductors, *Phys. Status Solidi.* 25 (1968) 493–512. doi:10.1002/pssb.19680250202.
- [96] B. V Korzun, V. R. Sobol, M. Rusu, R. M. Savizky, A. A. Fadzeyeva, I. I. Maroz, A. N. Gavrilenko, V. L. Matukhin, M. C. Lux-Steiner, Preparation and Phase Relations in the CuSbSe<sub>2</sub> – CuInSe<sub>2</sub> System, *MRS Proc.* 1735 (2016) mrsf14-2047233. doi:10.1557/opl.2016.59.
- [97] T. Raadik, J. Krustok, M.V. Yakushev, Photoreflectance study of AgGaTe<sub>2</sub> single crystals, *Phys. B Condens. Matter.* 406 (2011) 418–420. doi:10.1016/j.physb.2010.11.002.
- [98] W. Qiu, L. Wu, X. Ke, J. Yang, W. Zhang, Diverse lattice dynamics in ternary Cu-Sb-Se compounds, *Sci. Rep.* 5 (2015) 13643. doi:10.1038/srep13643.

- [99] J. Baker, R. S. Kumar, D. Sneed, A. Connolly, Y. Zhang, N. Velisavljevic, J. Paladugu, M. Pravica, C. Chen, A. Cornelius, Y. Zhao, Pressure induced structural transitions in  $\text{CuSbS}_2$  and  $\text{CuSbSe}_2$  thermoelectric compounds, *J. Alloys Compd.* 643 (2015) 186–194. doi:10.1016/j.jallcom.2015.04.138.
- [100] X. Ma, Z. Zhang, X. Wang, S. Wang, F. Xu, Y. Qian, Large-scale growth of wire-like  $\text{Sb}_2\text{Se}_3$  microcrystallines via PEG-400 polymer chain-assisted route, *J. Cryst. Growth.* 263 (2004) 491–497. doi:10.1016/j.jcrysgro.2003.11.004.
- [101] J. Krustok, H. Collan, M. Yakushev, K. Hjelt, The Role of Spatial Potential Fluctuations in the Shape of the {PL} Bands of Multinary Semiconductor Compounds, *Phys. Scr.* T79 (1999) 179. doi:10.1238/physica.topical.079a00179.
- [102] A.P. Levanyuk, V. V Osipov, Edge luminescence of direct-gap semiconductors, *Sov. Phys. Uspekhi.* 24 (1981) 187–215. doi:10.1070/pu1981v024n03abeh004770.
- [103] M. Grossberg, T. Raadik, J. Krustok, M. Kauk-Kuusik, K. Timmo, R. Kaupmees, V. Mikli, A. Mere, Optical and structural properties of orthorhombic and tetragonal polymorphs of  $\text{Cu}_2\text{CdGeSe}_4$ , *Thin Solid Films.* 666 (2018) 44–47. doi:10.1016/j.tsf.2018.09.031.
- [104] M. Grossberg, K. Timmo, T. Raadik, E. Kärber, V. Mikli, J. Krustok, Study of structural and optoelectronic properties of  $\text{Cu}_2\text{Zn}(\text{Sn}_{1-x}\text{Ge}_x)\text{Se}_4$  ( $x = 0$  to 1) alloy compounds, *Thin Solid Films.* 582 (2015) 176–179. doi:10.1016/j.tsf.2014.10.055.
- [105] T. Schmidt, K. Lischka, W. Zulehner, Excitation-power dependence of the near-band-edge photoluminescence of semiconductors, *Phys. Rev. B.* 45 (1992) 8989–8994. doi:10.1103/PhysRevB.45.8989.
- [106] J. Krustok, H. Collan, K. Hjelt, Does the low-temperature Arrhenius plot of the photoluminescence intensity in CdTe point towards an erroneous activation energy?, *J. Appl. Phys.* 81 (1997) 1442–1445. doi:10.1063/1.363903.
- [107] J. Krustok, T. Raadik, M. Grossberg, M. Kauk-Kuusik, V. Trifiletti, S. Binetti, Photoluminescence study of deep donor- deep acceptor pairs in  $\text{Cu}_2\text{ZnSnS}_4$ , *Mater. Sci. Semicond. Process.* 80 (2018) 52–55. doi:10.1016/j.mssp.2018.02.025.
- [108] J. Krustok, J.H. Schön, H. Collan, M. Yakushev, J. Mädasson, E. Bucher, Origin of the deep center photoluminescence in  $\text{CuGaSe}_2$  and  $\text{CuInS}_2$  crystals, *J. Appl. Phys.* 86 (1999) 364–369. doi:10.1063/1.370739.
- [109] F. Willian de Souza Lucas, H. Peng, S. Johnston, P. C. Dippo, S. Lany, L. H. Mascaro, A. Zakutayev, Characterization of defects in copper antimony disulfide, *J. Mater. Chem. A.* 5 (2017) 21986–21993. doi:10.1039/C7TA07012H.
- [110] L. J. Phillips, C. N. Savory, O. S. Hutter, P. J. Yates, H. Shiel, S. Mariotti, L. Bowen, M. Birkett, K. Durose, D. O. Scanlon, J. D. Major, Current Enhancement via a  $\text{TiO}_2$  Window Layer for CSS  $\text{Sb}_2\text{Se}_3$  Solar Cells: Performance Limits and High  $V_{oc}$ , *IEEE J. Photovoltaics.* 9 (2019) 544–551. doi:10.1109/JPHOTOV.2018.2885836.
- [111] A. Shongalova, M. R. Correia, B. Vermang, J. M. V. Cunha, P. M. P. Salomé, P. A. Fernandes, On the identification of  $\text{Sb}_2\text{Se}_3$  using Raman scattering, *MRS Commun.* 8 (2018) 865–870. doi:10.1557/mrc.2018.94.
- [112] D. E. Aspnes, Modulation spectroscopy/electric field effects on the dielectric function of semiconductors, in: M. Balkanski (Ed.), *Handb. Semicond.*, North-Holland, Amsterdam, 1980: pp. 109–154.



- [113] J. Krustok, H. Collan, K. Hjelt, J. Mädasson, V. Valdna, Photoluminescence from deep acceptor-deep donor complexes in CdTe, *J. Lumin.* 72–74 (1997) 103–105. doi:10.1016/S0022-2313(97)00061-6.
- [114] J. Krustok, J. Raudoja, J.-H. Schön, M. Yakushev, H. Collan, The role of deep donor–deep acceptor complexes in CIS-related compounds, *Thin Solid Films.* 361–362 (2000) 406–410. doi:https://doi.org/10.1016/S0040-6090(99)00756-7.
- [115] J. Krustok, J. Mädasson, J. Hiie, Photoluminescence Properties of Z-Bands in CdTe, *Phys. Status Solidi.* 165 (1998) 517–525. doi:10.1002/(SICI)1521-396X(199802)165:2<517::AID-PSSA517>3.0.CO;2-O.
- [116] P. Martínez-Ortíz, S. Lugo-Loredo, J. Campos-Álvarez, Y. Peña-Méndez, J. A. Aguilar-Martínez, Growth and characterization of Cu<sub>3</sub>SbSe<sub>4</sub> thin films through thermally diffusing Sb<sub>2</sub>Se<sub>3</sub> – CuSe by chemical bath deposition (CBD), *Mater. Res. Bull.* 102 (2018) 418–423. https://doi.org/10.1016/j.materresbull.2018.02.049.
- [117] H. Zeng, G.-B. Liu, J. Dai, Y. Yan, B. Zhu, R. He, L. Xie, S. Xu, X. Chen, W. Yao, X. Cui, Optical signature of symmetry variations and spin-valley coupling in atomically thin tungsten dichalcogenides, *Sci. Rep.* 3 (2013) 1608. doi:10.1038/srep01608.
- [118] A. H. Pinto, S. W. Shin, E. S. Aydil, R. L. Penn, Selective removal of Cu<sub>2-x</sub>(S,Se) phases from Cu<sub>2</sub>ZnSn(S,Se)<sub>4</sub> thin films, *Green Chem.* 18 (2016) 5814–5821. doi:10.1039/C6GC01287F.
- [119] S. Polivtseva, J. O. Adegite, J. Kois, D. Mamedov, S. Z. Karazhanov, J. Maricheva, O. Volobujeva, A Novel Thermochemical Metal Halide Treatment for High-Performance Sb<sub>2</sub>Se<sub>3</sub> Photocathodes, *Nanomaterials.* 11 (2020) 52. doi:10.3390/nano11010052.

## Acknowledgements

I acknowledge my supervisors Prof. Maarja Grossberg-Kuusik and Dr. Marit Kauk-Kuusik for their contribution, guidance and motivation.

I appreciate the collaborative input of past and present members of the Laboratory of Optoelectronic Materials and Laboratory of Photovoltaic Materials from Department of Materials and Environmental Technology at Tallinn University of Technology, and the co-authors from other institutions. I am grateful to Dr. Valdek Mikli, Dr. Olga Volobujeva from the Laboratory of Photovoltaic Materials at Tallinn University of Technology for SEM and EDX measurements. I am grateful to Dr. Maris Pilvet from the Laboratory of Photovoltaic Materials at Tallinn University of Technology for window layer deposition.

This work was supported by institutional research funding IUT19-28 of the Estonian Ministry of Education and Research, by the European Regional Development Fund, Project TK141, by the Estonian Research Council grant PRG1023 and by ASTRA “TUT Institutional Development Programme for 2016-2022” Graduate School of Functional Materials and Technologies (2014-2020.4.01.16-0032).

Finally, I offer my sincerest gratitude to my family whose support throughout the progression of this thesis was paramount.

This thesis is dedicated to my mom Svetlana Penežko.

## Abstract

### Properties of $\text{CuSbSe}_2$ and $\text{Sb}_2\text{Se}_3$ Absorber Materials for Solar Cell Applications

The development of efficient photovoltaic (PV) materials composed of nontoxic and earth abundant elements is of utmost importance to meet the increasing demand for electricity production. Currently, crystalline silicon comprises more than 95% of the total revenue of the photovoltaic electricity market. The thin film PV market is dominated by relatively high-efficiency CdTe and  $\text{Cu}(\text{In,Ga})\text{Se}_2$ -based solar cells. The most significant issue facing CdTe cells is concern about the high toxicity of cadmium and the biggest obstacle to the widespread use of CIGS is the relative scarcity of indium, which leads to high material costs. Therefore, alternative thin film PV technologies are being developed. Recently, significant efforts have been made to better and more deeply understand the structural, electrical, and optical properties of binary and ternary Sb-chalcogenide semiconductors due to their potential applications in photovoltaics.

The family of ternary Cu-Sb-Se includes different compounds, among which the ternary chalcogenide  $\text{CuSbSe}_2$  has great potential for single junction solar cell having a layered orthorhombic structure, a p-type conductivity with the suitable bandgap in the range from 1.04 to 1.2 eV, and a very high optical absorption coefficient of  $\sim 10^5 \text{ cm}^{-1}$ . The electrical and optoelectronic properties of semiconductor materials are highly dependent on the chemical composition and defect structure. Photoluminescence spectroscopy (PL) is one of the most sensitive methods for studying defects and photoexcited carrier recombination mechanisms in semiconductors. Unfortunately, at the beginning of this thesis, there was no information about detailed PL analysis of  $\text{CuSbSe}_2$ . Therefore, the first aim of this thesis was to synthesize single phase  $\text{CuSbSe}_2$  polycrystalline material by the melting method and to study the defect structure and related recombination mechanisms by temperature and laser power dependent PL.  $\text{CuSbSe}_2$  polycrystalline material with uniform composition was synthesized from high purity Cu,  $\text{Sb}_2\text{Se}_3$ , and Se precursors at  $900^\circ\text{C}$  by the molten phase reaction method. According to the compositional analysis by energy dispersive X-ray spectroscopy (EDX), the bulk composition of the synthesized  $\text{CuSbSe}_2$  polycrystalline material was Cu-poor and Sb-rich. The phase and crystal structure analysis by X-ray diffraction (XRD) and Raman spectroscopy confirmed that  $\text{CuSbSe}_2$  crystallized in orthorhombic structure.

The results of PL study, which was the first one in the literature, showed that the low-temperature ( $T = 10 \text{ K}$ ) PL spectra of  $\text{CuSbSe}_2$  consists of three emission bands: PL1 (1.28 eV), PL2 (1.17 eV), and PL3 (0.90 eV). Based on the peak positions and temperature dependencies of the PL spectra the PL1 band is proposed to result from the band-to-band (BB) recombination and the PL2 band from the band-to-acceptor (FB) recombination involving deep acceptor defect with an activation energy of  $165 \pm 6 \text{ meV}$ , which is attributed to  $\text{Cu}_{\text{Sb}}$  antisite defect. The latter may act as a strong recombination center in a solar cell limiting the performance of the device and should therefore be avoided. The origin of the PL3 band remained open.

Antimony selenide ( $\text{Sb}_2\text{Se}_3$ ) is also potential absorber material for environment-friendly and cost-efficient photovoltaics that have shown considerable progress in recent years, reaching 10.12% of power conversion efficiency for  $\text{Sb}_2\text{Se}_3$ -based solar cells. However, the bulk defect states in  $\text{Sb}_2\text{Se}_3$  have become one of the major obstacles to further efficiency improvement. Therefore, to obtain the missing information about defect

structure and related recombination mechanisms in polycrystalline  $\text{Sb}_2\text{Se}_3$ , the photoluminescence study was performed. Commercially available  $\text{Sb}_2\text{Se}_3$  powder was isothermally annealed in Se/Ar atmosphere at  $350^\circ\text{C}$ . According to the XRD analysis, the material crystallized in orthorhombic structure of  $\text{Sb}_2\text{Se}_3$ . According to photoreflectance spectroscopy, the band gap value of the studied  $\text{Sb}_2\text{Se}_3$  polycrystals was determined to be  $E_g = 1.182 \pm 0.010$  eV at room temperature.

For the first time, a detailed PL analysis of the prepared  $\text{Sb}_2\text{Se}_3$  polycrystalline material using various temperatures and laser excitation powers was performed. The low-temperature PL ( $T = 10$  K) study of  $\text{Sb}_2\text{Se}_3$  showed that PL spectra consists of three PL bands: PL1 (1.24 eV), PL2 (1.10 eV), and PL3 (0.94 eV). The temperature dependence of the PL bands positions revealed a slight shift (in the order of few meV) towards higher energies in the case of the PL1 and PL3 bands. PL2 band peak position showed a red-shift larger than the temperature dependence of the band gap. PL1 and PL3 bands were found to originate from the donor-acceptor pair (DAP) recombination. PL1 band was close to the low-temperature band gap of  $\text{Sb}_2\text{Se}_3$  1.32 eV and involved more distant pairs and shallower defects, while PL3 band involved more close pairs and deeper defects, which again is not favourable for the solar cell performance. The origin of the PL2 band remains open, but is proposed be related to the recombination at the grain boundaries. To analyze the recombination mechanisms behind the PL bands, also the laser power dependence of the PL spectra was measured at  $T = 10$  K. The detected power coefficient  $m$  values were smaller than unity, which indicated to the radiative recombination of charge carriers localized at defects within the band gap for all three PL bands. Similarly to  $\text{CuSbSe}_2$ , the detected deep defects should be avoided if the material is to be used as an absorber in PV.

The last part of the thesis is dedicated to the study of  $\text{CuSbSe}_2$  thin films deposited by magnetron co-sputtering method from  $\text{Cu}_2\text{Se}$  and  $\text{Sb}_2\text{Se}_3$  targets. The sputtering parameters for homogeneous  $\text{CuSbSe}_2$  thin film deposition was found to be following: a substrate temperature of  $350^\circ\text{C}$ , a sputtering power of 27 W for  $\text{Cu}_2\text{Se}$  and 88 W for  $\text{Sb}_2\text{Se}_3$ .  $\text{CuSbSe}_2$  thin films were subsequently annealed under selenium pressure 1 Torr to improve the properties of as-deposited absorber material. The annealing temperature and annealing time were varied in the range from  $380^\circ\text{C}$  to  $420^\circ\text{C}$  and from 10 to 60 minutes, respectively.

According to EDX analysis, the as-deposited  $\text{CuSbSe}_2$  thin films had Cu-poor composition. XRD and Raman analysis showed that as-deposited films contained mainly  $\text{CuSbSe}_2$  phase. SEM images showed that as-deposited single-layered  $\text{CuSbSe}_2$  films changed to double layered structure after the selenization. The thickness of the top layer increased from 300 nm to 500 nm by increasing the selenization time from 10 to 60 minutes at  $380^\circ\text{C}$ . The top layer thickness increased even more by increasing the temperature to  $420^\circ\text{C}$  for 60 minutes. After selenization, the double-layer structure contained  $\text{Cu}_3\text{SbSe}_4$  phase as top layer and  $\text{Sb}_2\text{Se}_3$  phase as bottom layer.  $\text{Cu}_3\text{SbSe}_4$  phase was removed effectively by chemical etching with 10% KCN alkaline solution. The remained  $\text{Sb}_2\text{Se}_3:\text{Cu}$  layer was implemented into the solar cell structure: SLG/Mo/ $\text{Sb}_2\text{Se}_3:\text{Cu}$ /CdS/*i*-ZnO/ZnO:Al. Complete device was characterized by current-voltage and external quantum efficiency (EQE) measurements. EQE curves were used to estimate the bandgap energy value of absorber layer ( $E_g=1.25$  eV). The highest efficiency of 3.2% with open circuit voltage of 373 mV, fill factor 52.1% and short circuit current density  $16.5 \text{ mA/cm}^2$  was achieved.

In summary, first detailed PL studies of  $\text{CuSbSe}_2$  and  $\text{Sb}_2\text{Se}_3$  presented in this thesis filled some knowledge gaps about the defects and photoexcited carrier recombination mechanisms in these materials, but some PL bands detected in these experiments still need further studies. This study also demonstrated  $\text{CuSbSe}_2$  thin films with good morphology and crystallinity deposited by co-sputtering method. During the post-annealing process, the  $\text{CuSbSe}_2$  films decomposed and formed a double-layer structure, which were not applicable as absorber material in solar cells. Chemical etching treatment removed undesired phases, giving the opportunity to make  $\text{Sb}_2\text{Se}_3:\text{Cu}$ -based a solar cell with efficiency 3.2%, demonstrating alternative approach for the preparation of doped  $\text{Sb}_2\text{Se}_3$  based thin film PV devices.

## Lühikokkuvõte

### Päikeseplatari absorbermaterjalide $\text{CuSbSe}_2$ ja $\text{Sb}_2\text{Se}_3$ omaduste uurimine

Päikeseenergeetikas (PV) kasutatavate keskkonnasõbralike ja maapõues laialt levinud elementidest koosnevate materjalide uurimine ja arendamine on ülimalt oluline, et rahuldada kasvavat nõudlust elektrienergia järele. Praegu moodustavad kristallilise räni baasil päikesepaneelid enam kui 95% päikeseelektri tootmisvõimusest. Õhukesekilelistest tehnoloogiatest domineerivad turul suhteliselt kõrge kasuteguriga CdTe ja  $\text{Cu(In,Ga)Se}_2$ -baasil päikesepaneelid. CdTe päikeseelementide suurimaks probleemiks on kaadmiumi toksilisus ja CIGS-i laialdast kasutamist piirab indiumi kättesaadavus, mis tingib kõrge materjalikulud. Seetõttu uuritakse ja arendatakse järjepidevalt alternatiivseid materjale ja tehnoloogiaid õhukesekileliste PV rakendusteks. Viimastel aastatel on enam tähelepanu saanud uued kahe- ja kolmekomponentsed Sb-kalkogeniididel põhinevad pooljuhtmaterjalid, millede struktuursed, elektrilised ja optilised omadused on paljulubavad päikeseplatari absorbermaterjalide rakendusteks.

Cu-Sb-Se perekonda kuuluvad erinevad ühendid, mille hulgas on kolmekomponentsel kalkogeniidil  $\text{CuSbSe}_2$  suur potentsiaal absorbermaterjalina ühesiirdelises päikeseelemendis.  $\text{CuSbSe}_2$ -l on kihiline ortorombiline struktuur, *p*-tüüpi juhtivus, sobiv keelutsoon vahemikus 1,04- 1,2 eV ja kõrge valguse neeldumiskoeffitsent  $\sim 10^5 \text{ cm}^{-1}$ .

Pooljuhtmaterjalide elektrilised ja optoelektronsed omadused sõltuvad suuresti keemilisest koostisest ja defektstruktuurist. Fotoluminestsents spektroskoopia (PL) on üks tundlikumaid meetodeid defektide ja kiirguslike rekombinatsiooniprotsesside uurimiseks pooljuhtmaterjalides. Käesoleva doktoritöö alguses ei olnud kirjanduses teavet  $\text{CuSbSe}_2$  üksikasjaliku PL analüüsi kohta. Siit tulenes ka käesoleva doktoritöö esimene eesmärk sünteesida ühefaasiline  $\text{CuSbSe}_2$  polükristalne materjal sulatusmeetodil ning uurida selle defektstruktuuri ja rekombinatsioonimehhanisme PL abil. Ühtlase koostisega  $\text{CuSbSe}_2$  polükristalne materjal sünteesiti kõrge puhtusega Cu,  $\text{Sb}_2\text{Se}_3$  ja Se lähteainetest 900 °C juures. Koostise analüüs näitas, et sünteesitud  $\text{CuSbSe}_2$  oli vasevaese ja antimonirikka koostisega. Struktuuriuuringud näitasid, et  $\text{CuSbSe}_2$  kristalliseerus ortorombilises kristallstruktuuris.

Esmakordselt teostatud madaltemperatuurse ( $T = 10 \text{ K}$ ) PL analüüsi tulemused näitasid, et  $\text{CuSbSe}_2$  PL spekter koosnes kolmest kiirgusribast: PL1 (1,28 eV), PL2 (1,17 eV) ja PL3 (0,90 eV). PL ribade asukohtade ja spektrite temperatuurisõltuvuste põhjal leiti, et PL1 riba pärineb tsoon-tsoon (BB) rekombinatsioonist ja PL2 riba tsoon-aktseptor (FB) rekombinatsioonist, mis on seotud  $\text{Cu}_{\text{Sb}}$  sügava aktseptordefektga, mille aktivatsioonienegiaks määrati  $165 \pm 6 \text{ meV}$ . Viimane võib toimida tugeva rekombinatsioonikanalina, mis piirab päikeseelemendi efektiivsust ja mille teket peaks seetõttu ära hoidma. PL3 riba päritolu jäi esialgu lahtiseks ja vajab lisauuringuid.

$\text{Sb}_2\text{Se}_3$  on samuti potentsiaalne absorbermaterjal keskkonnasõbralike ja kulutõhusate päikesepaneelide jaoks.  $\text{Sb}_2\text{Se}_3$ -baseeruvate päikeseelementide kasutegur on viimastel aastatel näidanud märkimisväärselt kiiret kasvu, saavutades käesoleval aastal 10,12%.  $\text{Sb}_2\text{Se}_3$ -s esinevad defektitasemed ja nende kaudu toimuvad rekombinatsioonilised kaod on üheks peamiseks takistuseks kõrgemate kasutegurite saavutamisel.  $\text{Sb}_2\text{Se}_3$  defektstruktuuri ja sellega seotud rekombinatsiooniprotsesse uuriti käesolevas töös samuti fotoluminestsents spektroskoopia abil. Struktuurianalüüs näitas, et eelnevalt 350°C juures Ar/Se aururõhus lõõmutatud  $\text{Sb}_2\text{Se}_3$  polükristalne pulber kristalliseerus

ortorombilises struktuuris. Fotopeegelduse spektroskoopia abil määrati uuritud  $\text{Sb}_2\text{Se}_3$  polükristallide keelutsooniks  $E_g = 1,182 \pm 0,010$  eV toatemperatuuril.

Polükristalse  $\text{Sb}_2\text{Se}_3$  jällegi esmakordselt teostatud detailse PL analüüsi jaoks kasutati erinevaid temperatuure ja laseri ergastusvõimsuseid.  $\text{Sb}_2\text{Se}_3$  madaltemperatuurne PL ( $T = 10$  K) analüüs näitas, et PL spekter koosnes kolmest PL ribast: PL1 (1,24 eV), PL2 (1,10 eV) ja PL3 (0,94 eV). PL piikide asukohtade temperatuurisõltuvus näitas PL1 ja PL3 piikide väikest nihet (suurusjärgus mõni meV) kõrgemate energiatega suunas. PL2 riba maksimum näitas punanihet, mis on suurem kui keelutsooni temperatuurisõltuvus. Leiti, et PL1 ja PL3 kiirgusribad on põhjustatud doonor-aktseptor paari (DAP) rekombinatsioonist. PL1 riba asus  $\text{Sb}_2\text{Se}_3$  madaltemperatuurse keelutsooni (1,32 eV) lähedal ning hõlmas kaugemaid paare ja madalamaid defekte, samas kui PL3 riba hõlmas lähemaid paare ja sügavamaid defekte, mis jällegi ei ole päikeseelemendi kõrgete väljundparameetrite saavutamiseks kasulik. PL2 piigi täpne põhjus jäi lahtiseks, kuid seda võib seostada kristallide piirpinnal toimuva rekombinatsiooniga. Kiirguslike rekombinatsiooni-mehhanismide analüüsiks kasutati ka madaltemperatuurset ( $T=10$ K) PL spektrite laservõimsusest sõltuvust, mille tulemusel leiti võimsuskoeffitsiendi  $m$  väärtused, mis olid väiksemad kui 1. See viitas, et kõigi kolme PL riba puhul on tegemist laengukandjate kiirgusliku rekombinatsiooniga, milles osalevad keelutsoonis asuvatel defektitasemetel lokaliseeritud laengukandjad. Leitud sügavate defektide teket tuleks ära hoida, kui materjali on plaanis kasutada absorberina päikeseelemendis.

Doktoritöö kolmandas osas uuriti  $\text{CuSbSe}_2$  õhukeste kilede sadestamist  $\text{Cu}_2\text{Se}$  ja  $\text{Sb}_2\text{Se}_3$  märkilaudadest magnetron-koospihustamise meetodil. Leiti, et homogeensete  $\text{CuSbSe}_2$  kilede sadestusparameetrid on järgmised: aluse temperatuur  $350^\circ\text{C}$ ,  $\text{Cu}_2\text{Se}$  ja  $\text{Sb}_2\text{Se}_3$  pihustusvõimsused vastavalt 27 W ja 88 W. Seejärel lõõmutati  $\text{CuSbSe}_2$  kilesid Ar/Se atmosfääris, et parandada absorbermaterjali omadusi. Lõõmutamistemperatuuri ja -aega varieeriti vastavalt vahemikus  $380^\circ\text{C}$  kuni  $420^\circ\text{C}$  ja 10 kuni 60 minutit.

Koostise ja struktuuri analüüsid näitas, et sadestatud  $\text{CuSbSe}_2$  kiled olid Cu-vaese koostisega ja sisaldasid peamiselt  $\text{CuSbSe}_2$  faasi. SEM pildid näitasid, et  $\text{CuSbSe}_2$  kiled lagunesid peale lõõmutusprotsessi kahekihiliseks kileks. Pealmise kihi paksus suurenes 300 nm-lt 500 nm-ni lõõmutusaja pikendamisega 10 minutilt 60 minutile  $380^\circ\text{C}$  juures. Pealmise kihi paksus suurenes veelgi, tõstes temperatuuri  $420^\circ\text{C}$  -ni. Struktuuri analüüs näitas, et kile ülemine kiht koosnes  $\text{Cu}_3\text{SbSe}_4$  faasist ja alumine kiht  $\text{Sb}_2\text{Se}_3$  faasist.  $\text{Cu}_3\text{SbSe}_4$  kiht eemaldati tõhusalt keemilisel söövitamisel 10% KCN leeliselise lahusega. Säilinud  $\text{Sb}_2\text{Se}_3$ :Cu kihti kasutati absorbermaterjalina järgnevas päikeseelemendi struktuuris: SLG/Mo/ $\text{Sb}_2\text{Se}_3$ :Cu/CdS/i-ZnO/ZnO:Al. Päikeseelemendi väljund-parameetrite iseloomustamiseks kasutati voolu-pinge analüüsi. Kvantefektiivsuse analüüsi kasutati absorbermaterjali keelutsooni hindamiseks ( $E_g=1,25$  eV). Suurim  $\text{Sb}_2\text{Se}_3$ :Cu baasil valmistatud päikeseelemendi kasutegur oli 3,2% väljundparameetritega:  $V_{oc}=373$  mV,  $FF=52,1\%$  ja  $J_{sc}=16,5$  mA/cm<sup>2</sup>.

Kokkuvõtlikult võib öelda, et käesolev doktoritöö täitis mõned teadmiste lüngad  $\text{CuSbSe}_2$  ja  $\text{Sb}_2\text{Se}_3$  esinevate defektide ja kiirguslike rekombinatsiooniprotsesside kohta, mida uuriti esmakordselt kasutades fotoluminestsents spektroskoopiat. Mõned uuringutes leitud PL ribad aga vajavad täiendavaid uuringuid. Doktoritöö raames õnnestus sadestada hea morfoloogia ja kristallilisusega  $\text{CuSbSe}_2$  õhukesed kiled magnetron-koospihustamise meetodil. Järellõõmutuse käigus  $\text{CuSbSe}_2$  kiled lagunesid kahekihiliseks kileks, mis ei sobinud päikeseelemendis kasutamiseks. Ebasobivad faasid eemaldati tõhusalt keemilisel söövitamisel ja saadud  $\text{Sb}_2\text{Se}_3$ :Cu absorbermaterjal võimaldas valmistada päikeseelemendid efektiivsusega 3.2%. Sellega pakuti välja alternatiivne meetod legeritud  $\text{Sb}_2\text{Se}_3$  baasil õhukesekiliste päikeseelementide valmistamiseks.

## Appendix

### Publication I

A. Penezko, M. Kauk-Kuusik, O. Volobujeva, R. Traksmäa, and M. Grossberg, Observation of photoluminescence edge emission in  $\text{CuSbSe}_2$  absorber material for photovoltaic applications, *Appl. Phys. Lett.* 115, 092101, 2019.





# Observation of photoluminescence edge emission in CuSbSe<sub>2</sub> absorber material for photovoltaic applications

Cite as: Appl. Phys. Lett. **115**, 092101 (2019); doi: 10.1063/1.5114893

Submitted: 12 June 2019 · Accepted: 9 August 2019 ·

Published Online: 26 August 2019



View Online



Export Citation



CrossMark

A. Penezko,<sup>1,a)</sup>  M. Kauk-Kuusik,<sup>1</sup>  O. Volobujeva,<sup>1</sup>  R. Traksmaa,<sup>2</sup> and M. Grossberg<sup>1</sup> 

## AFFILIATIONS

<sup>1</sup>Department of Materials and Environmental Technology, Tallinn University of Technology, Ehitajate Tee 5, 19086 Tallinn, Estonia

<sup>2</sup>Department of Mechanical and Industrial Engineering, Tallinn University of Technology, Ehitajate Tee 5, 19086 Tallinn, Estonia

<sup>a)</sup> Author to whom correspondence should be addressed: [aleksei.penezko@taltech.ee](mailto:aleksei.penezko@taltech.ee). Tel.: +372-56884402.

## ABSTRACT

CuSbSe<sub>2</sub> has great potential for being an earth-abundant absorber material in efficient thin film solar cells. In this study, the radiative recombination in CuSbSe<sub>2</sub> polycrystalline material was studied by temperature and laser power dependent photoluminescence spectroscopy which revealed the band-to-band and band-to-deep acceptor transitions, with the last one involving a deep acceptor defect with an activation energy of  $165 \pm 6$  meV. The observation of the edge emission in CuSbSe<sub>2</sub> refers to the high quality of the synthesized material.

Published under license by AIP Publishing. <https://doi.org/10.1063/1.5114893>

The development of efficient photovoltaic (PV) materials composed of nontoxic and earth abundant elements is of utmost importance to meet the increasing demands for electricity production. Currently, the thin film PV market is dominated by the thin film front-runners CdTe and Cu(In,Ga)Se<sub>2</sub> despite the fact that they face the concern of high toxicity of cadmium and scarcity of indium contained in those materials. This has driven the research to concentrate on other absorber materials made from abundant and environmentally benign elements.<sup>1</sup> In this context, quaternary Cu<sub>2</sub>ZnSn(S,Se)<sub>4</sub> compounds have gained significant attention and reached solar cell efficiencies of 12.6%.<sup>2</sup> The efficiency has plateaued at around 13% already for the past six years, and the researchers are facing the challenge of high open circuit voltage deficit of kesterite solar cells arising from the combination of a high density of trap defect states, band tailing, low carrier lifetime, and material inhomogeneity.

Among alternative compounds, ternary chalcogenide material CuSbSe<sub>2</sub> (CAsE) is one of the p-type semiconductors with great potential having the bandgap in the range from 1.04 eV to 1.2 eV at  $T = 300$  K<sup>3-5</sup> as reported by different research groups and a high optical absorption coefficient of  $\sim 10^5$  cm<sup>-1</sup>.<sup>6</sup> CAsE is a line compound that exists in the very narrow range of chemical compositions and has an orthorhombic layered structure with the space group *Pnma* being therefore crystallographically different from the extensively studied kesterites and chalcopyrites.<sup>7</sup> Due to the narrow single phase material region, the synthesis of phase-pure CuSbSe<sub>2</sub> by the solid state reaction

is rather challenging. Various methods have been used for the synthesis of CAsE crystals including mechanical alloying,<sup>4,8</sup> fusion method,<sup>9</sup> and solvothermal synthesis.<sup>10</sup> Electrodeposition,<sup>11</sup> sputtering,<sup>5,12</sup> and reactive close-spaced sublimation<sup>13</sup> methods have been used for the synthesis of CAsE thin films. In the case of the current record solar cell with an efficiency of 4.7%, the RF sputtering was used for the deposition of CAsE thin film absorbers.<sup>12</sup> Theoretical spectroscopic limited maximum efficiency analysis predicts an efficiency of 27% for the CuSbSe<sub>2</sub> based solar cells, indicating a large space of growth for the practical device efficiency.<sup>14</sup>

Only a couple of reports can be found about the optoelectronic properties of CuSbSe<sub>2</sub>. In few studies, the results of the density functional theory (DFT) calculations have been performed to determine the formation energies and energy levels of possible point defects for different chemical potentials in CAsE.<sup>12,15</sup> Based on the DFT calculations, the dominating defect in Se-rich CAsE is the V<sub>Cu</sub> acceptor being also behind the p-type conductivity of the material. In the case of a Se-poor material, nearly equal formation energies and defect concentrations are predicted by DFT for the V<sub>Cu</sub> acceptor and Cu<sub>i</sub> donor defects, resulting in strong compensation and intrinsic conductivity of the material.<sup>15</sup> Therefore, the Se-poor composition should be avoided if the material is used as the absorber for solar cells. According to the theoretical calculations, the V<sub>Cu</sub> acceptor has a shallow energy level at 0.08 eV above the valence band maximum (VBM) and the Cu<sub>i</sub> donor has an energy level at 0.15 eV below the conduction band minimum

(CBM).<sup>15</sup> From deeper acceptor defects,  $\text{Cu}_{\text{Sb}}$  has the lowest formation energy and has an energy level at 0.29 eV above VBM as predicted by DFT in Ref. 15. On the other hand, theoretical calculations by Welch *et al.*<sup>12</sup> also predict the high probability for the presence of deep selenium vacancies  $V_{\text{Se}}$  with amphoteric character having both donor and acceptor states in the gap, which can lead to photoexcited charge carrier trapping influencing the charge carrier lifetime in CAsE. Transient terahertz spectroscopy measurements have revealed an electron lifetime of 190 ps in CAsE.<sup>12</sup>

Experimentally, Rampino *et al.*<sup>16</sup> have determined from the temperature dependent electrical conductivity measurements the activation energies of acceptor defects of 45 meV and 140 meV in stoichiometric and Cu-poor CAsE, respectively. A deep acceptor level with an activation energy of 0.17 eV was detected by Soliman *et al.*<sup>17</sup> also from the temperature dependent electrical conductivity measurements. Rampino *et al.*<sup>16</sup> have identified in the admittance spectroscopy measurements on Cu-poor CAsE thin films the contribution of a deep defect with the activation energy of 270 meV to the total capacitance of the cell. However, there are no photoluminescence (PL) studies of this compound available in the literature, and therefore, no information is available about the radiative recombination mechanisms and related defects in this compound.

In this study, we synthesize the  $\text{CuSbSe}_2$  polycrystalline material by the melting method. The high purity precursor materials Cu,  $\text{Sb}_2\text{Se}_3$ , and Se were weighted in appropriate ratios (Cu:Sb:Se is 1:1:2) to produce 0.5 g of  $\text{CuSbSe}_2$  and ground in an agate mortar, and the mixture was loaded into a quartz ampoule and degassed. As according to the literature the melting point for CAsE is 490 °C,<sup>18</sup> the synthesis took place above the melting point of the material. The stoichiometric mixture of precursors was heated up in a furnace from room temperature (RT) to 900 °C for 3 h and maintained at this temperature for 1 h. After that, the ampoule was taken out from the furnace and quenched into cold water. The resulting polycrystalline ingot had a diameter of about 6 mm and a length of ~10 mm. For analysis, the ingot was broken into pieces.

The synthesized material was investigated using Raman scattering, X-ray diffraction (XRD), Energy Dispersive X-ray Spectroscopy (EDX), and temperature as well as laser power dependent photoluminescence spectroscopy (PL) to determine the crystallographic properties, phase composition, and defects dominating in the radiative recombination processes in order to improve the understanding of the fundamental properties of this promising absorber material for solar cells.

The crystal structure of the studied CAsE sample was determined by XRD by using a Rigaku Ultima IV diffractometer with monochromatic Cu K $\alpha$ 1 radiation ( $\lambda = 1.5406 \text{ \AA}$ ) at 40 kV and 40 mA operating with the silicon strip detector D/teX Ultra. Micro-Raman spectra were recorded by using a Horiba's LabRam HR800 spectrometer with a 532 nm laser line. For PL excitation and signal detection, the 442 nm line of a He-Cd laser and a Hamamatsu InGaAs detector were used, respectively. A closed-cycle helium cryostat was employed to measure the temperature dependency of the PL spectrum in the temperature range from 10 K to 300 K. The EDX analysis was performed on a Zeiss Merlin high-resolution scanning electron microscope equipped with a Bruker EDX-XFlash6/30 detector.

According to the EDX analysis, the synthesized CAsE polycrystalline material had uniform Sb-rich composition—Cu 24.0 at. %, Sb 26.0 at. %, and Se 50.0 at. %, which corresponds to the chemical

formula  $\text{CuSb}_{1.1}\text{Se}_{2.1}$ . A minor contribution of  $\text{Sb}_2\text{Se}_3$  was also detected by EDX in the studied samples. An example of the EDX mapping of a CAsE polycrystalline material is presented in Fig. 1.

Figure 2 presents the XRD pattern of the studied material mainly consisting of the characteristic peaks of  $\text{CuSbSe}_2$  with orthorhombic structure *Pnma*. The determined lattice parameters  $a = 6.308 \text{ \AA}$ ,  $b = 3.985 \text{ \AA}$ , and  $c = 15.014 \text{ \AA}$  are in good agreement with the experimental data in the literature.<sup>19,20</sup> XRD analysis also revealed the minor contribution of elemental selenium (Se- $\beta$  JDPDF 01-073-2121).

Due to the superposition between the peaks in the XRD pattern of the CAsE and some of the secondary phases, micro-Raman spectroscopy was used as a comparative method for the phase analysis of the synthesized compounds. The Raman spectrum of the CAsE polycrystalline material is presented in Fig. 3 showing the characteristic peaks of  $\text{CuSbSe}_2$  at 103, 139, and 214  $\text{cm}^{-1}$ . In addition, minor contribution of  $\text{Sb}_2\text{Se}_3$  [the shoulder peak at 189  $\text{cm}^{-1}$  (Ref. 21)] to the Raman spectrum was detected. The Raman peaks at 103, 139, and 214  $\text{cm}^{-1}$  are in correspondence with the data presented in Ref. 4 and were assigned to the  $A_g$ ,  $B_{2g}$ , and  $A_g$  vibrational modes of  $\text{CuSbSe}_2$ , respectively.<sup>15</sup>

As mentioned in the introduction of this paper, there are no photoluminescence studies of  $\text{CuSbSe}_2$  available in the literature. We performed a detailed photoluminescence analysis of the synthesized  $\text{CuSbSe}_2$  polycrystalline material using various temperatures and laser excitation powers. The temperature and laser power dependencies of the PL spectrum of CAsE are shown in Figs. 4(a) and 4(b), respectively. The PL spectrum of CAsE at  $T = 10 \text{ K}$  consists of three asymmetric PL bands at 1.28 eV, 1.17 eV, and 0.90 eV, named PL1, PL2, and PL3, respectively. The detected PL bands have a slightly asymmetrical shape with an exponential slope on the low-energy side and were therefore fitted with an empirical asymmetric double sigmoidal function (see the details in Ref. 22) for the detailed analysis of the PL bands. In general, the asymmetric shape of the PL bands is common to compensated multinary semiconductors with a high concentration of native defects that induce spatial potential fluctuations to the material.<sup>23–25</sup> The potential fluctuations will lead to a local perturbation of the band structure, also broadening the defect level distribution and

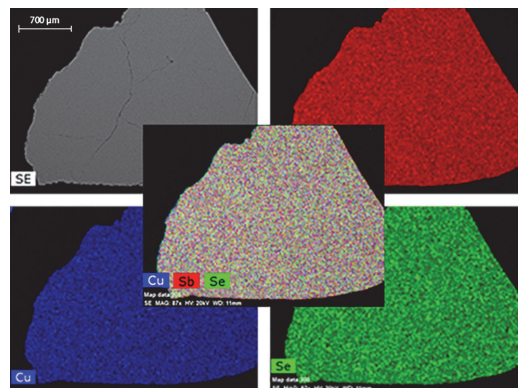


FIG. 1. Elemental composition mapping of a synthesized CAsE polycrystalline material by EDX.

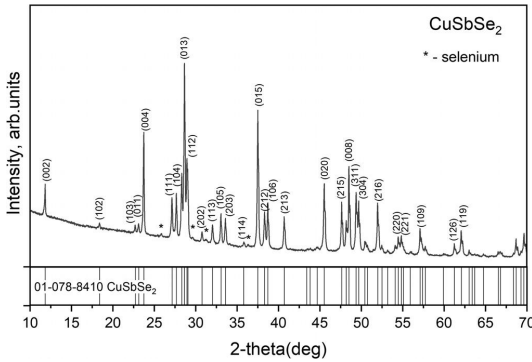


FIG. 2. XRD pattern of the studied CuSbSe<sub>2</sub> polycrystalline material.

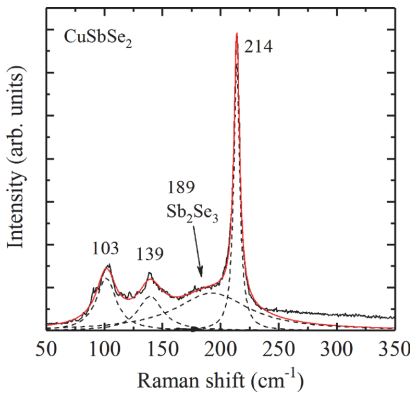


FIG. 3. Raman spectrum of the studied CAsE polycrystalline material showing characteristic peaks of CuSbSe<sub>2</sub> at 103, 139, and 214 cm<sup>-1</sup>. The dashed lines represent the fitting of the spectrum with Lorentz peaks.

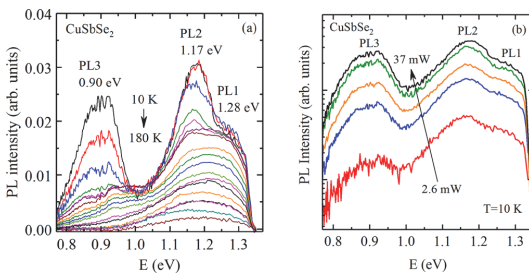


FIG. 4. (a) Temperature and (b) laser power dependencies ( $T = 10$  K) of the PL spectrum of CAsE. Three PL bands at 1.28 eV (PL1), 1.17 eV (PL2), and 0.90 eV (PL3) at  $T = 10$  K were detected.

forming band tails enabling additional recombination paths for the light-generated charge carriers.

From the laser power dependence of the low-temperature PL spectrum of CAsE, a blueshift of the PL1 and PL2 bands with increasing excitation power was detected with the magnitudes of 8 meV/decade and 12 meV/decade, respectively. The peak position of the PL3 band did not vary with the laser power. A large blueshift observed for the PL1 and PL2 bands is typical for the recombination in a material including spatial potential fluctuations and/or bandgap fluctuations and band tails.<sup>22,23</sup> The dependence of the integrated intensity  $\Phi(P)$  of PL bands on the excitation laser power  $P$  is following the sublinear dependence  $\Phi \sim P^m$  as can be seen in Fig. 5. The power coefficient  $m$  can be found as the gradient of the  $\Phi(P)$  plot on a log-log scale as shown in Fig. 5(a) giving values  $m = 1.06$ ,  $m = 0.72$ , and  $m = 0.63$  for the studied PL bands PL1, PL2, and PL3, respectively. The detected  $m$  values for PL2 and PL3 bands are smaller than unity indicate the radiative recombination of charge carriers localized at defects within the bandgap.<sup>26</sup> The  $m$  value above the unity observed for PL1 generally indicates the excitonic or band-to-band transitions.

Figure 5(b) presents the temperature dependencies of the integrated intensities of the PL bands  $\Phi$  from which the thermal activation energies were determined. The linear dependence of  $\ln\Phi(T)$  vs  $1000/T$  at high temperatures was fitted by using the theoretical expression for discrete energy levels,<sup>27</sup>

$$\Phi(T) = \frac{\Phi_0}{1 + \alpha_1 T^{3/2} + \alpha_2 T^{3/2} \exp(-E_T/kT)}, \quad (1)$$

where  $\alpha_1$  and  $\alpha_2$  are the process rate parameters and  $E_T$  is the thermal activation energy. Thermal activation energies  $165 \pm 6$  meV and  $106 \pm 5$  meV were obtained for the PL2 and PL3 bands in CAsE, indicating the involvement of rather deep defects in the radiative recombination processes. There was no linear dependence of  $\ln\Phi(T)$  vs  $1000/T$  at high temperatures for the PL1 band. The temperature dependencies of the peak positions of all three PL bands more or less follow the temperature dependence of the bandgap energy as presented in Ref. 15. The peak position close to the bandgap of CAsE around 1.3 eV at  $T = 10$  K (considering that the bandgap at  $T = 300$  K is 1.2 eV as found in Ref. 5) and the behavior of the PL1 band with laser power and temperature allow us to propose that this emission results from the band-to-band recombination that is usually an indication of good optoelectronic quality of the material.

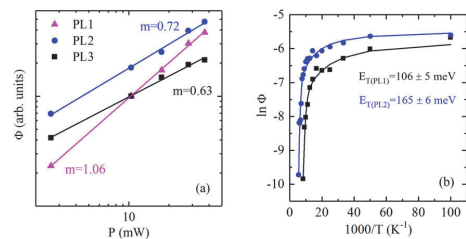


FIG. 5. (a) Integrated PL intensity  $\Phi$  of different PL bands as a function of the laser power  $P$ . The lines are least squares fit to the data. (b) Temperature dependencies of the integrated intensities of the PL bands; solid lines present the fitting results with Eq. (1).

The integrated intensity and the peak position of the PL2 band show the dependence on temperature and laser power typical for the band-to-acceptor transition involving holes localized in the valence band tail and electrons at a deep acceptor level. The obtained thermal activation energy obtained from the quenching of the PL2 band  $165 \pm 6$  meV resembles the position of the deep acceptor level from VBM. Rampino *et al.*<sup>16</sup> and Soliman *et al.*<sup>17</sup> also found deep acceptor defects with similar activation energy from the temperature dependent electrical conductivity measurements.

The PL3 band with a thermal activation energy of  $106 \pm 5$  meV is rather small considering the bandgap of the  $\text{CuSbSe}_2$  at  $T = 10$  K. Such deep PL bands with low activation energy and no shift with laser power are often found to result from the deep donor—deep acceptor recombination in multinary chalcogenide semiconductors.<sup>28,29</sup> The behavior of the PL3 band depending on the temperature and laser power should be studied further and samples presenting this PL band separately would be very useful for the more detailed analysis. We cannot exclude that this PL3 band could also be related to the  $\text{Sb}_2\text{Se}_3$  secondary phase that was detected in the studied samples. Similar deep PL bands showing very small thermal activation energies (on the order of few tenths of meV only) were detected in closely related  $\text{CuSbS}_2$ <sup>30</sup> and attributed to free-to-bound recombination that, however, would require additional explanation of the large discrepancy between the bandgap and PL band position. Hence, such deep PL bands as is PL3 in this study should be investigated further.

In conclusion, the results of a detailed photoluminescence study on a  $\text{CuSbSe}_2$  perspective absorber material for PV applications are presented. Radiative recombination in  $\text{CuSbSe}_2$  polycrystalline material was studied by temperature and laser power dependent photoluminescence spectroscopy that revealed the band-to-band and band-to-deep acceptor transitions. In addition to the edge emission, we were able to detect experimentally from the PL measurements the presence of the theoretically predicted deep acceptor defect with an activation energy of  $165 \pm 6$  meV in the studied  $\text{CuSbSe}_2$ .

This work was supported by Institutional Research Funding No. IUT19-28 and Personal Research Funding No. PUT1495 of the Estonian Ministry of Education and Research and by the European Regional Development Fund, Project No. TK141.

## REFERENCES

- <sup>1</sup>B. Krishnan, S. Shaji, and R. Ernesto Ornelas, *J. Mater. Sci.: Mater Electron* **26**, 4770 (2015).
- <sup>2</sup>W. Wang, M. T. Winkler, O. Gunawan, T. Gokmen, T. K. Todorov, Y. Zhu, and D. B. Mitzi, *Adv. Energy Mater.* **4**, 1301465 (2014).
- <sup>3</sup>T. Wada and T. Maeda, *Phys. Status Solidi C* **14**, 1600196 (2017).
- <sup>4</sup>K. J. Tiwari, V. Vinod, A. Subrahmanyam, and P. Malar, *Appl. Surf. Sci.* **418**, 216 (2017).
- <sup>5</sup>D. Colombara, L. M. Peter, K. D. Rogers, J. D. Painter, and S. Roncallo, *Thin Solid Films* **519**, 7438 (2011).
- <sup>6</sup>A. W. Welch, L. L. Baranowski, P. Zawadzki, S. Lany, C. A. Wolden, and A. Zakutayev, *Appl. Phys. Express* **8**, 082301 (2015).
- <sup>7</sup>F. W. de Souza Lucas, A. W. Welch, L. L. Baranowski, P. C. Dippo, H. Hempel, T. Unold, R. Eichberger, B. Blank, U. Rau, L. H. Mascaro, and A. Zakutayev, *J. Phys. Chem. C* **120**, 18377 (2016).
- <sup>8</sup>D. Zhang, J. Yang, Q. Jiang, L. Fu, Y. Xiao, Y. Luoand, and Z. Zhou, *J. Mater. Chem. A* **4**, 4188 (2016).
- <sup>9</sup>D. Li and X. Y. Qin, *J. Appl. Phys.* **100**, 023713 (2006).
- <sup>10</sup>J. Zhou, G.-Q. Bian, Q.-Y. Zhu, Y. Zhang, C.-Y. Li, and J. Dai, *J. Solid State Chem.* **182**, 259 (2009).
- <sup>11</sup>D. Tang, J. Yang, F. Liu, Y. Lai, J. Li, and Y. Liu, *Electrochim. Acta* **76**, 480 (2012).
- <sup>12</sup>A. W. Welch, L. L. Baranowski, H. Peng, H. Hempel, R. Eichberger, T. Unold, S. Lany, C. Wolden, and A. Zakutayev, *Adv. Energy Mater.* **7**, 1601935 (2017).
- <sup>13</sup>C. Wang, B. Yang, R. Ding, W. Chen, R. Kondrotas, Y. Zhao, S. Lu, Z. Li, and J. Tang, *APL Mater.* **6**, 084801 (2018).
- <sup>14</sup>L. Yu, R. S. Kokenyesi, D. A. Keszler, and A. Zunger, *Adv. Energy Mater.* **3**, 43 (2013).
- <sup>15</sup>D.-J. Xue, B. Yang, Z.-K. Yuan, G. Wang, X. Liu, Y. Zhou, L. Hu, D. Pan, S. Chen, and J. Tang, *Adv. Energy Mater.* **5**, 1501203 (2015).
- <sup>16</sup>S. Rampino, F. Pattini, M. Bronzoni, M. Mazzer, M. Sidoli, G. Spaggiari, and E. Gilioli, *Sol. Energy Mater. Sol. Cells* **185**, 86 (2018).
- <sup>17</sup>L. I. Soliman, A. M. Abo El Soad, H. A. Zayed, and S. A. El Ghfar, *Fiz. A* **11**, 139 (2002).
- <sup>18</sup>B. V. Korzun, V. R. Sobol, M. Rusu, R. M. Savizky, A. A. Fadzeyeva, I. I. Maroz, A. N. Gavrilenko, V. L. Matukhin, and M. Ch. Lux-Steiner, *Mater. Res. Soc. Symp. Proc.* **1735**, 1047 (2016).
- <sup>19</sup>W. Qiu, L. Wu, X. Ke, J. Yang, and W. Zhang, *Sci. Rep.* **5**, 13643 (2015).
- <sup>20</sup>J. Baker, R. S. Kumar, D. Sneed, A. Connolly, Y. Zhang, N. Velisavljevic, J. Paladugu, M. Pravica, C. Chen, A. Cornelius, and Y. Zhao, *J. Alloys Comp.* **643**, 186 (2015).
- <sup>21</sup>X. Ma, Z. Zhang, X. Wang, S. Wang, F. Xu, and Y. Qian, *J. Cryst. Growth* **263**, 491 (2004).
- <sup>22</sup>J. Krustok, H. Collan, M. Yakushev, and K. Hjelt, *Phys. Scr.* **T79**, 179 (1999).
- <sup>23</sup>A. P. Levanyuk and V. V. Osipov, *Sov. Phys. Usp.* **24**, 187 (1981).
- <sup>24</sup>M. Grossberg, T. Raadik, J. Krustok, M. Kauk-Kuusik, K. Timmo, R. Kaupmees, V. Mikli, and A. Mere, *Thin Solid Films* **666**, 44 (2018).
- <sup>25</sup>M. Grossberg, K. Timmo, T. Raadik, E. Kärber, V. Mikli, and J. Krustok, *Thin Solid Films* **582**, 176 (2015).
- <sup>26</sup>T. Schmidt, K. Lischka, and W. Zulehner, *Phys. Rev. B* **45**, 8989 (1992).
- <sup>27</sup>J. Krustok, H. Collan, and K. Hjelt, *J. Appl. Phys.* **81**, 1442 (1997).
- <sup>28</sup>J. Krustok, T. Raadik, M. Grossberg, M. Kauk-Kuusik, V. Trifiletti, and S. Binetti, *Mater. Sci. Semicond. Process.* **80**, 52 (2018).
- <sup>29</sup>J. Krustok, J. H. Schön, H. Collan, M. Yakushev, J. Mäddasson, and E. Bucher, *J. Appl. Phys.* **86**, 364 (1999).
- <sup>30</sup>F. W. de Souza Lucas, H. Peng, S. Johnston, P. C. Dippo, S. Lany, L. H. Mascaro, and A. Zakutayev, *J. Mater. Chem. A* **5**, 21986 (2017).

**Publication II**

M. Grossberg, O. Volobujeva, A. Penezko, R. Kaupmees, T. Raadik, J. Krustok, Origin of photoluminescence from antimony selenide, *Journal of Alloys and Compounds*, Volume 817, 152716, 2020.





Contents lists available at ScienceDirect

## Journal of Alloys and Compounds

journal homepage: <http://www.elsevier.com/locate/jalcom>

## Origin of photoluminescence from antimony selenide

M. Grossberg<sup>a,\*</sup>, O. Volobujeva<sup>a</sup>, A. Penezko<sup>a</sup>, R. Kaupmees<sup>a</sup>, T. Raadik<sup>a</sup>, J. Krustok<sup>a,b</sup><sup>a</sup> Department of Materials and Environmental Technology, Tallinn University of Technology, Ehitajate Tee 5, 19086, Tallinn, Estonia<sup>b</sup> Division of Physics, Tallinn University of Technology, Ehitajate Tee 5, 19086, Tallinn, Estonia

## ARTICLE INFO

## Article history:

Received 26 July 2019

Received in revised form

15 October 2019

Accepted 16 October 2019

Available online 17 October 2019

## Keywords:

Sb<sub>2</sub>Se<sub>3</sub>

Photoluminescence

Defects

Donor-acceptor pairs

## ABSTRACT

Antimony selenide (Sb<sub>2</sub>Se<sub>3</sub>) absorber material has great potential for low-cost photovoltaics due to its excellent optoelectronic properties and low processing temperatures. This study presents detailed temperature and excitation power dependent photoluminescence (PL) analysis of Sb<sub>2</sub>Se<sub>3</sub> polycrystals revealing the dominating radiative recombination mechanisms and related defects in the studied material. The low-temperature (T = 10 K) PL spectrum consisted of three bands at 0.94 eV, 1.10 eV and 1.24 eV, the last one located close to the low-temperature band gap of Sb<sub>2</sub>Se<sub>3</sub> 1.32 eV. The PL bands at 1.24 eV and 0.94 eV were found to originate from the donor-acceptor pair recombination, the first one at 1.24 eV involving more distant pairs while the second one at 0.94 eV resulting from the deep acceptor – deep donor pair recombination. Third PL band at 1.10 eV is proposed to be related to the grain boundaries.

© 2019 Elsevier B.V. All rights reserved.

## 1. Introduction

Antimony selenide (Sb<sub>2</sub>Se<sub>3</sub>) belongs to V<sub>2</sub>–VI<sub>3</sub> (V = As, Sb, Bi; VI = S, Se, Te) binary materials that have been attracting research interest due to their potential applications in photovoltaic and thermoelectric devices, as well as in Li- and Na-ion batteries [1–3]. Its constituent elements are of low-toxicity, earth-abundant, and inexpensive. Sb<sub>2</sub>Se<sub>3</sub> is a p-type material with high absorption coefficient (>10<sup>5</sup> cm<sup>-1</sup> at short wavelength [4]) and nearly optimal band gap energy for solar energy conversion around 1.2 eV at T = 300 K [5]. Solar cells based on core-shell structured Sb<sub>2</sub>Se<sub>3</sub> nanorod array have recently reached efficiencies of 9.2% [6].

From the structural properties point of view, Sb<sub>2</sub>Se<sub>3</sub> is a one-dimensional line type compound consisting of covalently bonded (Sb<sub>4</sub>Se<sub>6</sub>)<sub>n</sub> ribbons that are stacked together by van der Waals forces and crystallizing in orthorhombic crystal structure with space group *Pbnm* [6]. The Sb<sub>2</sub>Se<sub>3</sub> grains can grow in a columnar manner enabling effective charge carrier transport in one direction. Both, direct and indirect band gap of Sb<sub>2</sub>Se<sub>3</sub> have been detected [6,7]. Chen et al. [7] determined indirect band gap E<sub>g,i</sub> = 1.03 ± 0.01 eV and direct band gap of E<sub>g,d</sub> = 1.17 ± 0.02 eV at 300 K from the optical absorption measurements of Sb<sub>2</sub>Se<sub>3</sub> thin films. The energetic

difference between the indirect and direct band gap of Sb<sub>2</sub>Se<sub>3</sub> decreases towards lower temperatures and was found to be only 0.04 eV at T = 0 K.

Defects in the absorber material play a crucial role in determining the solar cell performance. There is very little information available about the defects in Sb<sub>2</sub>Se<sub>3</sub>. Recently, a comprehensive study of the first-principles calculations of the defects in Sb<sub>2</sub>Se<sub>3</sub> was published by Huang et al. [8] stating that due to the low symmetry of the quasi-one-dimensional structure of Sb<sub>2</sub>Se<sub>3</sub>, a series of donor and acceptor levels are predicted in the band gap of the material since each point defect located at non-equivalent atomic sites can have very different properties. Even the presence of some uncommon defects in binary chalcogenide compounds such as the two-anion-replace-one-cation antisite 2Se<sub>Sb</sub> producing a shallow acceptor level is predicted by the theoretical calculations in the same study [8].

The ab initio calculations predict V<sub>Sb</sub> and Se<sub>Sb</sub> as dominant acceptor defects in Se-rich Sb<sub>2</sub>Se<sub>3</sub> that is aimed for the PV applications [8–10]. Chen et al. [11] and Liu et al. [10] have experimentally determined an acceptor defect level with E<sub>a</sub> = 111 meV and E<sub>a</sub> = 107 meV from the temperature dependent conductivity measurements, respectively. It was assigned to Se<sub>Sb</sub> defect as it is predicted by theoretical calculations as the defect with the lowest formation energy in Sb<sub>2</sub>Se<sub>3</sub> with the energy level at about 0.1 eV above the valence band edge [8,10]. The same defect was detected also in admittance spectroscopy measurements with E<sub>a</sub> = 95 meV and the density of defects states about

\* Corresponding author.

E-mail address: [maarja.grossberg@taltech.ee](mailto:maarja.grossberg@taltech.ee) (M. Grossberg).



$1 \times 10^{15} \text{ cm}^{-3} \text{ eV}^{-1}$  [11]. The two deep acceptor defects with energy levels at  $E_V+0.48 \text{ eV}$  and  $E_V+0.71 \text{ eV}$  detected in  $\text{Sb}_2\text{Se}_3$  by deep level transient spectroscopy (DLTS) were assigned to  $V_{\text{Sb}}$  and  $\text{Se}_{\text{Sb}}$ , correspondingly [12]. The donor defect at  $E_C - 0.61 \text{ eV}$  detected in the same DLTS study, was assigned to  $\text{Sb}_{\text{Se}}$  donor. Recently, Tao et al. [13] published a temperature dependent admittance spectroscopy study on  $\text{Sb}_2\text{Se}_3$  solar cells with an efficiency of over 7% and detected the presence of three deep defect levels at 363 meV, 398 meV, and 435 meV, however, no assignment of the defects is provided to the reader. Interestingly, it was also found in Ref. [12] that in different samples, the defect densities of  $\text{Se}_{\text{Sb}}$  and  $\text{Sb}_{\text{Se}}$  are always very similar suggesting that they might form  $[\text{Se}_{\text{Sb}} + \text{Sb}_{\text{Se}}]$  defect complexes as is also predicted in the recent study by Huang et al. [8].

Photoluminescence is a valuable tool for studying recombination mechanisms and related defects in a semiconductors, however, no defect studies of  $\text{Sb}_2\text{Se}_3$  by luminescence methods could be found in the literature. Only a low-temperature ( $T = 7 \text{ K}$ ) PL spectra of  $\text{Sb}_2\text{Se}_3$  thin films were reported by Shongalova et al. [14], where the presence of two broad ( $\sim 100 \text{ meV}$ ) deep PL bands at 0.75 eV and 0.85 eV is detected. However, there is no analysis of the data presented to the reader. Hence, the aim of this study is to fulfil the gap and provide a detailed analysis of the PL spectra of high quality  $\text{Sb}_2\text{Se}_3$  polycrystals to reveal the radiative recombination mechanisms and related defects.

**2. Experimental**

The 5 N purity  $\text{Sb}_2\text{Se}_3$  polycrystals from Alfa Aesar were post-annealed in isothermal sealed quartz ampoules at  $T = 623 \text{ K}$  in Ar atmosphere (100 Torr) in the presence of additional Se source for 30 min as these were found to be the optimal post-treatment conditions for  $\text{Sb}_2\text{Se}_3$  thin films studied in parallel in order to obtain photoconductive  $\text{Sb}_2\text{Se}_3$  with uniform stoichiometric composition.

The elemental and phase composition of the sample were determined by Energy Dispersive X-ray spectroscopy (EDX) and Raman spectroscopy. The EDX analysis was performed on Zeiss Merlin high-resolution scanning electron microscope equipped with the Bruker EDX-XFlash6/30 detector. According to the EDX analysis, the  $\text{Sb}_2\text{Se}_3$  samples have close to stoichiometric composition, being very slightly Se-rich. Micro-Raman spectra were recorded by using a Horiba's LabRam HR800 spectrometer with a 532 nm laser line with the spot size of 10  $\mu\text{m}$  in diameter. The crystal structure of the studied  $\text{Sb}_2\text{Se}_3$  was determined by X-ray

diffraction (XRD) by using a Rigaku Ultima IV diffractometer with monochromatic Cu K $\alpha$ 1 radiation ( $\lambda = 1.5406 \text{ \AA}$ ) at 40 kV and 40 mA operating with the silicon strip detector D/teX Ultra. The lattice constants were determined using the Rietveld refinement procedure by Rigaku PDXL version 1.4.0.3 software.

A 0.64 m focal length single grating ( $600 \text{ mm}^{-1}$ ) monochromator and the 442 nm line of a He–Cd laser with different power and spot size of 100  $\mu\text{m}$  in diameter were used for the PL measurements. For PL signal detection a Hamamatsu InGaAs photomultiplier tube was used. A closed-cycle helium cryostat was employed to measure temperature dependencies of the PL spectra at temperatures from 10 K to 300 K.

The photoreflectance (PR) measurements were made with a traditional setup [15] where the  $f = 64 \text{ cm}$  grating monochromator together with a 250 W halogen bulb was used as a primary beam and a 45 mW He–Cd laser (441 nm) as a secondary beam. The reflectance signal at 85 Hz was detected using a Si detector with a lock-in amplifier in the spectral range from 1.1 to 1.3 eV.

**3. Results and discussion**

*3.1. Structural properties*

The XRD pattern and the Raman spectrum of the studied  $\text{Sb}_2\text{Se}_3$  polycrystals are presented in Fig. 1a and Fig. 1b, respectively. According to the XRD analysis, the material crystallizes in orthorhombic structure of  $\text{Sb}_2\text{Se}_3$  with space group  $Pnma 62$  (ICDD: 01-083-7430). All detected XRD peaks belong to  $\text{Sb}_2\text{Se}_3$ , only main diffraction peaks are labelled for the clarity of the figure. The following lattice parameters were determined:  $a = 1.17833(10) \text{ nm}$ ,  $b = 0.39776(6) \text{ nm}$  and  $c = 1.1634(2) \text{ nm}$  being in correspondence with the data reported by other research groups [16].

The characteristic Raman spectrum of the studied  $\text{Sb}_2\text{Se}_3$  consisted of 6 Raman peaks at 99, 125, 155, 185, 191 and 213  $\text{cm}^{-1}$ , the Raman peak at 191  $\text{cm}^{-1}$  being the dominant one. The obtained Raman spectrum is in good correlation with the recently published data by Shongalova et al. [17] showing that the often found Raman mode around 250  $\text{cm}^{-1}$  that is absent in our samples is corresponding to  $\text{Sb}_2\text{O}_3$  instead of  $\text{Sb}_2\text{Se}_3$ . No contribution from the secondary phases to the XRD pattern and to the Raman spectrum of the studied material could be detected.

*3.2. Photoreflectance and photoluminescence results*

For determining the band gap of the studied  $\text{Sb}_2\text{Se}_3$  polycrystals,

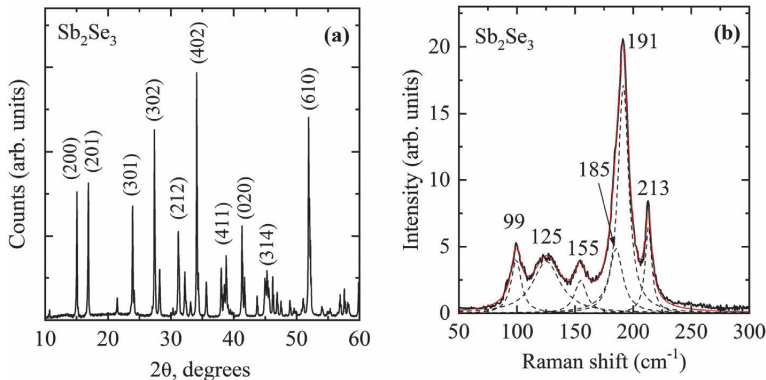


**Fig. 1.** The XRD pattern (a) and the Raman spectrum (b) of the studied  $\text{Sb}_2\text{Se}_3$  polycrystals indicating to the single phase material.

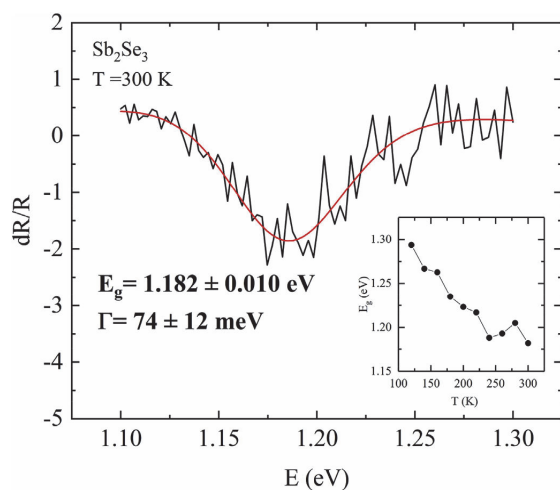


**Fig. 2.** PR spectrum of the studied  $\text{Sb}_2\text{Se}_3$  crystals at  $T=300\text{K}$ . The red solid line presents the fitting of the experimental data with Eq. (1). The inset graph presents the temperature dependence of the bandgap energy of the material determined from the PR spectra in the temperature region from 120 K to 300 K. (For interpretation of the references to colour in this figure legend, the reader is referred to the Web version of this article.)

photoreflectance spectroscopy in the temperature range from 120 K to 300 K was used. The PR spectrum of  $\text{Sb}_2\text{Se}_3$  at  $T=300\text{K}$  is presented in Fig. 2. The measured PR spectra were analyzed by the low-field line-shape function with a third derivative functional form, developed by Aspnes [18]:

$$\frac{\Delta R}{R} = \text{Re} \left[ A e^{i\phi} (E - E_g + i\Gamma)^{-n} \right], \quad (1)$$

where  $E$  is the photon energy and  $A$ ,  $\phi$ ,  $E_g$ , and  $\Gamma$  are the amplitude, phase, optical transition energy, and broadening parameter of the spectrum, respectively. The exponent  $n$  in Eq. (1) depends on the type of the critical point, and determining its proper value is of particular importance in analyzing PR spectra.  $n=2.5$ , corresponding to a three-dimensional critical point, was used for the fitting of all PR spectra. The band gap  $E_g = 1.182 \pm 0.010\text{ eV}$  and the broadening parameter  $\Gamma = 74 \pm 12\text{ meV}$  were found for  $\text{Sb}_2\text{Se}_3$  at  $T=300\text{K}$ . The temperature dependence of the bandgap energy of  $\text{Sb}_2\text{Se}_3$  presented in the inset graph of Fig. 2 is in very good agreement with the data presented in Ref. [5], however, they found slightly larger broadening parameter  $\Gamma = 82\text{ meV}$  at  $T=300\text{K}$ .

The temperature dependence of the PL spectrum of the studied  $\text{Sb}_2\text{Se}_3$  polycrystals in the temperature region from  $T=10\text{K}$  to  $T=90\text{K}$  is presented in Fig. 3. The inset graph presents the fitting of the spectrum at  $T=10\text{K}$  with an empirical asymmetric double sigmoid function [19] resulting in three PL bands positioned at 1.24 eV (PL1), 1.10 eV (PL2) and 0.94 eV (PL3). The PL bands have slightly asymmetric shape with a steeper decline at high-energy side and a nearly temperature independent incline at the low-energy side that is common in semiconductors with band tails [20]. The average depth of the band edge fluctuations determined from the low energy side of the PL1 band at  $T=10\text{K}$  according to Ref. [20] is  $\gamma = 17\text{ meV}$ , which is smaller than the Urbach energy 38 meV at  $T=300\text{K}$  found by Chen et al. in Ref. [11] indicating to the good quality of our studied polycrystals.

The temperature dependence of the PL bands positions (Fig. 4a) revealed a slight shift towards higher energies in the case of the PL1

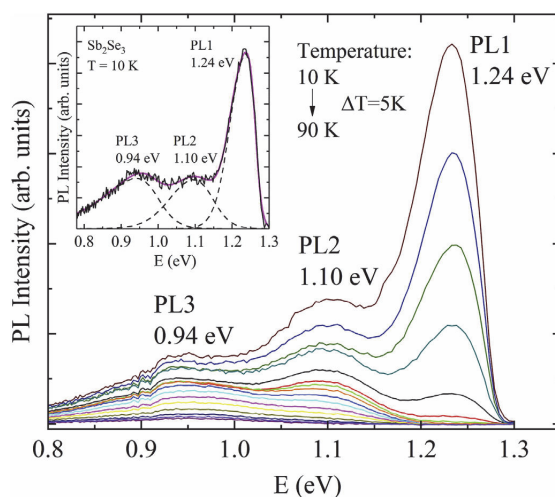


**Fig. 3.** The temperature dependence of the PL spectrum of the studied  $\text{Sb}_2\text{Se}_3$  polycrystals. The inset figure presents an example of the fitting of the spectra.

and PL3 bands. PL2 band peak position shows a red-shift larger than the temperature dependence of the band gap [5]. The thermal activation energies for the bands obtained from the Arrhenius plot (Fig. 4b) where the dependence of  $\ln(I)$  versus  $1000/T$  at high temperatures was fitted by using theoretical expression for discrete energy levels [21]:

$$\Phi(T) = \frac{\Phi_0}{1 + \alpha_1 T^{3/2} + \alpha_2 T^{3/2} \exp(-E_T/kT)}, \quad (2)$$

where  $\Phi$  is integrated intensity,  $\alpha_1$  and  $\alpha_2$  are the process rate parameters and  $E_T$  is the thermal activation energy. As predicted by the fast quenching of the PL spectra with temperature (see Fig. 3) small thermal activation energies  $E_{T(\text{PL1})} = 33 \pm 5\text{ meV}$ ,  $E_{T(\text{PL2})} = 65 \pm 6\text{ meV}$  and  $E_{T(\text{PL3})} = 93 \pm 3\text{ meV}$  were obtained.

Considering the low temperature band gap of  $\text{Sb}_2\text{Se}_3$   $E_g = 1.32\text{ eV}$  [5,7], the positions of the detected PL bands at  $T=10\text{K}$  being quite distant from the band gap, and the obtained small thermal activation energies, one can propose that the PL1 and PL3 bands most probably arise from the donor-acceptor pair (DAP) recombination. The presence of high concentration of donor-acceptor pairs is also predicted by the theoretical calculations [8].

To analyze the recombination mechanisms behind the PL bands, also the laser power dependence of the PL spectra was measured at  $T=10\text{K}$ , see Fig. 5. The inset graphs present the laser power dependencies of the PL bands positions and intensities. The dependence of the integrated intensity  $\Phi(P)$  of PL bands on the excitation laser power  $P$  is following the dependence  $\Phi \sim P^m$  as can be seen from the inset graph in Fig. 5. The power coefficient  $m$  can be found as the gradient of the  $\Phi(P)$  plot on a log-log scale as shown in upper inset graph in Fig. 5 giving  $m \sim 0.6$  for all three PL bands. The detected  $m$  value which is smaller than unity indicates to the radiative recombination of charge carriers localized at defects within the band gap for all three PL bands [22].

The peak position of the PL2 and PL3 bands varied only slightly (less than 1 meV/decade) with the laser power. A blueshift of the PL1 band with increasing excitation power was detected with the magnitude of 3 meV/decade, which is characteristic to donor-acceptor pair recombination as well as to a semiconductor

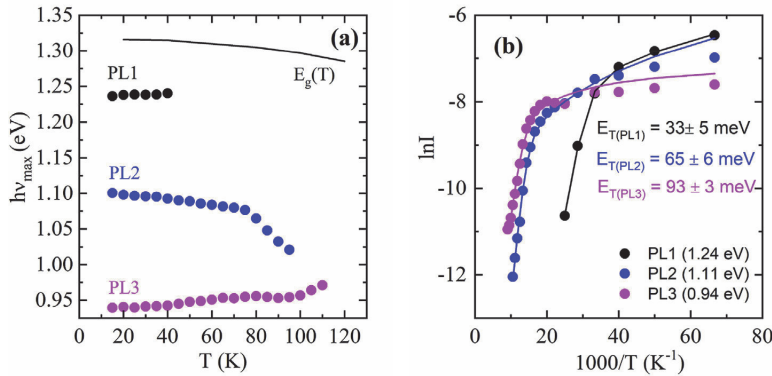


Fig. 4. The temperature dependence of the PL band peak positions together with the band gap energy  $E_g$  from Ref. [5] presented as solid line (a), and the Arrhenius plot (b) showing the thermal activation energies for the studied three PL bands in  $\text{Sb}_2\text{Se}_3$  obtained from the fitting of the curves with Eq. (2).

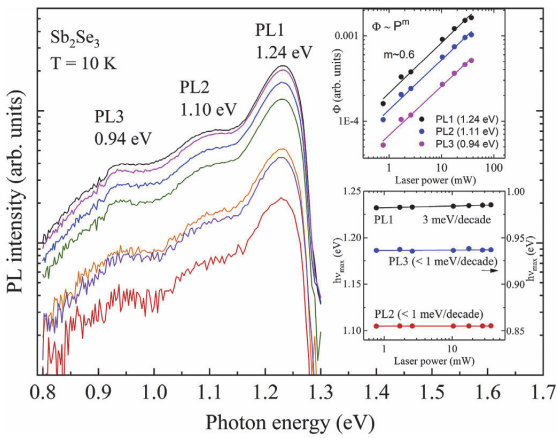


Fig. 5. The laser power dependence of the PL bands of  $\text{Sb}_2\text{Se}_3$  at  $T = 10\text{ K}$ . The inset graphs present the laser power dependencies of the PL bands peak positions (bottom graph) and intensities (upper graph).

involving band tails [20]. The emission energy from a donor-acceptor pair separated by a distance  $r$  can be calculated by the following equation [23]:

$$h\nu_{\max} = E_g - (E_a + E_d) + \frac{e^2}{4\pi\epsilon_0\epsilon r}, \quad (3)$$

where  $E_g$  is the bandgap energy,  $E_a$  and  $E_d$  are the acceptor and donor ionization energies, respectively,  $r$  is the distance between the donor and acceptor,  $e$  is the electron charge,  $\epsilon$  is the static dielectric constant, and  $\epsilon_0$  is the permittivity of vacuum. The last term of Eq. (3) describes the Coulomb interaction between the donor and acceptor defects. The relatively small shift of the PL3 band with laser power and rather "deep" peak position indicate to the DAP recombination via very close donor-acceptor pairs, while the PL1 band involves DAP with larger distance between donor and acceptor defects.

Due to a low symmetry of  $\text{Sb}_2\text{Se}_3$  crystal lattice, 2 different lattice sites for Sb and 3 different sites for Se exist [24]. The closest distance  $r = 0.2588\text{ nm}$  is between Se(1) and Sb(2) sites

corresponding to the Coulomb energy of 232 meV ( $\epsilon = 24$  [11]). Considering the peak position of the PL3 band, the thermal activation energy, and the bandgap energy of  $\text{Sb}_2\text{Se}_3$ , similar value for the Coulomb energy for the PL3 band is expected. Accordingly, our results show that we have a donor-acceptor pair, where the donor and acceptor defects occupy closest Se and Sb sites in the lattice. These so-called deep donor-deep acceptor pairs (DD-DA) were discovered previously in CdTe [25], in chalcopyrites [26], and in kesterites [27]. It is known that the electron (hole) wave function in the deep donor (acceptor) level must be highly localized. Therefore, for more distant pairs, there is practically no overlapping of carriers wave functions and, consequently, no observable recombination emission. According to Ref. [8] all single defects in  $\text{Sb}_2\text{Se}_3$  are quite deep and therefore they indeed can form DD-DA pairs. When paired, single acceptor and donor defect levels are pushed towards band edges and the thermal activation energy of these complexes will become quite small. While the PL1 band of more distant pairs shows a certain blueshift with increased excitation intensity, the PL3 band corresponding to DD-DA pairs practically does not shift. Moreover, DA pairs having somewhat larger separation and thus smaller Coulomb energy can cause the observed slightly asymmetric shape of the PL bands in addition to the broadening caused by the band tails. For example, Sb(1)-Se(3) sites are separated by the distance  $r = 0.2664\text{ nm}$  and the corresponding Coulomb energy is only about 7 meV smaller than for the closest distance.

The shallowest single acceptor defect in slightly Se-rich  $\text{Sb}_2\text{Se}_3$  is  $\text{Se}_{\text{Sb}(1)}$  defect having a depth of about 100 meV [8,11]. We can assume, that this defect is a component of DA pair responsible for the PL1 band. The corresponding donor defect is not clear and requires further studies.

The PL2 band behaves differently from the PL1 and PL3 bands referring to a different type of recombination. According to Fig. 4 (a), the PL2 band peak position shows a red-shift comparable or even slightly larger than the temperature dependence of the band gap energy and it is independent of the magnitude of the laser power. However, taking into account the PL2 band peak position, the low-temperature band gap of  $\text{Sb}_2\text{Se}_3$   $E_g = 1.32\text{ eV}$  [5,7] and the thermal activation energy for this PL band, it cannot be attributed to a simple band-to-acceptor recombination. Moreover, the observed peak position shift with temperature is an indication of the involvement of the band states in the recombination process for the PL2 band. Therefore, we propose that the most probable origin of the PL2 band is related to grain boundaries. There are different models about PL in the vicinity of grain boundaries, they all are

based on band bending and thus on local reduction of bandgap energy or the depth of defect levels. In this case, the recombination can occur through tunneling processes near grain boundaries, where a significant band bending is present. Similar model was proposed also for Z-bands in CdTe [28]. In our polycrystalline samples the concentration of grain boundaries is quite high and therefore the intensity of the PL2 band is also relatively high. Of course, further studies must be performed to clarify this recombination related to grain boundaries.

#### 4. Conclusion

In conclusion, the results of a detailed photoluminescence study on  $\text{Sb}_2\text{Se}_3$  as perspective absorber material for PV applications is presented. Radiative recombination in  $\text{Sb}_2\text{Se}_3$  polycrystals was studied by temperature and laser power dependent photoluminescence spectroscopy that revealed the origin for the detected PL bands at 1.24 eV and 0.94 eV as donor-acceptor pair recombination. The PL1 band involves more distant donor-acceptor pairs while the PL3 band results from the deep donor – deep acceptor recombination. These results are in agreement with the theoretical defect calculations that predict high concentration of donor-acceptor pairs in this low symmetry quasi-one-dimensional  $\text{Sb}_2\text{Se}_3$  material. Third PL band at 1.10 eV is proposed to be related to the grain boundaries, but requires further studies to clarify the recombination model behind this PL band.

#### Declaration of competing interest

The authors declare that they have no known competing financial interests or personal relationships that could have appeared to influence the work reported in this paper.

#### Acknowledgements

This work has been supported by institutional research funding IUT19-28 and personal research funding PUT1495 of the Estonian Ministry of Education and Research, and by the European Regional Development Fund, Project TK141.

#### References

- R. Venkatasubramanian, E. Siivola, T. Colpitts, B. O'Quinn, Thin-Film thermoelectric devices with high room-temperature figures of merit, *Nature* 413 (2001) 597–602, <https://doi.org/10.1038/35098012>.
- K. Zeng, D.-J. Xue, J. Tang, Antimony selenide thin-film solar cells, *Semicond. Sci. Technol.* 31 (2016), 063001, <https://doi.org/10.1088/0268-1242/31/6/063001>.
- W. Luo, A. Calas, C. Tang, F. Li, L. Zhou, L. Mai, Ultralong  $\text{Sb}_2\text{Se}_3$  nanowire-based free-standing membrane anode for lithium/sodium ion batteries, *ACS Appl. Mater. Interfaces* 8 (2016) 35219–35226, <https://doi.org/10.1021/acsami.6b11544>.
- Y. Zhou, M. Leng, Z. Xia, J. Zhong, H. Song, X. Liu, B. Yang, J. Zhang, J. Chen, K. Zhou, J. Han, Y. Cheng, J. Tang, Solution-processed antimony selenide heterojunction solar cells, *Adv. Energy Mater.* 4 (2014), 1301846, <https://doi.org/10.1002/aenm.201301846>.
- M. Birkett, W.M. Linhart, J. Stoner, L.J. Phillips, K. Durose, J. Alaria, J.D. Major, R. Kudrawiec, T.D. Veal, Band gap temperature-dependence of close-space sublimation grown  $\text{Sb}_2\text{Se}_3$  by photo-reflectance, *Appl. Mater.* 6 (2018), 084901, <https://doi.org/10.1063/1.5027157>.
- Z. Li, X. Liang, G. Li, H. Liu, H. Zhang, J. Guo, J. Chen, K. Shen, X. San, W. Yu, R.E.I. Schropp, 9.2%-efficient core-shell structured antimony selenide nanorod array solar cells, *Nat. Commun.* 10 (2019) 125, <https://doi.org/10.1038/s41467-018-07903-6>.
- C. Chen, W. Li, Y. Zhou, C. Chen, M. Luo, X. Liu, K. Zeng, B. Yang, C. Zhang, J. Han, J. Tang, Optical properties of amorphous and polycrystalline  $\text{Sb}_2\text{Se}_3$  thin films prepared by thermal evaporation, *Appl. Phys. Lett.* 107 (2015), 043905, <https://doi.org/10.1063/1.4927741>.
- M. Huang, P. Xu, D. Han, J. Tang, S. Chen, Complicated and unconventional defect properties of the quasi-one-dimensional photovoltaic semiconductor  $\text{Sb}_2\text{Se}_3$ , *ACS Appl. Mater. Interfaces* 11 (2019) 15564–15572, <https://doi.org/10.1021/acsami.9b01220>.
- H. Guo, Z. Chen, X. Wang, Q. Cang, X. Jia, C. Ma, N. Yuan, J. Ding, Enhancement in the efficiency of  $\text{Sb}_2\text{Se}_3$  thin-film solar cells by increasing carrier concentration and inducing columnar growth of the grains, *Sol. RRL* 3 (2019), 1800224, <https://doi.org/10.1002/solr.201800224>.
- X. Liu, X. Xiao, Y. Yang, D.J. Xue, D. Li, C. Chen, S. Lu, L. Gao, Y. He, G. Wang, S. Chen, J. Tang, Enhanced  $\text{Sb}_2\text{Se}_3$  solar cell performance through theory-guided defect control, *Prog. Photovolt. Res. Appl.* 25 (2017) 861–870, <https://doi.org/10.1002/pip.2900>.
- C. Chen, D.C. Bobela, Y. Yang, S. Lu, K. Zeng, C. Ge, B. Yang, L. Gao, Y. Zhao, M.C. Beard, J. Tang, Characterization of basic physical properties of  $\text{Sb}_2\text{Se}_3$  and its relevance for photovoltaics, *Front. Optoelectron.* 10 (2017) 18–30, <https://doi.org/10.1007/s12200-017-0702-z>.
- X. Wen, C. Chen, S. Lu, K. Li, R. Kondrotas, Y. Zhao, W. Chen, L. Gao, C. Wang, J. Zhang, G. Niu, J. Tang, Vapor transport deposition of antimony selenide thin film solar cells with 7.6% efficiency, *Nat. Commun.* 9 (2018) 2179, <https://doi.org/10.1038/s41467-018-04634-6>.
- J. Tao, X. Hu, Y. Hong, K. Li, J. Jiang, S. Chen, C. Jing, F. Yue, P. Yang, C. Zhang, Z. Wu, J. Tang, J. Chu, Investigation of electronic transport mechanisms in  $\text{Sb}_2\text{Se}_3$  thin-film solar cells, *Sol. Energy Mater. Sol. Cells* 197 (2019) 1–6, <https://doi.org/10.1016/j.solmat.2019.04.003>.
- A. Shongalova, M.R. Correia, J.P. Teixeira, J.P. Leitão, J.C. González, S. Ranjbar, S. Garud, B. Vermang, J.M.V. Cunha, P.M.P. Salomé, P.A. Fernandes, Growth of  $\text{Sb}_2\text{Se}_3$  thin films by selenization of RF sputtered binary precursors, *Sol. Energy Mater. Sol. Cells* 187 (2018) 219–226, <https://doi.org/10.1016/j.solmat.2018.08.003>.
- T. Raadik, J. Krustok, M.V. Yakushev, Photoreflectance study of  $\text{AgGaTe}_2$  single crystals, *Phys. B Condens. Matter* 406 (2011) 418–420, <https://doi.org/10.1016/j.physb.2010.11.002>.
- L.J. Phillips, C.N. Savory, O.S. Hutter, P.J. Yates, H. Shiel, S. Mariotti, L. Bowen, M. Birkett, K. Durose, D.O. Scanlon, J.D. Major, Current enhancement via a  $\text{TiO}_2$  window layer for  $\text{CSS Sb}_2\text{Se}_3$  solar cells: performance limits and high Voc, *IEEE J. Photovolt.* 9 (2019) 544–551, <https://doi.org/10.1109/JPHOTOV.2018.2885836>.
- A. Shongalova, M.R. Correia, B. Vermang, J.M.V. Cunha, P.M.P. Salomé, P.A. Fernandes, On the identification of  $\text{Sb}_2\text{Se}_3$  using Raman scattering, *MRS Commun.* 8 (2018) 865–870, <https://doi.org/10.1557/mrc.2018.94>.
- D.E. Aspnes, *Handbook on Semiconductors. Vol. 2. Optical Properties of Solids*, North-Holland Publishing Company, Amsterdam, 1980.
- J. Krustok, H. Collan, M. Yakushev, K. Hjelt, The role of spatial potential fluctuations in the shape of the PL bands of multinary semiconductor compounds, *Phys. Scr.* T79 (1999) 179–182, <https://doi.org/10.1238/Physica.Topical.079a00179>.
- A.P. Levanyuk, V.V. Osipov, Edge luminescence of direct-gap semiconductors, *Sov. Phys. Uspekhi* 24 (1981) 187–215, <https://doi.org/10.1070/PU1981v024n03ABEH004770>.
- J. Krustok, H. Collan, K. Hjelt, Does the low-temperature Arrhenius plot of the photoluminescence intensity in CdTe point towards an erroneous activation energy? *J. Appl. Phys.* 81 (1997) 1442, <https://doi.org/10.1063/1.363903>.
- T. Schmidt, K. Lischka, W. Zulehner, Excitation-power dependence of the near-band-edge photoluminescence of semiconductors, *Phys. Rev. B* 45 (1992) 8989, <https://doi.org/10.1103/PhysRevB.45.8989>.
- F. Williams, Donor–acceptor pairs in semiconductors, *Phys. Status Solidi* 25 (1968) 493–512, <https://doi.org/10.1002/pssb.19680250202>.
- V.L. Deringer, R.P. Stoffel, M. Wuttig, R. Dronskowski, Vibrational properties and bonding nature of  $\text{Sb}_2\text{Se}_3$  and their implications for chalcogenide materials, *Chem. Sci.* 6 (2015) 5255–5262, <https://doi.org/10.1039/c5sc00825e>.
- J. Krustok, H. Collan, K. Hjelt, J. Mádasson, V. Valdna, Photoluminescence from deep acceptor-deep donor complexes in CdTe, *J. Lumin.* 72–74 (1997) 103–105, [https://doi.org/10.1016/S0022-2313\(97\)00061-6](https://doi.org/10.1016/S0022-2313(97)00061-6).
- J. Krustok, J. Raudoja, J.H. Schön, M. Yakushev, H. Collan, The role of deep donor–deep acceptor complexes in CIS-related compounds, *Thin Solid Films* 361–362 (2000) 406–410, [https://doi.org/10.1016/S0040-6090\(99\)00756-7](https://doi.org/10.1016/S0040-6090(99)00756-7).
- J. Krustok, T. Raadik, M. Grossberg, M. Kauk-Kuusik, V. Trifiletti, S. Binetti, Photoluminescence study of deep donor–deep acceptor pairs in  $\text{Cu}_2\text{ZnSnS}_4$ , *Mater. Sci. Semicond. Process.* 80 (2018) 52–55, <https://doi.org/10.1016/j.mssp.2018.02.025>.
- J. Krustok, J. Mádasson, J. Hiie, Photoluminescence properties of Z- bands in CdTe, *Phys. Status Solidi (a)* 165 (1998) 517–525, [https://doi.org/10.1002/\(SICI\)1521-396X\(199802\)165:2%3C517::AID-PSSA517%3E3.0.CO;2-G](https://doi.org/10.1002/(SICI)1521-396X(199802)165:2%3C517::AID-PSSA517%3E3.0.CO;2-G).



**Publication III**

A. Penezko, M. Kauk-Kuusik, O. Volobujeva, M. Grossberg, Properties of Cu-Sb-Se thin films deposited by magnetron co-sputtering for solar cell applications, Thin Solid Films 740, 139004, 2021.





Contents lists available at ScienceDirect

## Thin Solid Films

journal homepage: [www.elsevier.com/locate/tsf](http://www.elsevier.com/locate/tsf)

# Properties of Cu-Sb-Se thin films deposited by magnetron co-sputtering for solar cell applications

A. Penezko<sup>\*</sup>, M. Kauk-Kuusik, O. Volobujeva, M. Grossberg

Department of Materials and Environmental Technology, Tallinn University of Technology, Ehitajate tee 5, 19086 Tallinn, Estonia

## ARTICLE INFO

## Keywords:

Copper antimony selenide  
Raman scattering  
Solar cell  
Magnetron sputtering

## ABSTRACT

Many compound semiconductors in the Cu-Sb-Se group of materials have a great potential as effective and low-cost absorber material for thin film solar cells, such as CuSbSe<sub>2</sub>. In this study, the deposition of CuSbSe<sub>2</sub> thin films by magnetron sputtering method from binary precursors was investigated. As deposited thin films were annealed in selenium atmosphere in different conditions. The influence of selenization temperature and time on the structural and optoelectronic properties of the thin films was studied.

As-deposited CuSbSe<sub>2</sub> thin films had Cu-poor composition. According to structural analysis, as-deposited films contained also Sb<sub>2</sub>Se<sub>3</sub> secondary phase. Post-deposition annealing resulted in the formation of Cu<sub>3</sub>SbSe<sub>4</sub>/Sb<sub>2</sub>Se<sub>3</sub> double-layered structure in the films. Chemical etching with KCN effectively removed Cu<sub>3</sub>SbSe<sub>4</sub> phase and remained Sb<sub>2</sub>Se<sub>3</sub>:Cu layer was implemented in soda-lime glass/Mo/Sb<sub>2</sub>Se<sub>3</sub>:Cu/CdS/i-ZnO/ZnO:Al solar cell device structures, which showed the highest efficiency of 3.2%.

## 1. Introduction

The family of ternary Cu-Sb-Se system includes different compounds: CuSbSe<sub>2</sub>, Cu<sub>3</sub>SbSe<sub>3</sub>, Cu<sub>3</sub>SbSe<sub>4</sub>, Cu<sub>7</sub>SbSe<sub>6</sub> and Cu<sub>12</sub>Sb<sub>4</sub>Se<sub>13</sub>. Among these compounds, CuSbSe<sub>2</sub> has received the most research attention due to its suitable properties like *p*-type conductivity, band gap of 1.04–1.2 eV [1–4], and absorption coefficient of  $1.8 \times 10^5 \text{ cm}^{-1}$  [5] for solar energy conversion. In addition to that, the constituent elements of CuSbSe<sub>2</sub> are inexpensive, nontoxic, and abundant in the earth's crust, which meets the requirements of future photovoltaic (PV) device development. CuSbSe<sub>2</sub> crystallizes in an orthorhombic structure with *Pnma* space group [6].

Cu-Sb-Se system is complicate because it contains besides CuSbSe<sub>2</sub> phase, at least five binary or ternary phases including Cu<sub>2</sub>Se, CuSe, Sb<sub>2</sub>Se<sub>3</sub>, Cu<sub>3</sub>SbSe<sub>4</sub>, and Cu<sub>3</sub>SbSe<sub>3</sub> that could exist as secondary phases if the samples are nonstoichiometric or prepared with an inappropriate process [7]. CuSbSe<sub>2</sub> exists in very narrow compositional region; it should be close to 1:1:2 to prevent the formation of secondary phases. Cu-Se phases are highly conductive and can cause a shunting effect, but Sb<sub>2</sub>Se<sub>3</sub> for example has good optoelectronic properties and has been shown to be an efficient PV absorber [8].

According to spectroscopic limited maximum efficiency calculations [9], the theoretical power conversion efficiency (PCE) of CuSbSe<sub>2</sub> solar

cells is 27%. The highest efficiency reported up to now is 3.8%, where CuSbSe<sub>2</sub> absorber layer was grown by low-temperature pulsed electron deposition [10]. Experimental PCE of CuSbSe<sub>2</sub> solar cells is still low mainly due to the presence of secondary phases (Cu<sub>2</sub>Se, Sb<sub>2</sub>Se<sub>3</sub>, Cu<sub>3</sub>SbSe<sub>3</sub>, Cu<sub>3</sub>SbSe<sub>4</sub> etc.) [11].

Various methods have been used for the synthesis of CuSbSe<sub>2</sub> thin films- electrodeposition [1], sputtering [2,12], reactive close-spaced sublimation [13], electron beam evaporation [14] and pulsed laser deposition [15]. Co-sputtering of the binary compounds used in the present study is a thin film deposition technique, which can provide control on the stoichiometry of the dense films over a large area with a high uniformity. There have been only few studies on the fabrication and characterization of CuSbSe<sub>2</sub> thin films using the co-sputtering method [2,7,12].

The general approach for improving the optical and electrical properties of polycrystalline thin films of semiconductor compounds is post-deposition annealing involving the introduction of additional volatile elements such as the chalcogen [16]. Selenization process is used to improve properties and quality of absorber materials.

The aim of this study was to prepare CuSbSe<sub>2</sub> thin films by magnetron co-sputtering method from Cu<sub>2</sub>Se and Sb<sub>2</sub>Se<sub>3</sub> targets and to develop post-deposition annealing process for as-deposited CuSbSe<sub>2</sub> films. The structural and compositional properties of co-sputtered and post-

<sup>\*</sup> Corresponding author.

E-mail address: [aleksei.penezko@taltech.ee](mailto:aleksei.penezko@taltech.ee) (A. Penezko).



annealed Cu-Sb-Se films, as well as the optoelectronic properties of the solar cell devices based on the annealed thin films were systematically investigated.

## 2. Experiment

Cu-Sb-Se thin films were deposited by co-sputtering method (Angstrom Engineering Evovac 030 with three sputter sources with glow discharge) from binary targets of  $\text{Cu}_2\text{Se}$  (Direct Current Sputtering, DC) and  $\text{Sb}_2\text{Se}_3$  (Radio Frequency Sputtering, RF) at substrate temperature  $350^\circ\text{C}$  for 1 hour. The purity of both targets was 99.99% (Testbourne Ltd). For the substrates, molybdenum as back contact was deposited by DC magnetron sputtering onto cleaned soda-lime glass (SLG) at substrate temperature of  $400^\circ\text{C}$  and Ar pressure of 0.67 Pa for 50 min.

The rotational speed for glass substrate was 2 rpm. The distance between the substrate ( $10\text{ cm} \times 10\text{ cm}$  size) and the targets was set as 12 cm. The background pressure of the vacuum chamber was 0.00093 Pa and the process pressure was 0.53 Pa. The applied power was 27 W for  $\text{Cu}_2\text{Se}$  and 88 W for  $\text{Sb}_2\text{Se}_3$ .

The as-deposited Cu-Sb-Se films were post-annealed in selenium vapor in a dual zone heating tube furnace. Selenization was done in the degassed and sealed quartz ampoules. The sample was put in one side of the ampoule, and Se grain in the second side. Temperatures of both zones were controlled separately. Temperature of the sample side was varied from  $380$  to  $420^\circ\text{C}$ , annealing time was varied from 10 to 60 min and vapor pressure of selenium was kept constant at 133.32 Pa. After selenization, all samples were cooled down naturally to room temperature.

Finally, to evaluate the potential of selenized absorber thin films for photovoltaic applications, heterojunction solar cells with the structure of SLG/Mo/absorber/CdS/*i*-ZnO/ZnO:Al were fabricated. The CdS buffer layer was deposited by chemical bath deposition method with subsequent RF sputtering of the *i*-ZnO/ZnO:Al window layer. CdS was deposited from an aqueous solutions containing 0.02 M cadmium acetate dihydrate ( $\text{Cd}(\text{CH}_3\text{COO})_2 \cdot 2\text{H}_2\text{O}$ ) as source of Cd, 0.35 M thiourea ( $\text{SC}(\text{NH}_2)_2$ ) as source of S, 2 M ammonium hydroxide ( $\text{NH}_4\text{OH}$ ) as a buffer solution for keeping the pH at 11.6. The deposition time was 10 min and temperature was  $60^\circ\text{C}$ . Prior to CdS deposition, the selenized films were etched with 10 wt.% KCN alkaline solution for 60 s.

The crystallographic properties and phase composition of the deposited thin films were investigated by Raman scattering measurements and X-ray diffraction (XRD). For XRD, a Rigaku Ultima IV diffractometer with monochromatic Cu  $\text{K}\alpha 1$  radiation ( $\lambda = 1.5406\text{ \AA}$ ) at 40 kV and 40 mA operating with the silicon strip detector D/teX Ultra was used. Micro-Raman spectra were recorded by using a Horiba's LabRam HR800 spectrometer with a 532 nm laser line. The evolution of the surface morphology and the thickness of films was performed with

high-resolution scanning electron microscope (HR-SEM Zeiss Merlin). Measurements were made at an operating voltage of 3 kV. The chemical composition of the thin films was determined using an energy dispersive x-ray analysis (EDS) system (Bruker EDX-XFlash6/30 detector). For EDS analysis was used operating voltage 10 kV (and 20 kV for mapping) and the concentrations of elements were calculated by using PB-ZAF standardless mode.

Photovoltaic properties of devices based on Cu-Sb-Se films were analyzed by current-voltage characteristics (*I*-*V*) and external quantum efficiency (EQE) measurements. *I*-*V* characteristics were measured under the  $100\text{ mW/cm}^2$  illumination using a Keithley 2400 Source Meter. EQE measurements were done using a computer-controlled SPM-2 monochromator and a 100 W halogen-tungsten light source.

## 3. Results and discussion

### 3.1. Properties of as-deposited Cu-Sb-Se films

Fig. 1 shows SEM images of a) the cross-section and b) surface of as-deposited Cu-Sb-Se thin film co-sputtered from binary targets at  $350^\circ\text{C}$ . Cross-sectional image of Cu-Sb-Se absorber shows that a compact film with thickness around  $1.4\text{ }\mu\text{m}$  was obtained. Top-view SEM image shows that the surface of as-deposited film is heterogeneous. According to the EDX analysis, the as-deposited Cu-Sb-Se polycrystalline thin films had Cu-poor composition - Cu 22.4 at%, Sb 27.3 at% and Se 50.3 at%. EDX elemental mapping analysis of the Cu-Sb-Se thin film showed Sb- and Se-rich regions - Cu 15.3 at%, Sb 32.7 at%, Se 52.0 at% (yellow and pink colored areas in the inset map in Fig. 1b), which could correspond mostly to  $\text{Sb}_2\text{Se}_3$  phase.

Phase composition of the as-deposited film was determined by Raman analysis. Fig. 2 shows Raman spectra of as-deposited Cu-Sb-Se with peaks at 93, 103, 180, 209, and  $214\text{ cm}^{-1}$ , which are attributed to  $\text{CuSbSe}_2$  phase [17]. Additionally, Raman peak at  $192\text{ cm}^{-1}$  was detected, which is assigned to  $\text{Sb}_2\text{Se}_3$  secondary phase [18].

According to XRD pattern presented in Fig. 3a, as-deposited Cu-Sb-Se film consists of  $\text{CuSbSe}_2$  phase (PDF 01-083-9473), which crystallize in orthorhombic structure with space group *Pnma*. The determined lattice parameters for  $\text{CuSbSe}_2$   $a = 6.294\text{ \AA}$ ,  $b = 4.015\text{ \AA}$  and  $c = 14.905\text{ \AA}$  are in good agreement with the literature data [19]. Additionally  $\text{Sb}_2\text{Se}_3$  phase (PDF 03-065-2433) was detected, which crystallizes also in orthorhombic structure.

### 3.2. Properties of selenized Cu-Sb-Se films

In this study, post-deposition annealing was done in a dual zone heating tube furnace. As-deposited  $\text{CuSbSe}_2$  films were selenized at temperatures  $380$ – $420^\circ\text{C}$  for 10 to 60 min under selenium vapor

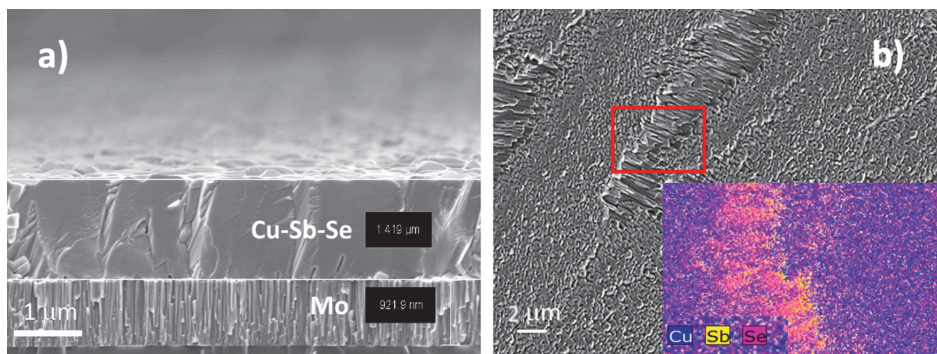


Fig. 1. SEM images of a) cross-section and b) surface of as-deposited Cu-Sb-Se thin film sputtered at  $350^\circ\text{C}$ . Enlarged view in Fig.1b shows EDX elemental mapping of the surface regions of  $\text{Sb}_2\text{Se}_3$ .

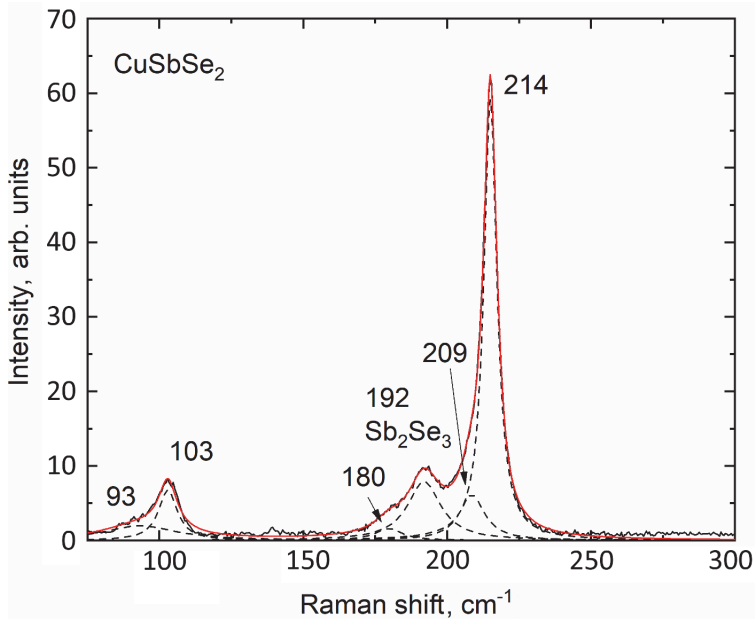


Fig. 2. Raman spectra of as-deposited Cu-Sb-Se thin film together with the fitting using Lorentzian peaks.

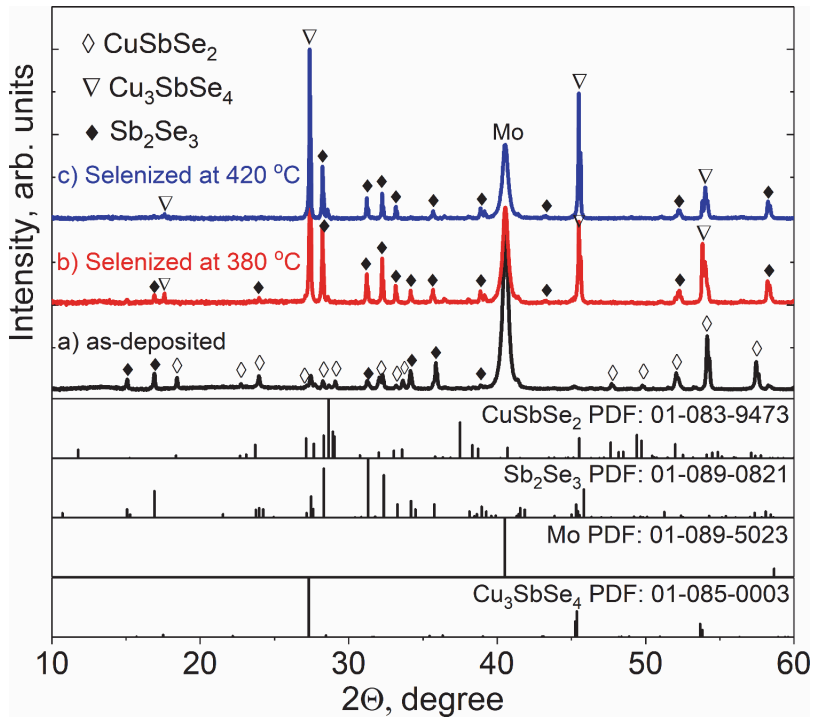


Fig. 3. XRD patterns of a) as-deposited Cu-Sb-Se thin film, b) selenized at 380 °C and c) selenized at 420 °C.

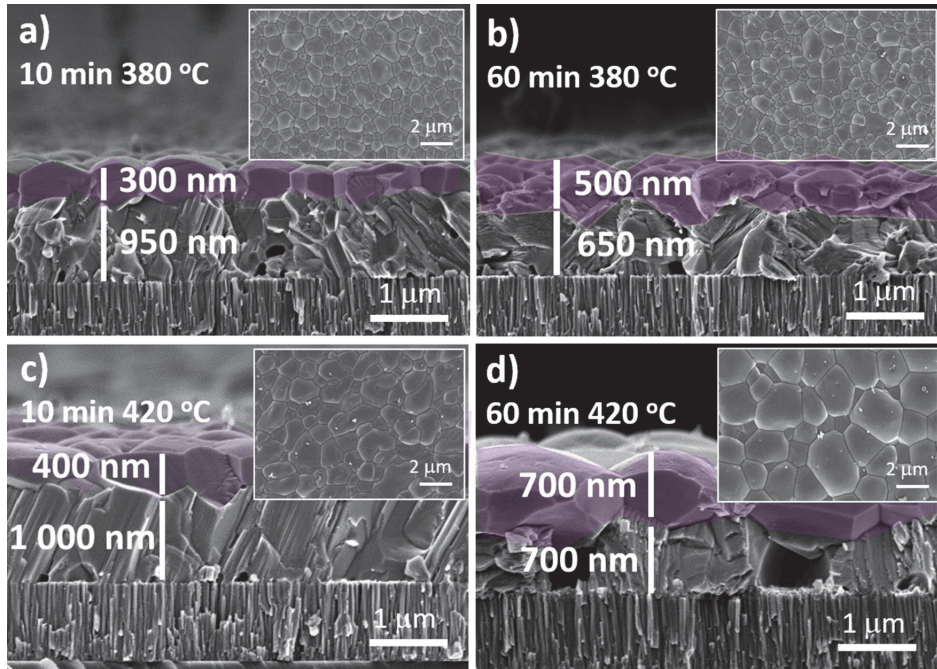


Fig. 4. SEM images of cross-section and surface of thin films selenized at 380 °C a) for 10 min and b) 60 min, at 420 °C c) for 10 min and d) 60 min showing the formed double-layered structure of the selenized films.

pressure of 133.32 Pa.

Fig. 4a and Fig. 4b show SEM images of cross-section and surface of films selenized at 380 °C for 10 min and 60 min. Cross-sectional SEM images show that the selenization process results in the formation of a double layer structure of the films.  $\text{CuSbSe}_2$  decomposed to  $\text{Cu}_3\text{SbSe}_4$  and  $\text{Sb}_2\text{Se}_3$  [12]. The thickness of the top layer increases from ~300 nm to ~500 nm by increasing the annealing time from 10 to 60 min.

Fig. 4c and Fig. 4d show the SEM images of cross-section and surface of the films selenized at 420 °C for 10 and 60 min. The crystals in the top layer of the film are growing much larger with increasing the annealing temperature and time. Furthermore, top-view SEM images (inset images in Fig. 4d) show the formation of large sintered crystals after annealing at higher temperatures (420 °C). The thickness of top layer after selenization at 420 °C for 60 min is approximately 700 nm. The estimated thickness of the bottom layer is ~700 nm. Unfortunately, the formed thin film also contains pinholes between large crystals exposing the Mo back contact.

After the selenization at 420 °C for 60 min, the double-layered films

were analyzed by EDX elemental depth profiles across the cross-section of the film as shown in Fig. 5. According to the EDX profile, Cu concentration increased from the bottom layer to top layer (marked with a red line in Fig. 5b) and the concentration of Sb decreased in the same direction (marked with a green line in Fig. 5b). The content of Se was homogeneously distributed over the cross-section of film (marked with a blue line in Fig. 5b). EDX analysis showed that the surface layer contains Cu 33.8 at% and Sb 12.1 at% ([Cu]/[Sb] ratio is 2.79) and near the Mo-back contact the Cu content was 9.7 at% and Sb content was 33.3 at% ([Cu]/[Sb] = 0.29).

To determine the phase composition of double-layered Cu-Sb-Se films, Raman analysis was performed on the cross-section of samples. Fig. 6 shows the Raman spectra measured from the cross-section of Cu-Sb-Se film selenized at 420 °C. Based on the relative intensities of the Raman peaks, it shows that on the back contact side (edge near Mo/SLG) is mainly  $\text{Sb}_2\text{Se}_3$  phase with characteristic Raman peaks at 98, 191 and 212 [17]. On the front side (near the surface) is mainly  $\text{Cu}_3\text{SbSe}_4$  phase with characteristic Raman peaks at 165, 183, 227 and 234  $\text{cm}^{-1}$ , which

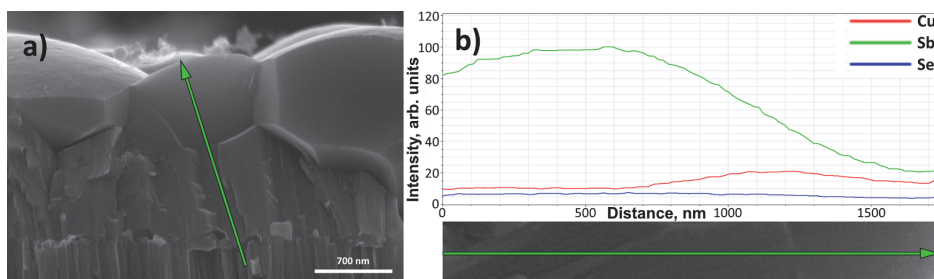


Fig. 5. a) SEM images of cross-section of Cu-Sb-Se selenized at 420 °C for 60 min and b) corresponding EDX profile.

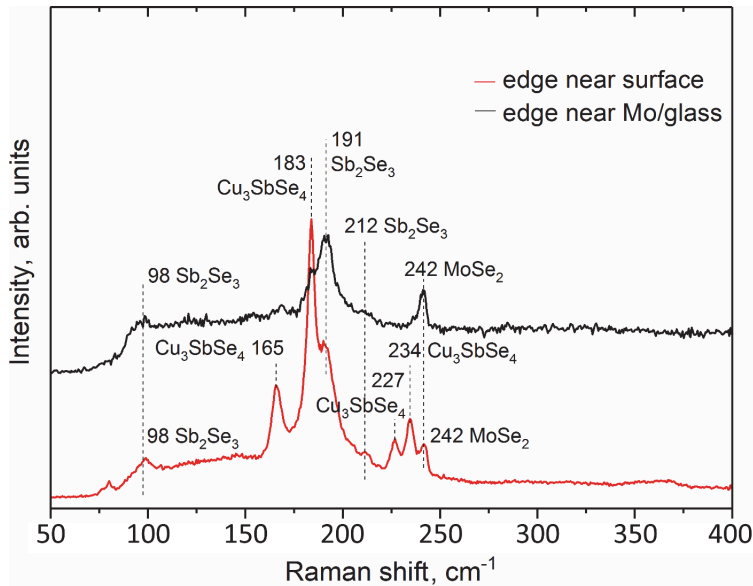


Fig. 6. Raman spectra of Cu-Sb-Se thin film selenized at 420 °C for 60 min.

are in correspondence with the data presented in Ref. [20]. Raman peak at 242  $\text{cm}^{-1}$  belongs to  $\text{MoSe}_2$  [21].

XRD analysis confirmed that  $\text{CuSbSe}_2$  films decomposed after selenization at 380 °C and 420 °C, the new phases appeared. In Fig. 3b and 3c are presented XRD patterns of the Cu-Sb-Se films after selenization at 380 °C and 420 °C. It can be seen that strongest diffraction peaks can be perfectly indexed to a tetragonal structure  $\text{Cu}_3\text{SbSe}_4$  (PDF 01 85-0003; space group  $I-42m$ ) with lattice constants  $a = 5.645 \text{ \AA}$  and  $c = 11.237 \text{ \AA}$ , which are in good agreement with the experimental data in the literature [20]. In addition to  $\text{Cu}_3\text{SbSe}_4$ , the binary antimony selenide phase with the orthorhombic structure (ICDD # 01-089-0821, space group  $Pbnm$ ) with the unit cell parameters  $a = 11.617 \text{ \AA}$ ,  $b = 11.750 \text{ \AA}$ ,  $c = 3.972 \text{ \AA}$  was detected.

### 3.3. Properties of solar cells

As  $\text{Cu}_3\text{SbSe}_4$  compound detected as the top layer of the selenized films has very small bandgap 0.29 eV [22], KCN chemical etching was applied before using the selenized thin films as absorber layers in solar cells. KCN etching is typically used to remove Cu-chalcogenide phases [23]. After the etching process, the remaining porous thin film contained mainly  $\text{Sb}_2\text{Se}_3$  phase (Sb 39.6 at%, Se 57.5 at% by EDX) with small amount of Cu (2.9 at% by EDX). Fig. 7 shows the SEM image of cross-section of the prepared solar cell structure glass/Mo/ $\text{Sb}_2\text{Se}_3$ :Cu/CdS/*i*-ZnO/ZnO:Al and the highest PCE of 3.2% was achieved. The open circuit voltage ( $V_{oc}$ ) of the cell was 373 mV, fill factor ( $FF$ ) 52.1% and short circuit current density ( $J_{sc}$ ) 16.5  $\text{mA}/\text{cm}^2$ . The working area

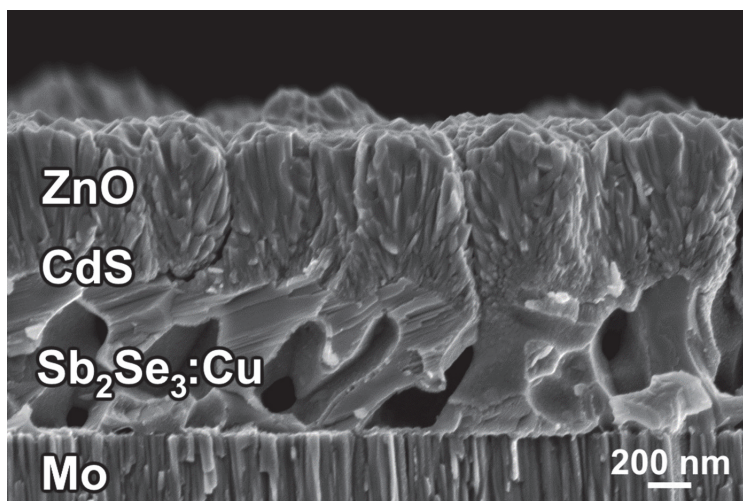


Fig. 7. SEM image of the cross-section of solar cell with the structure: glass/Mo/ $\text{Sb}_2\text{Se}_3$ :Cu/CdS/*i*-ZnO/ZnO:Al.

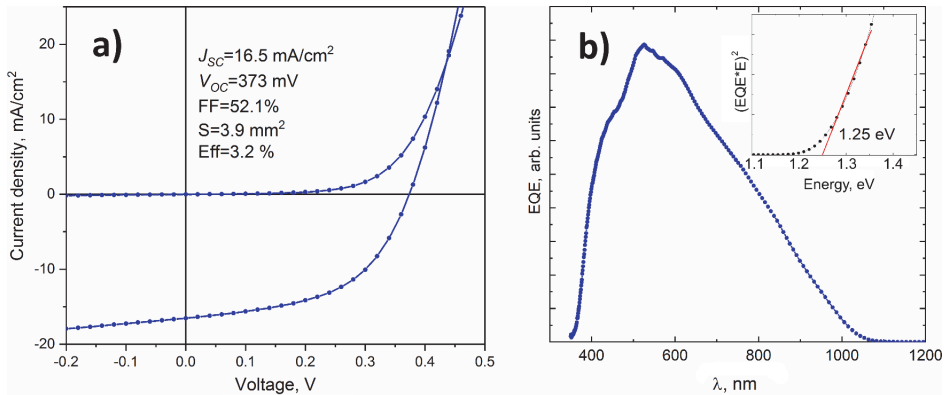


Fig. 8. a)  $J$ - $V$  characteristic and b) EQE of solar cell with the structure: glass/Mo/Sb<sub>2</sub>Se<sub>3</sub>:Cu/CdS/*i*-ZnO/ZnO:Al.

was 3.9 mm<sup>2</sup> (Fig. 8).

EQE was used to determine the band gap ( $E_g$ ) value of absorber material. The EQE spectra was measured as a function of the incident light wavelength at room temperature in the wavelength range from 350 to 1200 nm. From the linear segment of the low-energy side of the construction  $(EQE)^2$  vs.  $E$  curves, the effective bandgap energy ( $E_g^*$ ) was evaluated. Estimated band gap value was 1.25 eV, which is in good correlation with reported bandgap values for Sb<sub>2</sub>Se<sub>3</sub> [24].

#### 4. Conclusion

In this study we successfully deposited CuSbSe<sub>2</sub> thin films by magnetron sputtering method. According to EDX analysis the as-deposited CuSbSe<sub>2</sub> thin films had Cu-poor composition. Structural analysis by XRD and Raman spectroscopy revealed that as-deposited films had additionally traces of Sb<sub>2</sub>Se<sub>3</sub>. Post-deposition annealing in selenium atmosphere resulted in the formation of Cu<sub>3</sub>SbSe<sub>4</sub>/Sb<sub>2</sub>Se<sub>3</sub> double-layered structure in the films. Chemical etching with KCN effectively removed Cu<sub>3</sub>SbSe<sub>4</sub> phase and remained Sb<sub>2</sub>Se<sub>3</sub>:Cu layer was implemented in SLG/Mo/Sb<sub>2</sub>Se<sub>3</sub>:Cu/CdS/*i*-ZnO/ZnO:Al solar cell device structures. The highest efficiency of 3.2% was achieved absorber layer that was post-annealing at 380 °C for 30 min followed by KCN etching.

#### CRedit authorship contribution statement

Corresponding author: Aleksei Penezko – Conceptualization, Methodology, Validation, Formal analysis, Investigation, Writing – original draft, Visualization, Cu-Sb-Se sample preparation, Material and device characterization.

Author: Maarja Grossberg – Conceptualization, Resources, Supervision, review & editing, Project administration, Funding acquisition.

Author: Marit Kauk-Kuusik – Conceptualization, Resources, Supervision, review & editing, device completion, Project administration, Funding acquisition.

Author: Olga Volobujeva – SEM and EDS analysis, reviewing & editing

#### Declaration of Competing Interest

The authors declare that they have no known competing financial interests or personal relationships that could have appeared to influence the work reported in this paper

#### Acknowledgements

This work was financially supported by European Union through the European Regional Development Fund, Project TK141, ERDF project “Center of nanomaterials technologies and research (NAMUR+)” (2014–2020.4.01.16–0123) and by the Estonian Research Council grant PRG1023.

#### References

- [1] D. Tang, J. Yang, F. Liu, Y. Lai, J. Li, Y. Liu, Growth and characterization of CuSbSe<sub>2</sub> thin films prepared by electrodeposition, *Electrochim. Acta.* 76 (2012) 480–486, <https://doi.org/10.1016/j.electacta.2012.05.066>.
- [2] A.W. Welch, L.L. Baranowski, P. Zawadzki, S. Lany, C.A. Wolden, A. Zakutayev, CuSbSe<sub>2</sub> photovoltaic devices with 3% efficiency, *Appl. Phys. Express.* 8 (2015) 82301, <https://doi.org/10.7567/apex.8.082301>.
- [3] D.-J. Xue, B. Yang, Z.-K. Yuan, G. Wang, X. Liu, Y. Zhou, L. Hu, D. Pan, S. Chen, J. Tang, CuSbSe<sub>2</sub> as a Potential Photovoltaic Absorber Material: studies from Theory to Experiment, *Adv. Energy Mater.* 5 (2015), 1501203, <https://doi.org/10.1002/aenm.201501203>.
- [4] D. Colombara, L.M. Peter, K.D. Rogers, J.D. Painter, S. Roncallo, Formation of CuSbS<sub>2</sub> and CuSbSe<sub>2</sub> thin films via chalcosynthesis of Sb–Cu metal precursors, *Thin Solid Films* 519 (2011) 7438–7443, <https://doi.org/10.1016/j.tsf.2011.01.140>.
- [5] M. Kumar, C. Persson, Cu(Sb, Bi)(S, Se)<sub>2</sub> as Indium-free Absorber Material with High Optical Efficiency, *Energy Procedia* 44 (2014) 176–183, <https://doi.org/10.1016/j.egypro.2013.12.025>.
- [6] T. Wada, T. Maeda, Optical properties and electronic structures of CuSbS<sub>2</sub>, CuSbSe<sub>2</sub>, and CuSb(S<sub>1-x</sub>Se<sub>x</sub>)<sub>2</sub> solid solution, *Phys. Status Solidi C* 14 (2017), 1600196, <https://doi.org/10.1002/pssc.201600196>.
- [7] S. Kim, N.-H. Kim, Impurity Phases and Optoelectronic Properties of CuSbSe<sub>2</sub> Thin Films Prepared by Cosputtering Process for Absorber Layer in Solar Cells, *Coatings* 10 (2020) 1209, <https://doi.org/10.3390/coatings10121209>.
- [8] Z. Li, X. Liang, G. Li, H. Liu, H. Zhang, J. Guo, J. Chen, K. Shen, X. San, W. Yu, R.E. I. Schropp, Y. Mai, 9.2%-efficient core-shell structured antimony selenide nanorod array solar cells, *Nat. Commun.* 10 (2019) 125, <https://doi.org/10.1038/s41467-018-07903-6>.
- [9] L. Yu, R.S. Kokenyesi, D.A. Keszler, A. Zunger, Inverse Design of High Absorption Thin-Film Photovoltaic Materials, *Adv. Energy Mater.* 3 (2013) 43–48, <https://doi.org/10.1002/aenm.201200538>.
- [10] S. Rampino, F. Pattini, M. Bronzoni, M. Mazzer, M. Sidoli, G. Spaggiari, E. Gilioli, CuSbSe<sub>2</sub> thin film solar cells with ~4% conversion efficiency grown by low-temperature pulsed electron deposition, *Sol. Energy Mater. Sol. Cells.* 185 (2018) 86–96, <https://doi.org/10.1016/j.solmat.2018.05.024>.
- [11] B. Yang, C. Wang, Z. Yuan, S. Chen, Y. He, H. Song, R. Ding, Y. Zhao, J. Tang, Hydrazine solution processed CuSbSe<sub>2</sub>: temperature dependent phase and crystal orientation evolution, *Sol. Energy Mater. Sol. Cells.* 168 (2017) 112–118, <https://doi.org/10.1016/j.solmat.2017.04.030>.
- [12] A.W. Welch, L.L. Baranowski, H. Peng, H. Hempel, R. Eichberger, T. Unold, S. Lany, C. Wolden, A. Zakutayev, Trade-Offs in Thin Film Solar Cells with Layered Chalcostibite Photovoltaic Absorbers, *Adv. Energy Mater.* 7 (2017), 1601935, <https://doi.org/10.1002/aenm.201601935>.
- [13] C. Wang, B. Yang, R. Ding, W. Chen, R. Kondrotas, Y. Zhao, S. Lu, Z. Li, J. Tang, Reactive close-spaced sublimation processed CuSbSe<sub>2</sub> thin films and their photovoltaic application, *APL Mater* 6 (2018) 84801, <https://doi.org/10.1063/1.5028415>.

- [14] D. Goyal, C.P. Goyal, H. Ikeda, P. Malar, Role of growth temperature in photovoltaic absorber  $\text{CuSbSe}_2$  deposition through e-beam evaporation, *Mater. Sci. Semicond. Process.* 108 (2020), 104874, <https://doi.org/10.1016/j.mssp.2019.104874>.
- [15] T. Guo, D. Wang, Y. Yang, X. Xiong, K. Li, G. Zeng, B. Li, M. Ghali, Preparation and characterization of  $\text{CuSbSe}_2$  thin films deposited by pulsed laser deposition, *Mater. Sci. Semicond. Process.* 127 (2021), 105716, <https://doi.org/10.1016/j.mssp.2021.105716>.
- [16] O.K. Simya, B.G. Priyadarshini, K. Balachander, A.M. Ashok, Formation of a phase pure kesterite CZTSe thin films using multisource hybrid physical vapour deposition, *Mater. Res. Express.* 7 (2020) 16419, <https://doi.org/10.1088/2053-1591/ab64ee>.
- [17] A. Penezko, M. Kauk-Kuusik, O. Volobujeva, R. Traksmaa, M. Grossberg, Observation of photoluminescence edge emission in  $\text{CuSbSe}_2$  absorber material for photovoltaic applications, *Appl. Phys. Lett.* 115 (2019) 92101, <https://doi.org/10.1063/1.5114893>.
- [18] M. Grossberg, O. Volobujeva, A. Penezko, R. Kaupmees, T. Raadik, J. Krustok, Origin of photoluminescence from antimony selenide, *J. Alloys Compd.* 817 (2020), 152716, <https://doi.org/10.1016/j.jallcom.2019.152716>.
- [19] W. Qiu, L. Wu, X. Ke, J. Yang, W. Zhang, Diverse lattice dynamics in ternary Cu-Sb-Se compounds, *Sci. Rep.* 5 (2015) 13643, <https://doi.org/10.1038/srep13643>.
- [20] P. Martínez-Ortiz, S. Lugo-Loredo, J. Campos-Álvarez, Y. Peña-Méndez, J. A. Aguilar-Martínez, Growth and characterization of  $\text{Cu}_3\text{SbSe}_4$  thin films through thermally diffusing  $\text{Sb}_2\text{Se}_3$  – CuSe by chemical bath deposition (CBD), *Mater. Res. Bull.* 102 (2018) 418–423, <https://doi.org/10.1016/j.materresbull.2018.02.049>.
- [21] P. Tonndorf, R. Schmidt, P. Böttger, X. Zhang, J. Börner, A. Liebig, M. Albrecht, C. Kloc, O. Gordan, D.R.T. Zahn, S. Michaelis de Vasconcellos, R. Bratschitsch, Photoluminescence emission and Raman response of monolayer  $\text{MoS}_2$ ,  $\text{MoSe}_2$ , and  $\text{WSe}_2$ , *Opt. Express.* 21 (2013) 4908, <https://doi.org/10.1364/OE.21.004908>.
- [22] T.-R. Wei, H. Wang, Z.M. Gibbs, C.-F. Wu, G.J. Snyder, J.-F. Li, Thermoelectric properties of Sn-doped p-type  $\text{Cu}_3\text{SbSe}_4$ : a compound with large effective mass and small band gap, *J. Mater. Chem. A.* 2 (2014) 13527–13533, <https://doi.org/10.1039/C4TA01957A>.
- [23] A.H. Pinto, S.W. Shin, E.S. Aydil, R.L. Penn, Selective removal of  $\text{Cu}_{2-x}(\text{S,Se})$  phases from  $\text{Cu}_2\text{ZnSn}(\text{S,Se})_4$  thin films, *Green Chem.* 18 (2016) 5814–5821, <https://doi.org/10.1039/C6GC01287F>.
- [24] S. Polivtseva, J.O. Adegite, J. Kois, D. Mamedov, S.Z. Karazhanov, J. Maricheva, O. Volobujeva, A Novel Thermochemical Metal Halide Treatment for High-Performance  $\text{Sb}_2\text{Se}_3$  Photocathodes, *Nanomaterials* 11 (2020) 52, <https://doi.org/10.3390/nano11010052>.

# Curriculum vitae

## Personal data

Name: Aleksei Penezko  
Date of birth: 04.05.1987  
Place of birth: Estonia  
Citizenship: Estonian

## Contact data

E-mail: aleksei.penezko@taltech.ee

## Education

2018–2022 Tallinn University of Technology, Chemical and Materials Technology, PhD  
2013–2015 Tallinn University of Technology, Virumaa College, Fuel chemistry and technology – MSc (*cum laude*)  
2006–2010 Tallinn University of Technology, Virumaa College, Fuel technology – BSc (*cum laude*)  
1994–2006 Kohtla-Järve Ahtme Gymnasium, Secondary education

## Language competence

Russian Native  
English Proficient  
Estonian Intermediate

## Participation in conferences

2021 European Materials Research Society Spring Meeting 2021, online.  
Poster presentation.  
2019–2021 Graduate School of Functional Materials and Technologies (GSFMT), Tallinn University of Technology and Tartu University, Estonia. Oral and poster presentations.  
2019 European Materials Research Society 2019 Spring Meeting and Exhibition, Nice, France. Poster presentation.

## Professional employment

2018–2022 Laboratory of Photovoltaic Materials, Tallinn University of Technology, early stage researcher  
2012–2017 VKG AS, engineer

## Research project

RPG1023 “Sustainable, cost-efficient, flexible, lightweight and semi-transparent multinary chalcogenide based solar cells for building integrated photovoltaics”.

## List of publications

1. **A. Penezko**, M. Kauk-Kuusik, O. Volobujeva, R. Traksmaa, and M. Grossberg, Observation of photoluminescence edge emission in CuSbSe<sub>2</sub> absorber

- material for photovoltaic applications, Appl. Phys. Lett. 115, 092101, 2019. <https://doi.org/10.1063/1.5114893>
2. M. Grossberg, O. Volobujeva, **A. Penezko**, R. Kaupmees, T. Raadik, J. Krustok, Origin of photoluminescence from antimony selenide, Journal of Alloys and Compounds, Volume 817, 152716, 2020. <https://doi.org/10.1016/j.jallcom.2019.152716>
  3. **Penezko**, M. Kauk-Kuusik, O. Volobujeva, M. Grossberg, Properties of Cu-Sb-Se thin films deposited by magnetron co-sputtering for solar cell applications, Thin Solid Films 740, 139004, 2021. <https://doi.org/10.1016/j.tsf.2021.139004>



## Elulookirjeldus

### Isikuandmed

Nimi: Aleksei Penezko  
Sünniaeg: 04.05.1987  
Sünnikoht: Eesti  
Kodakondsus: eesti

### Kontaktandmed

E-post: aleksei.penezko@taltech.ee

### Hariduskäik

2018–2022 Tallinna Tehnikaülikool, keemia- ja materjalitehnoloogia, PhD  
2013–2015 Tallinna Tehnikaülikool, Virumaa Kolledž, Kütuste keemia ja tehnoloogia – MSc (*cum laude*)  
2006–2010 Tallinna Tehnikaülikool, Virumaa Kolledž, Kütuste tehnoloogia – BSc (*cum laude*)  
1994–2006 Kohtla-Järve Ahtme Gümnaasium, keskkharidus

### Keelteoskus

Vene keel Emakeel  
Inglise keel Kõrgtase  
Eesti keel Kesktase

### Osalemine konverentsidel

2021 Euroopa Materjaliuuringute Seltsi kevadine võrgukonverents ja näitus. Plakatettekanne.  
2019–2021 Funktsionaalsete materjalide ja tehnoloogiate doktorikool (FMTDK), Tallinna Tehnikaülikool ja Tartu Ülikool, Eesti. Suulised ja plakatettekanded.  
2019 Euroopa Materjaliuuringute Seltsi kevadine konverents ja näitus, Nice, Prantsusmaa. Plakatettekanne.

### Teenistuskäik

2018–2022 Päikeseenergeetika Materjalide Teaduslabor, Tallinna Tehnikaülikool, doktorant-nooremteadur  
2012–2017 VKG AS, insener

### Teadusprojektid

RPG1023 “Mitmik-kalkogeeniididel põhinevad jätkusuutlikud, kuluefektiivsed, kerged, painduvad ja poolläbipaistvad ehitisingreeritavad päikesepatareid”.

### Teaduspublikatsioonid

1. **A. Penezko**, M. Kauk-Kuusik, O. Volobujeva, R. Traksmaa, and M. Grossberg, Observation of photoluminescence edge emission in CuSbSe<sub>2</sub> absorber material for photovoltaic applications, Appl. Phys. Lett. 115, 092101, 2019. <https://doi.org/10.1063/1.5114893>

2. M. Grossberg, O. Volobujeva, **A. Penezko**, R. Kaupmees, T. Raadik, J. Krustok, Origin of photoluminescence from antimony selenide, *Journal of Alloys and Compounds*, Volume 817, 152716, 2020. <https://doi.org/10.1016/j.jallcom.2019.152716>
3. **Penezko**, M. Kauk-Kuusik, O. Volobujeva, M. Grossberg, Properties of Cu-Sb-Se thin films deposited by magnetron co-sputtering for solar cell applications, *Thin Solid Films* 740, 139004, 2021. <https://doi.org/10.1016/j.tsf.2021.139004>

ISSN 2585-6901 (PDF)  
ISBN 978-9949-83-940-7 (PDF)